# NIOBIUM OXIDE BASED MATERIAL FOR VISIBLE LIGHT PHOTOCATALYSIS

Thesis submitted in accordance with the requirements of the University of Liverpool for the degree of Doctor in Philosophy

by

Christopher P. Ireland

November 2012

# Abstract

The primary aim of the work presented in this thesis was to design and synthesise well-characterised material that would exploit visible light to promote photocatalysis, involving the degradation of organic compounds in water, or generation of hydrogen from the water splitting reaction. In doing so, both environmental concerns, such as the removal of pollutants in wastewater, and energy concerns, such as the generation of a clean and safe form of hydrogen for use as a renewable fuel could be addressed. The approach used was to employ existing methods to synthesise high surface area quasi-amorphous material that is active in UV light for photocatalysis, and then design and employ post synthetic modification to promote the material for visible light photocatalysis.

Niobium (V) oxide was synthesised in a high surface area form, successfully scaling up the synthesis from 2 g to over 200 g quantities of as made material. This UV active photocatalyst was fully characterized by methods including X-ray diffraction and thermal gravimetric analysis. The material was used to degrade the model dye Methyl Orange and generate hydrogen from a methanol / water solution without further modification.

By adding platinum group metals (PGMs) to the niobium (V) oxide, a greatly enhanced efficiency for hydrogen generation was realized. A survey of metals (platinum rhodium and palladium) and weight percentages of metal added (0.01 – 1%) was carried out, with the PGM added materials characterised for hydrogen generation using a methanol / water sacrificial reagent system, as well as PGM dispersion, TEM imaging, EDX and X-ray photoelectron spectroscopy for characterising the higher weight percentage material.

Finally, chromium (III) oxide was added to the surface of the niobium (V) oxide in various weight percentages (1% - 5%). The optical properties of this composite material, in comparison with the starting materials were investigated, in particular the difference in diffuse reflectance of the starting materials and composite were highlighted to demonstrate charge transfer between the chromium (III) on the surface, and niobium (V), in the bulk of the material, with the oxidation states being confirmed by XPS. Furthermore, this material was found to degrade methyl orange under visible light. An action spectrum was carried out measuring the quantum efficiency of the reaction at different wavelengths, which proved it was the chromium – niobium charge transfer absorbance in isolation that was responsible for the methyl orange degradation.

# Acknowledgements

I would firstly like to thank my supervisor, Prof. Matt Rosseinsky for his guidance and support over the nearly 4 years of my studentship, in addition to my secondary supervisor, Dr. John Claridge for his excellent advice and suggestions throughout the project. I would also like to thank my industrial supervisor, Dr. Stephen Poulston for his advice, guidance and support, in particular on my visits to the Johnson Matthey Technology Centre in Sonning Common, when Stephen and his team made me feel welcome. I would in particular like to thank Prof. Jim Darwent, for his continued friendship, knowledge, advice and support over my time here, which has been invaluable.

I would like to thank Dr. Rob Palgrave for all his help, in particular his valuable help and guidance in understanding optical measurements. I would also like to thank Dr. Jo Clark for her friendship and helpful discussions about our work. I would like to thank former members of the Photocatalysis Group at Liverpool who helped me extensively when I first arrived: Dr. Emiliana Dvininov and Dr. Upendra Joshi, in addition to Dr. Hongjun Niu and Dr. Duong Giap, who provided support in the initial stages of the photocatalysis project. Additionally, I would like to thank Dr. Alexandra Fateeva, Dr. Paul Williams, Dr. Paul Boldrin, Dr. Philip Chater and Peter King whom I have worked with over the past few years on some fascinating projects. I would like to thank the new members of the Photocatalysis Team at Liverpool: Dr. Asif Tahir, Dr. Bo Liu, Borbala Kiss and Tom Mangnall, and wish them well in their work here. I would also like to thank our Masters Students who I worked with in the Photocatalysis Group: Suzanna Hussain and Ellie Laney, in particular for their enthusiasm for the projects they were involved in.

I would also like to thank people from Johnson Matthey who have assisted me on the project, in particular Dr. Andy Smith, Dr. Steve Bennett, Dr. Andrew Steele and Dr. Dogan Ozkaya

I would finally like to thank my family, friends and colleagues who have made my time at Liverpool University an enjoyable experience.

## Table of Contents

**1 Introduction ..... 1**

**1.1 Solar Energy ..... 1**

**1.2 Photocatalysis ..... 2**

**1.3 Visible Light Photocatalysis ..... 11**

**1.4 Improving the Efficiency of the Photocatalyst ..... 19**

**1.5 Aim and Scope of the Project ..... 24**

**1.6 References ..... 27**

**2 Experimental Methods ..... 33**

**2.1 Hydrogen Generation ..... 33**

2.1.1 Standard Hydrogen Generation Protocol ..... 34

2.1.2 Benchmarking of Hydrogen Measurements ..... 36

2.1.3 Henry's Law Considerations ..... 38

**2.2 Methyl Orange Degradation ..... 39**

2.2.1 Neutral pH Methyl Orange Degradation Reactions ..... 41

2.2.2 Acid pH Methyl Orange Degradation Reactions ..... 42

**2.3 Diffuse Reflectance ..... 43**

**2.4 Chemical Actinometry ..... 45**

**2.5 PGM dispersion Analysis ..... 46**

**2.6 Other Characterisation ..... 47**

2.6.1 X-Ray Diffraction ..... 47

2.6.2 X-Ray Photoelectron Spectroscopy (XPS) ..... 49

2.6.3 BET Method for Calculating Surface Area ..... 49

2.6.4 Thermogravimetric Analysis and Microanalysis ..... 51

2.6.5 Microscopy (SEM, TEM and EDX) ..... 52

**2.7 References ..... 54**

**3 Niobium Oxide ..... 56**

**3.1 Introduction ..... 56**

**3.2 Mesoporous $Nb_2O_5$ ..... 63**

3.2.1 Synthesis of Mesoporous $Nb_2O_5$ ..... 64

3.2.2 Characterisation of Mesoporous $Nb_2O_5$ ..... 65

**3.3 Nanoparticulate $Nb_2O_5$ ..... 72**

3.3.1 Synthesis of Nanoparticulate $Nb_2O_5$ ..... 72

3.3.2 Characterisation of Nanoparticulate $Nb_2O_5$ ..... 73

**3.4 Methyl Orange Degradation with Nano and Meso $Nb_2O_5$ ..... 75**

**3.5 Scaled Up Nanoparticulate $Nb_2O_5$ ..... 76**

3.5.1 Synthesis of Scaled Up Nanoparticulate $Nb_2O_5$-1 ..... 77

3.5.2 Further modification of the synthesis ..... 77

3.5.3 Characterisation of $Nb_2O_5$-1 and $Nb_2O_5$-3 ..... 80

3.5.4 Calcining $Nb_2O_5$-1 and $Nb_2O_5$-3 ..... 83

**3.6 Further Scaling Up of Nanoparticulate $Nb_2O_5$ ..... 90**

3.6.1 Synthesis of Further Scaled Up Nanoparticulate $Nb_2O_5$-B1 and $Nb_2O_5$-B2 ..... 91

3.6.2 Characterisation of $Nb_2O_5$-B1 and $Nb_2O_5$-B2 ..... 93

**3.7 Conclusion ..... 96**

**3.8 References ..... 97**

**4 Platinum Group Metals on Niobium Oxide ..... 100**

**4.1 Introduction ..... 100**

**4.2 Synthesis and Characterisation of PGM Added Material ..... 103**

4.2.1 Addition of Platinum to $Nb_2O_5$ by the Impregnation Method ..... 103

4.2.2 Addition of Platinum to $Nb_2O_5$ by the Photodeposition Method ..... 105

4.2.3 Addition of Rhodium or Palladium to $Nb_2O_5$ by the Impregnation Method ..... 106

4.2.4 Characterisation of PGM-$Nb_2O_5$ material ..... 108

**4.3 Hydrogen Measurements ..... 123**

4.3.1 $Nb_2O_5$ Hydrogen Generation ..... 123

4.3.2 Platinum Added $Nb_2O_5$ Hydrogen Generation ..... 124

4.3.3 Rhodium Added $Nb_2O_5$ Hydrogen Generation ..... 127

4.3.4 Palladium Added $Nb_2O_5$ Hydrogen Generation ..... 129

4.3.5 Addition of two co-catalysts ($RuO_2$ and Pt) ..... 131

**4.4 Conclusion and Future Work ..... 133**

**4.5 References ..... 135**

**5 Chromium – Niobium Based Composites ..... 136**

**5.1 Introduction ..... 136**

**5.2 Synthesis and Characterisation of $Cr_2O_3$-$Nb_2O_5$ ..... 140**

5.2.1 Synthesis of $Cr_2O_3$-$Nb_2O_5$ ..... 140

5.2.2 Characterisation of 3%$Cr_2O_3$-$Nb_2O_5$:500 ..... 142

**5.3 Composite Optical Properties ..... 147**

5.3.1 Optical Properties During Synthesis ..... 147

5.3.2 Optical Properties of Niobium Oxide ..... 150

5.3.3 Optical Properties of Chromium Oxide ..... 151

5.3.4 Optical Properties of 3%$Cr_2O_3$-$Nb_2O_5$:500 ..... 155

**5.4 Photocatalysis Reactions ..... 161**

5.4.1 Methyl Orange Visible Light Photocatalysis ..... 161

5.4.2 Methyl Orange Degradation of Niobium Oxide and Chromium Oxide Under Visible Light ..... 162

5.4.3 Methyl Orange Degradation of 5%$Cr_2O_3$-$Nb_2O_5$:500 Under Visible Light ..... 164

5.4.4 Action Spectrum of 5%$Cr_2O_3$-$Nb_2O_5$:500 ..... 166

**5.5 Conclusion and Future Work ..... 168**

**5.6 References ..... 170**

**6 Conclusion ..... 172**

# 1 Introduction

## 1.1 Solar Energy

With energy and environmental concerns coming to the forefront in recent years, much scientific research is directed at solving these problems, by developing safe and renewable sources of energy, and combating environmental pollution. The amount of solar energy incident on the Earth's surface is 1003 W $m^{-2}$, using data supplied by the American Society for Testing and Materials,[1-2] as used in Ohtani's 2008 review of photocatalysis misconceptions.[3] The idea of utilizing this renewable energy source is extremely attractive, compared to non–renewable sources of energy such as fossil fuels, with a finite lifetime; particularly useful is being able to use solar energy to drive chemical or electrical processes.[4]

The application of this can be of very low complexity. SODIS (SOlar DISinfection) can be used to disinfect water in developing regions, whereby plastic water bottles are filled with water and left out in sunlight for approximately six hours. This solar disinfection kills all bacteria and most pathogens in the water using both thermal and optical processes, providing a cleaner water supply than would be obtained without the procedure, with evidence showing lasting health benefits in the population.[5-6] Alternatively, high complexity devices could be used to utilize solar energy. For example, photovoltaic cells based on crystalline silicon, with efficiency of nearly 25% being used to covert solar energy to electricity[7]; devices such as a photoelectrochemical cell have also been used to convert solar energy to electricity that drive an electrochemical reaction, such as electrolysis of water, generating oxygen and hydrogen.[8-9] In this and the SODIS example, solar energy is being converted into a chemical process, either the degrading organic matter in the case of SODIS, or generating electricity to provide electrolysis in the case of the photoelectrochemical cell.

This thesis concentrates on the area of photocatalysis, with the aim of synthesising material, a photocatalyst, that is catalytically able to utilize solar energy to drive chemical processes. For example, the photocatalyst could be added to contaminated water; sunlight combined with the photocatalyst can then catalytically degrade the pollutants, cleaning up the water. Alternatively, the photocatalyst could be placed in water with sunlight, inducing the photocatalyst to split water into hydrogen and oxygen with the hydrogen being captured and used as a fuel. Whilst applications such as these are impressive and inspiring goals, the actual achievement and commercial viability of such applications and objectives are some way off.[10]

The introduction to this thesis aims to explain in more detail the concepts of photocatalysis giving an explanation of the mechanisms involved, and will also critically discuss the objectives and challenges associated with the area. The introduction will survey visible light photocatalysis, assessing the literature-based methods of synthesizing and characterising visible light material, and discussing how the visible light nature of the material can be assessed. The introduction also contains a discussion of ways of improving the efficiency of the photocatalyst, focusing on the involvement of Platinum Group Metals (PGMs) in photocatalysis, including the initial work with PGMs and photocatalysis, and the limited amount of literature that studies in detail PGM with the photocatalyst characterisation. The introduction concludes with the scope and aims of the work discussed in this thesis, linking the work carried out to current literature.

## 1.2 Photocatalysis

Since 1970, when Fujishima and Honda demonstrated hydrogen generation on illumination from a system employing rutile titanium dioxide ($TiO_2$) as a photo-anode, and platinum as a photo-cathode with an external bias,[11] research in this area has increased year on year, with many comparable materials identified that are able to split water into hydrogen and oxygen.[12] The majority of research of such materials is focused on two areas: organic

degradation,[13-16] and hydrogen generation through water splitting,[17-21] although the use of photocatalysts for other applications such as using light to synthesise material is also a key area, for example organic transformations such as the conversion of benzene to phenol, or using light to synthesise metal nanoparticles such as gold.[22-23] The use of photocatalysts as a component of photovoltaic systems is also a keen area of research.[24-26] Material that can be employed as a photocatalyst in this way are invariably semiconductors that undergo photo-excitation.[27-29]

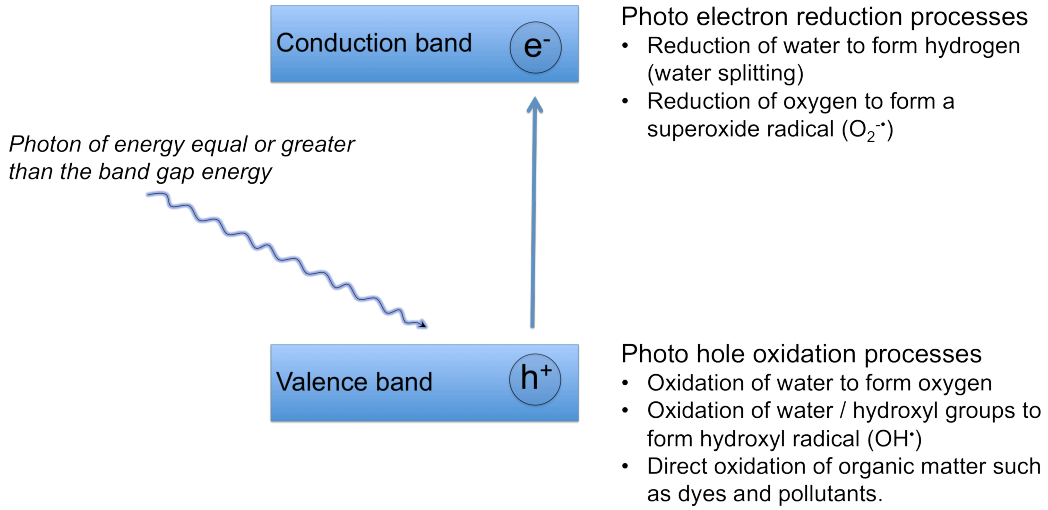


**Figure 1-1** Diagram illustrating the photo-excitation of semiconductors such as titanium dioxide, and the oxidation and reduction processes that can be involved with photoelectrons and holes.

Semiconductors are extended structures, where the atomic orbitals have combined to form bands, consisting of comparable energy levels, with a filled valence band, and an empty higher energy conduction band, separated by an energy gap (band gap, $E_g$), the difference in energy between the highest occupied state of the valance band and lowest unoccupied state of the conduction band. Semiconductor oxides have an electronic band structure such that the valence band, dominated by oxygen 2*p* orbitals, is full with the electrons unable to transport charge, and the higher energy conduction band, consisting predominantly of the metal ion *d* orbitals, empty of electrons.

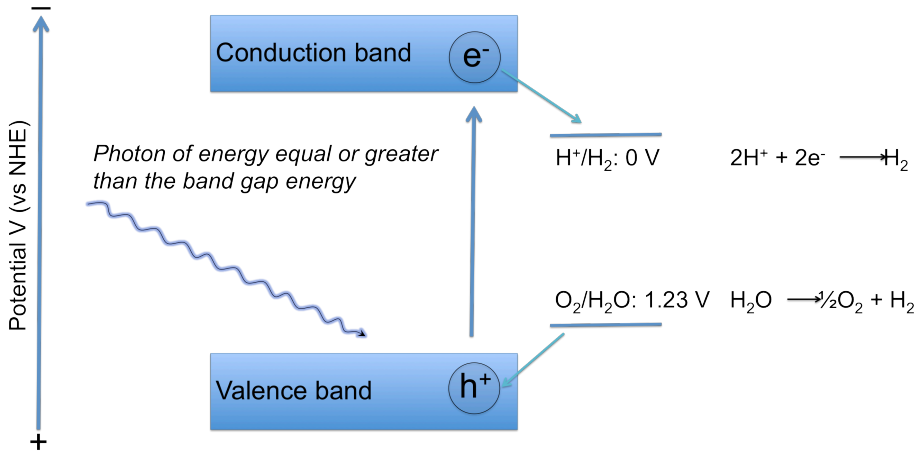


**Figure 1-2** Potential energy diagram for photochemical water splitting at pH 0, using a semiconductor.

For the vast majority of photocatalytic semiconductors, including titanium dioxide, ($TiO_2$) niobium (V) oxide ($Nb_2O_5$) and tantalum (V) oxide ($Ta_2O_5$), the energy required to excite the electron from the valence band to the conduction band is equivalent in energy to photons of UV light.[30] As illustrated in Figure 1-1, shining UV light at material such as $TiO_2$ allows electrons to be promoted from the valence band to the conduction band of the material. This leaves holes in the valence band that can be involved in oxidation processes, and promoted electrons in the conduction band, which can be involved in reduction processes.

For water splitting to occur, i.e. the reduction of water to hydrogen, and the oxidation of water to oxygen, the reduction and oxidation potential of the conduction band and valence band in the semiconductor have to be at the correct potential to allow these redox reactions to occur. To allow the reduction of water to form hydrogen, the bottom of the conduction band of the semiconductor must be at a more negative reduction potential than the reduction potential of $H^+$ / $H_2$, defined as 0 V vs NHE at pH 0, with the reduction of water to hydrogen requiring two electrons (Figure 1-2). With the conduction band consisting predominantly of *d* orbitals from the metal component of the semiconductor oxide, the

metal in the oxide heavily influences this reduction potential. Similarly, the top of the valence band must be at a more positive reduction potential than the oxidation potential of $H_2O$ / $O_2$, defined as 1.23 V vs NHE at pH 0 (Figure 1-2), to allow the oxidation of water to form oxygen, with this a four electron process.

Provided the conduction band and valence band are at reduction potentials that allow water splitting to occur, a semiconductor with a band gap greater than 1.23 eV will be able to oxidise and reduce water, and so facilitate water splitting. The band gaps of some oxides are illustrated in Figure 1-3; also plotted are the conduction band reduction potentials, and the valence band oxidation potentials, relative to the reduction and oxidation potentials of water.

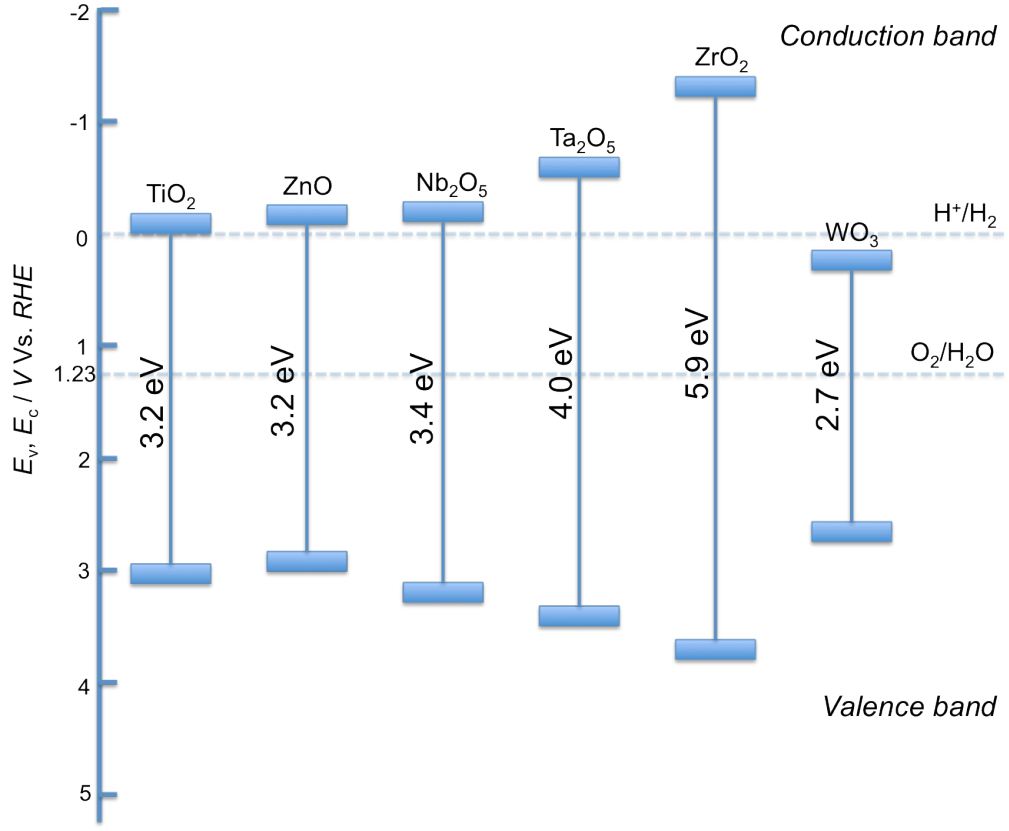


**Figure 1-3** Conduction band potentials, valence band potentials and band gaps of some common oxide semiconductors, with the oxidation and reduction potentials of water also plotted, at pH = 0. Data taken from Matsumoto.[30]

Whilst these potentials are the values at pH 0, it has been shown that these potentials are influenced by pH, with Ward et al. demonstrating the electron in a semiconductor has a greater reducing power as the pH increases, i.e. conduction band potential becomes less negative, as indicated in Equation 1-1, derived from the work in measuring photocurrent as a function of pH.[31]

$$E_{\mathrm{F}} = E_{\mathrm{F}}(\mathrm{pH}\ 0) - 0.059\ \mathrm{pH}$$

**Equation 1-1** Equation demonstrating the relationship between pH and the flat band potential of a semiconductor ($E_{\mathrm{F}}$) at the specific pH.[31]

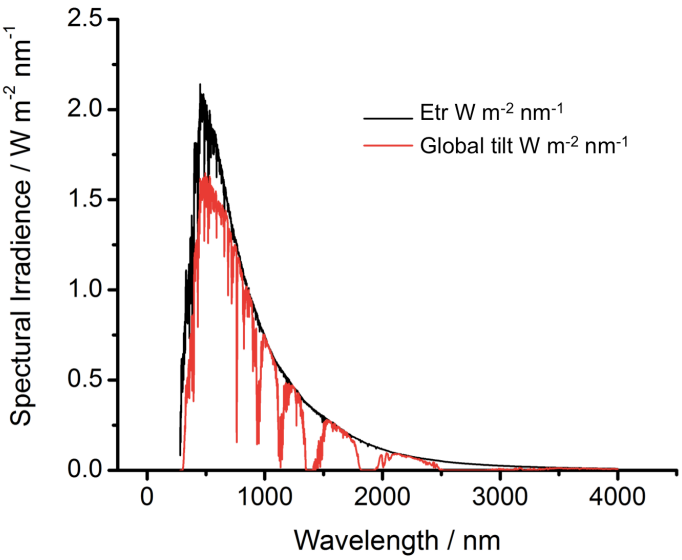


**Figure 1-4** the spectrum of solar light at the surface of the Earth (Global tilt); data taken from ASTM.[1-2]

Whilst the boundary between visible and UV light is somewhat arbitrary, one can define visible light as electromagnetic radiation of a wavelength between 380 nm and 760 nm emanating from the Sun; by taking this definition visible light accounts for 53% of the energy of the solar spectrum under typical conditions in North America, whereas the higher energy UV region (which can be defined as electromagnetic wavelength of less than 410 nm) accounts for only 10% of the solar spectrum based on the energy of light.[2] With

photons of visible light therefore having an energy of less than around 3 eV, a semiconductor with a band gap between 1.23 eV and 3.00 eV with the correct reduction / oxidation potentials for water splitting would be highly desirable, as such material with visible light band gaps would be able to utilize more of the solar spectrum than material requiring UV light to induce photo-excitation. All the simple oxides illustrated in Figure 1-3 with the exception of tungsten oxide ($WO_3$) have a band gap in the UV light energy region; whilst the band gap of $WO_3$ is such that visible light will induce photo generated electrons and holes, the photo generated electrons in the conduction band, at a more positive reduction potential than $H^+$ / $H_2$, will not be able to reduce water to hydrogen, although oxidation of water is viable by the photo generated holes. Synthesising semiconductors with the correct band positions in terms of water splitting and visible light absorbance is an intensive area of research, which is explored in detail in Section 1.3.

When degrading organic matter using a semiconducting photocatalyst, light with an energy larger than the photocatalyst band gap can excite electrons from the valence band to the conduction band, producing holes that are able to directly oxidise the dye, or produce hydroxyl radicals able to degrade the dye; photo generated electrons are able to produce oxygen radicals that can produce more hydroxyl radicals that can also degrade the dye (Figure 1-5(a)). The degradation of organic matter may occur via an alternative mechanism if the matter is able to absorb light itself, such as a dye. Here the dye is able to absorb light and so reach an excited state; electrons from the organic matter could be transferred to the semiconductor oxide conduction band (Figure 1-5(b)).[32] These electrons in the conduction band can produce oxygen radicals that can produce hydroxyl radicals able to eventually degrade the dye. The excited dye itself can also degrade itself by photo bleaching. In both these alternative reactions, the actual band gap of the semiconductor photocatalyst is not relevant; the absorbance properties of the organic material determine the energy of light required to initiate the reaction, and so wavelength of light required to degrade the matter. Dye sensitized solar cells work on a comparable principle, with a ruthenium-based dye

responsible for the visible light absorbance, injecting the electron directly into the semiconductor (routinely $TiO_2$) conduction band, with the actual band gap of the semiconductor irrelevant.[24]

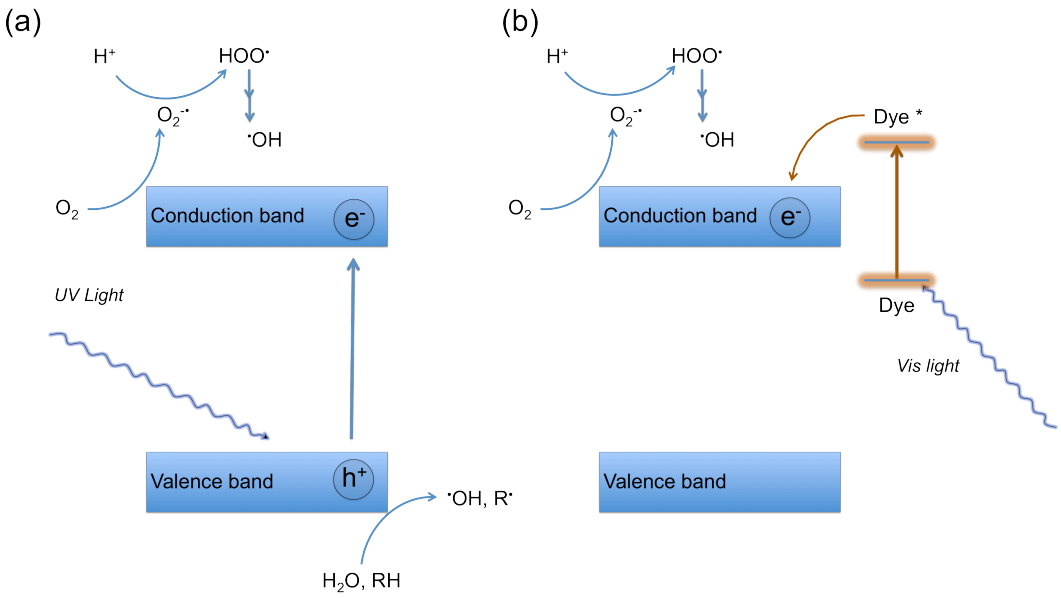


**Figure 1-5** Processes involved in the photodegradation of dyes (a) using light with a greater energy than the semiconductor band gap to induce dye degradation; (b) using light with an energy less than the semiconductor band gap, but able to induce the dye into an excited state. Figure adapted from Zhao et al.[32]

For photocatalysis involving the excitation of electrons from the valence band to the conduction band, a key process is the migration of the hole and electron after excitation of the particle to the surface, where they can be used in redox processes. However, the species can be recombined without undergoing redox reactions, via bulk recombination (Figure 1-6). Similarly, the hole and electron may recombine on the surface. In both cases the energy is expelled as heat, and the recombination has a detrimental effect on the reaction rate, reducing the efficiency of the photocatalysis reaction being performed.

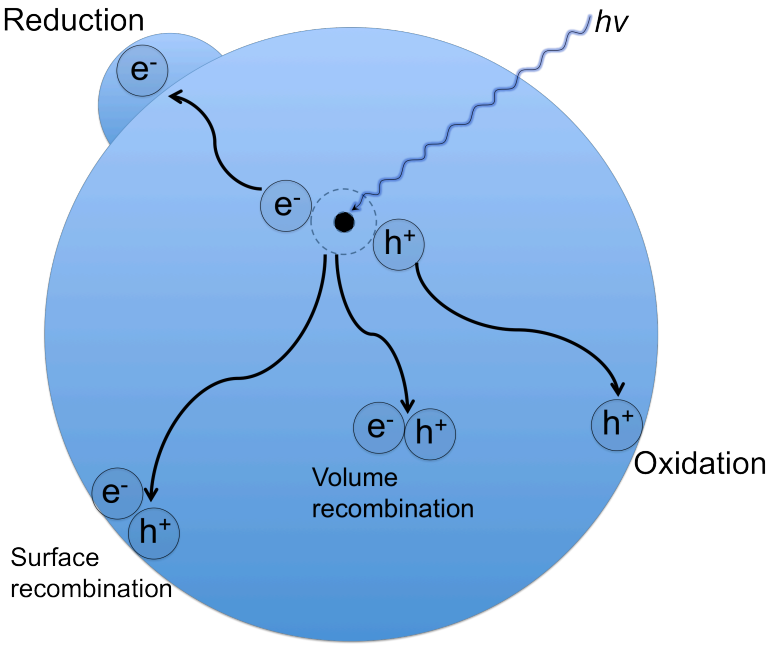


**Figure 1-6** Processes occurring on a semiconductor after excitation by light greater than the semiconductor band gap. Adapted from Mills and Le Hunte.[14]

The efficiency of the photocatalysis reaction can be described as the Quantum Efficiency (*QE*) of the reaction. This value is a number based on the amount of hydrogen or oxygen produced for water splitting, or material degraded for organic degradation reactions, and the flux of incident photons, which can measured by the technique of Chemical Actinometery.[33]

$$QE = \frac{A \times R}{I}$$

**Equation 1-2** Quantum efficiency, with '*A*' a coefficient based on the reaction taking place (ie 2 for hydrogen evolution, 4 for oxygen evolution as the processes are 2 and 4 electron processes respectively), '*R*' a measure of the reaction rate, and '*I*' the flux of incident photons.

This value in often quoted as Apparent Quantum Yield (*AQY*); the Quantum Yield itself being difficult to measure, due to the difficulty in accurately determining the actual number of photons being absorbed by the catalyst, with photons likely to be scattered or reflected i.e. not be absorbed by the catalyst. The *QE* or *AQY* assume that all the photons

reported (*I*) are absorbed in a catalyst suspension, and so are utilized in excitation and the generation of holes and electrons.[21]

| Material | Light Source | QE / % | Reference |
|---|---|---|---|
| NiO-La:$NaTaO_3$ | UV | 56 | [34] |
| Rh-$TiO_2$ (coated with NaOH | UV | 29 | [35] |
| | | | |
| $(Ga_{1-x}Zn_x)(N_{1-x}O_x)$ solid solution | Vis (420 – 440 nm) | 2.5 | [17] |
| Ni:$InTaO_4$ | Vis (> 420 nm) | 0.66 | [36] |
| TaON / $WO_3$ Z scheme | Vis (> 420 nm) | 0.4 | [37] |

**Table 1-1** Table showing the highest Quantum Efficiencies of photocatalysts reported to split pure water under UV light and visible light.

The material with the highest reported Quantum Efficiency for pure water splitting under UV light, with the *QE* reported as 56%, is Kudo's NiO modified La:$NaTaO_3$.[34] For visible light systems, the highest reported *QE* is significantly lower, with Domen's $(Ga_{1-x}Zn_x)(N_{1-x}O_x)$ solid solution with a QE of 2.5%, the highest efficiency visible light photocatalyst for splitting pure water,[38] recently found to be stable under reaction conditions for 3 months.[39]

Minimizing the particle size has a positive effect on reducing the electron / hole recombination occurring in the bulk of the particle; as discussed in Section 1.4, adding a co-catalyst such as a PGM can also have the effect of creating an electron gradient, with the electron migrating towards the metal, allowing greater separation between the photo generated hole and electron.

The ideal photocatalyst for use in solar light therefore, should have a band gap less than 3.0 eV, to allow visible absorbance, with steps taken to minimize electron / hole recombination, allowing greater efficiency. Section 1.3 explores the methods of

synthesising visible light active photocatalysts, and modification of UV active photocatalysts to facilitate visible light absorbance. Following this, Section 1.4 explores the ways of improving the efficiency of the photocatalysis material, concentrating on co-catalysts, and in particular discussing the role of PGMs in this.

## 1.3 Visible Light Photocatalysis

As briefly discussed earlier in the chapter, the amount of solar energy incident on the Earth's surface is 1003 W $m^{-2}$ under typical conditions in North America; of this, visible light accounts for 53% of the solar spectrum. Therefore material able to both absorb and utilize visible light radiation in a photocatalytic reaction are a keen area of research, with applications in both water splitting, with the aim of generating hydrogen for use as a fuel, and organic pollutant degradation, addressing environmental concerns using renewable energy.

Jae Sung Lee, in his 2006 review of water splitting using visible light photocatalysts,[18] succinctly summarised the different types of visible light photocatalysts, describing modification of UV active photocatalysts by cation doping, modification by anion doping, single-phase visible light photocatalysts, and finally multi-component photocatalysts. Lee describes an example of the multi-component photocatalyst being the $(Ga_{1-x}Zn_x)(N_{1-x}O_x)$ solid solution,[38] as of 2011 the material with the highest quantum efficiency for overall pure water splitting under visible light. This relatively low quantum efficiency for the visible light water splitting reaction, whilst disappointing compared with the target of 10 % efficiency thought to be the minimum required for commercial applications[12, 40], indicates there is much scope for improvement.

Research has been carried out into cation doping of UV light active semiconductors, with the idea of inducing visible light absorbance. In his excellent review of 2010,[28] Herrmann describes an example of cation doping: chromium doping into $TiO_2$ as "catastrophic", the

main issue being the dopant acting as a recombination centre for holes and electrons, thus decreasing the efficiency of the reaction. Lee agrees somewhat, discussing the doping of chromium or iron in $La_2Ti_2O_7$.[18] Doping with chromium or iron does induce visible absorbance, seen as a shoulder in the diffuse reflectance; band structure calculations show the dopant forms what Lee describes as an interband, a electron band situated within the conventional conduction – valence band gap. Whilst visible light will promote electrons to the conduction band, the holes left in the interband are not oxidizing enough to oxidise water; in fact the interband serves as a recombination site for photo-generated holes and electrons. Herrmann's review states "it is now generally and finally admitted that cationic doping is detrimental to photocatalysis"; whilst results by Jae Sung Lee show that cationic doping does induce visible light photocatalysis, the poor efficiency of the resulting material, in addition to the understanding of the band structure, shows that other ways of producing visible light photocatalysts may be more successful.

Perhaps a better approach is the second of those discussed by Lee: modification of UV active photocatalysts by anion doping. One of the most widely studied visible light photocatalysts of recent years is nitrogen doped $TiO_2$,[41] with the original paper by Asahi et al. published in 2001 having nearly 4000 citations as of June 2012.[42] The hybridization of oxygen 2*p* orbitals and nitrogen 2*p* orbitals at the top of the valence band raises the energy potential of the valence band, and so supposedly reduces the band gap, with the conduction band unaffected. Whilst Lee et al. compared N doped $TiO_2$ with their $PbBi_2Nb_2O_9$ material for hydrogen generation and oxygen generation,[43] with only negligible hydrogen produced with N doped $TiO_2$ using sacrificial methanol, the majority of papers published with N doped $TiO_2$ concern organic degradation reactions under visible light,[41] or recently water purification of toxins.[44] Although a successful photocatalyst, the exact nature of the doping is still being explored, with much of the research focused on identifying the nature of the doping; for example whether the doping is substitutional or interstitial.[45]

In his review, Lee assigns TaON as an example of anion doping of $Ta_2O_5$; while the method of preparation of the material is similar with that of N doped $TiO_2$, the actual TaON produced is single phase, and so should perhaps be classified as such. The Domen group has studied this material in detail, since first publishing the first example of its use in water oxidation reactions,[46] and then hydrogen generation reactions with co-catalysts under visible light.[47] Despite showing significant activity in both hydrogen and oxygen generation, there is little literature by other groups, or other photocatalytic applications of the material, in water purification or organic degradation for example. The stability of TaON in water may perhaps be a factor, with nitrides and oxynitrides known to oxidise in water, although Domen's photocatalytic testing shows the material to be stable for the duration of the reactions tested. A related compound, $Ta_3N_5$ is also found to be a good visible light photocatalyst for water splitting, generating hydrogen and oxygen using sacrificial reagents.[48] As with TaON, this material is a single phase, and again Domen finds no evidence of the catalyst degrading over the course of the reactions carried out.

Unlike N doped $TiO_2$, and cation doped material such as chromium or iron doped $La_2Ti_2O_7$ described earlier, the diffuse reflectance of TaON and $Ta_3N_5$ shows a distinct band gap in the visible region of the spectrum; the diffuse reflectance doped material generally shows a shoulder forming in the visible region from the band gap reflectance of the undoped oxide. Lee attributes this shoulder in the diffuse reflectance of N doped $TiO_2$ to the difference in the formal oxidation numbers of oxygen ($O^{2-}$) and nitrogen ($N^{3-}$) producing oxygen defects in the lattice of the doped material. These defects also have a detrimental effect on the efficiency of the photocatalysis reaction, acting as electron / hole recombination centres.

Other anionic doping of oxides includes carbon doping or sulfur doping, both of which have been used to successfully modify oxides to absorb visible light. Carbon doped $TiO_2$ films, synthesised by Khan et al.,[49] were found to be able to split water stoichiometrically under a 150 W Xe lamp. Whilst the films were not tested under exclusively visible light,

the group found the photocurrent was much higher with the C doped $TiO_2$ films compared to the undoped $TiO_2$ when light from a 150 W Xe lamp illuminated the films, indicating significantly more absorbance of light and improved efficiency of the C doped $TiO_2$; evidence of this is provided by the diffuse reflectance, which shows significant absorbance in the visible region, although as with N doped $TiO_2$ material, the $TiO_2$ band gap is still evident. Sulfur doping of $TiO_2$ again provides visible absorbance,[50] with Umebayashi et al. finding the band gap of S doped $TiO_2$ shifting towards the visible region, although the band gaps quoted for $TiO_2$ and sulfur doped $TiO_2$ (2.3 eV and 1.4 eV respectively) appear suspect. Ohtani successfully used sulfur doped $TiO_2$ to degrade AcOH, with an action spectrum, a plot of the efficiency of the reaction in addition to the diffuse reflectance of the catalyst over wavelength of light, proving the visible light absorbing sulfur doped $TiO_2$ was responsible for the photoactivity.[51]

Aside from the oxy-nitrides and nitrides mentioned previously, there are few single phase visible light absorbing compounds that are capable of both oxidizing and reducing water, to induce overall water splitting. The $PbBi_2Nb_2O_9$ material synthesised by Kim et al.[43] is one such example; another is $RbPb_2Nb_2O_{10}$.[52] The electronic structure of these multi-element oxides is more complicated than UV active single metal oxide material such as $TiO_2$ and $Nb_2O_5$, with both $Ti^{4+}$ and $Nb^{5+}$ in the respective materials having no *d* electrons in the metal oxidation state they are in leaving the conduction band mainly consisting of the empty metal *d* orbitals, and the valence band consisting mainly of 2*p* orbitals from the oxygen. With the $PbBi_2Nb_2O_9$ material, the valence band consists of O2*p* orbitals hybridized with Bi 6*s* orbitals and Pb 6*s* orbitals, leading to an increase in the energy position of the valence band, and so narrowing the band gap of the material.[43]

Whist the majority of single phase photocatalysts are either oxides, oxynitrides, or nitrides,[12] recently non-metal visible light photocatalysts have been synthesised. An example is the thermal polycondensation of organic monomers to synthesise graphitic

carbon nitrides ($C_3N_4$).[53] This material was used to successfully generate hydrogen from a methanol / water solution, with an action spectrum carried out to confirm that the efficiency of the reaction was dependent on the catalyst absorption of light.

Multi component photocatalysts cover a wide range of photocatalysts that can utilize visible light. In addition to solid solutions, two distinct metal species can be present on the same particle, or two distinct visible light particles providing separate reduction and oxidation sites can be used in tandem with electron transfer ions in solution.[54]

The previously mentioned GaN/ZnO system is an example of a solid solution, with Domen giving the formula as $(Ga_{1-x}Zn_x)(N_{1-x}O_x)$.[38] With a quantum yield at 2.5% at 420 nm – 440 nm, Domen reported this material was able to generate hydrogen and oxygen from pure water at efficiency at nearly a magnitude higher than previously reported visible light photocatalysts. The material was loaded with mixed oxides of rhodium and chromium as co-catalysts, and since this initial synthesis of the material was published, work has concentrated on improving the efficiency of the material by characterising and optimizing the rhodium – chromium co-catalyst.[55-60] This work is another demonstration of the importance of co-catalysts in synthesising the most efficient photocatalysts; the novel chromium – rhodium co-catalyst used here proving to be the best one for the GaN/ZnO system.

$WO_3$ is an effective visible light oxidation catalyst, however it cannot be used for water splitting due to the conduction band having an energy less than the reduction potential of water, and so is unable to reduce water to hydrogen. By combining with another photocatalyst that can reduce water, in a solution that can transfer the electron from one oxide to another, overall water splitting can be achieved. This system, called a Z-scheme due to its similarity to photosynthesis,[61] has been effectively used over the past few years. Domen used the single phase TaON, loaded with platinum, as the reduction photocatalyst, capable of reducing water to hydrogen under visible light, with Pt-$WO_3$ used as the

oxidation catalyst (Figure 1-7).[37] Used with an iodide ($I^-$) solution, the TaON is able to oxidise the $I^-$ to $IO_3^-$ using the visible light generated holes. In the same system, Pt-$WO_3$ is able to oxidise water under visible light, to oxygen; the photo-generated electrons are able to reduce the $IO_3^-$ back to $I^-$, with the $I^-$ / $IO_3^-$ described as a shuttle redox mediator. Whilst this system working under visible light, provides a higher level of efficiency than the TaON on its own, which itself is capable of oxidizing and reducing water, the coloured $I^-$ / $IO_3^-$ redox shuttle is absorbing in the visible region and so reduces the overall efficiency of the system, and work is underway to find a transparent redox shuttle as efficient as the $I^-$ / $IO_3^-$ shuttle.

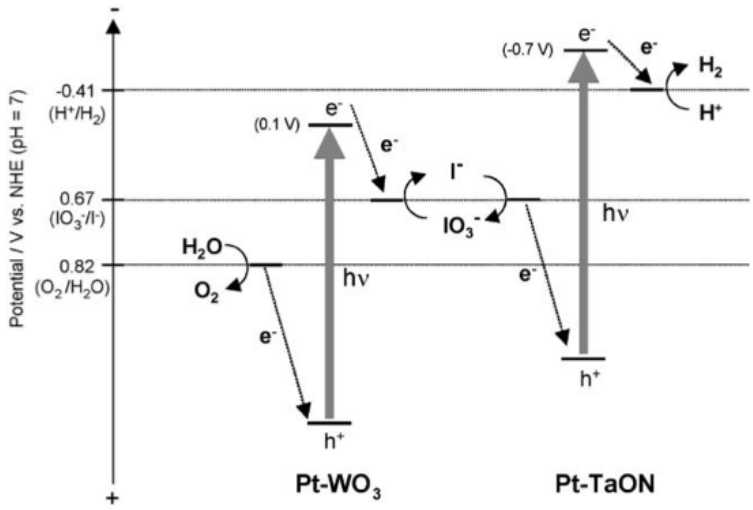


**Figure 1-7** Proposed mechanism for using a Z-scheme for water splitting over Pt–TaON and Pt–$WO_3$ with an $IO_3^-$ / $I^-$ shuttle redox mediator. From Abe et al.[37]

Alternatively, a single particle Z-scheme could be synthesised, which eliminates the need for a redox shuttle. Kudo, in 2009 synthesised a novel material by combining Ru/$SrTiO_3$:Rh and $BiVO_4$ powders at pH 3.5, with the surface charge of the two materials at that pH ensuring that the two combine to form aggregates.[62] This single particulate system was able to produce hydrogen and oxygen from water, with the doped rhodium ($Rh^{3+}$ / $Rh^{4+}$) in the Ru/$SrTiO_3$:Rh system effectively acting as the electron shuttle.

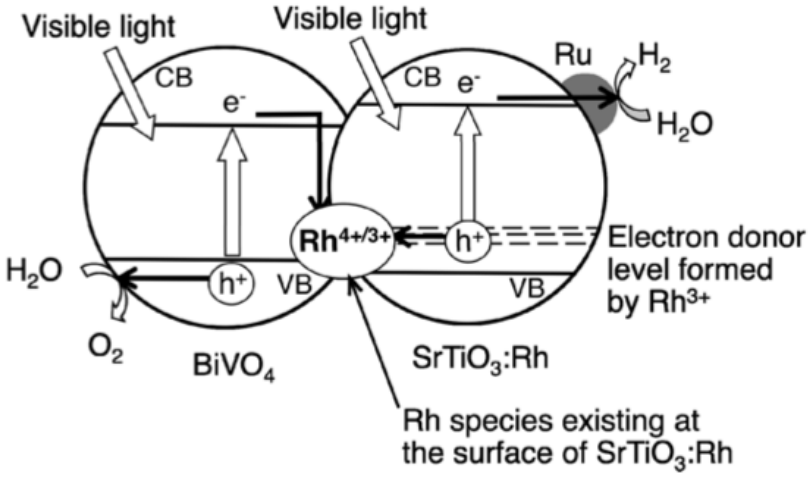


**Figure 1-8** Mechanism of water splitting using the single particle Z-scheme photocatalysis system driven by electron transfer between the oxygen producing $BiVO_4$ and hydrogen producing $SrTiO_3$:Rh. From Sasaki et al.[62]

Yun et al. recently reported a single particulate Z-scheme,[63] comparable to a previously synthesised single particulate Z-scheme reported by Tada et al.,[64] consisting of Pt/CdS/Au/$TiO_2$. The synthesis of this material is more involved than the simple combination of material at low pH of Kudo's work; carbon doped $TiO_2$ ($TiO_{1.96}C_{0.04}$) was photodeposited with gold initially, and this material was then photodeposited with a cadmium precursor, to give a cadmium sulfide shell over the gold nanoparticles previously photodeposited. This material was further photodeposited with platinum metal, to give a platinum co-catalyst (Pt/CdS/Au/$TiO_{1.96}C_{0.04}$). This platinized material was then tested for hydrogen generation, with NaS and $NaSO_3$ solution as sacrificial reagents. Under visible light illumination, the $TiO_{1.96}C_{0.04}$ was demonstrated to act as the oxidation catalyst; photo generated electrons, migrating through the gold nanoparticle, then combined with the photogenerated hole from the CdS, with the photogenerated electron from CdS generating hydrogen.

Whilst the Z-schemes mentioned involve both materials individually absorbing visible light, producing holes and electrons, an alternative absorbance involving two metal species

involves the direct transfer of the electron from one metal species to another, using energy provided by light. Work pioneered by Frei is a significant example of this metal – metal charge transfer (MMCT) with the first example of this being used in photocatalysis evident in Frei's work with zirconium and copper.[65] As will be discussed in more detail in the introduction to Chapter 5 of this thesis, zirconium in the +4 oxidation state was loaded onto a silica support, in addition to copper in the +1 oxidation state. On illumination with visible light, an electron from Zr(IV) was transferred to Cu(I); the Zr(III) species was then able to reduce $CO_2$ to CO. Similarly, Hashimoto and his group loaded chromium(III) onto the surface of $TiO_2$, and investigated the visible light MMCT between Cr(III) and Ti(IV) in $TiO_2$, and used this interaction to degraded propan-2-ol.[66] Clark et al. successfully used the strategy of using visible light MMCT between two metal species as a basis to investigate the photocatalytic properties of $CaCu_3Ti_4O_{12}$, noting the MMCT interaction between the copper and titanium in the compound.[67] The strategy was continued in this thesis, by using the interaction between niobium (V) species and chromium (III) species as a basis for synthesising a composite, as will be discussed in Chapter 5.

From literature therefore, although there are sound strategies for producing visible light photocatalysts, many suffer from the complex nature of the compound. For example the $(Ga_{1-x}Zn_x)(N_{1-x}O_x)$/Cr-Rh system,[38] and the Pt/CdS/Au/$TiO_{1.96}C_{0.04}$ system.[63] The lack of understanding or repeatability of synthesising the material can also be problematic, for example the $TiO_xN_{1-x}$, where there is little control in being able to substitute or intercalate nitrogen into the lattice of $TiO_2$.[41] TaON, and oxynitrides whilst relatively straightforward to synthesise suffer from perceived instability.

Another observed problem with visible light catalysis is suspicions over whether results are actually valid.[3] For example many systems use a light source that contains UV light, with visible light provided by using filters that cut off at a wavelength of light (normally 420 nm), which filters light below that wavelength; the suspicion in the relatively low

efficiency of the 'visible light' catalyst is due to a small amount of UV radiation bypassing the filter. This suspicion can be avoided by providing an action spectrum, a spectrum which plots the efficiency of the reaction, routinely determined from Chemical Actinometry, with the absorbance spectrum of the catalyst, from the material's diffuse reflectance. This can be used to show that the efficiency of the reaction follows the diffuse reflectance of the catalyst over a range of wavelengths, for example Domen's $(Ga_{1-x}Zn_x)(N_{1-x}O_x)$/Cr-Rh system;[38] although this is now seen quite frequently in photocatalytic literature, in the majority of cases, it is not shown.

Particularly for dye degradation reactions, where the dye in addition absorbs visible light, providing an action spectrum is important.[29] As discussed in Chapter 2, methyl orange is used as a model dye for photocatalytic reactions, with its stability under visible light being a key factor in it's usefulness as a way of characterising photocatalytic activity.[68-69] Despite this stability, the dye can undergo degradation by sensitization, with Galindo et al. showing degradation of methyl orange with $TiO_2$ under a laser light source at 442 nm, which provides energy less than the band gap energy of $TiO_2$;[70] a similar conclusion can be reached from the action spectrum carried out by Clark et al. with the $Pt/CaCu_3Ti_4O_{12}$ material when reacted under visible light with methyl orange.[67] Ohtani demonstrated that although S doped $TiO_2$ successfully degraded AcOH into $CO_2$, with an action spectrum confirming this, visible light Methylene Blue degradation by the same catalyst could not be proved, with the action spectrum suggesting that a dye sensitization was taking place;[51] Ohtani notes that such reactions carried out without the analysis of an action spectrum could give false results regarding the visible light photo activity of the catalyst.

## 1.4 Improving the Efficiency of the Photocatalyst

In Osterloh's review on inorganic material used in photocatalysis, it was stated that an ideal target for efficiency of photocatalysts in terms of commercial viability was 10%, noting that as of 2008, a visible light photocatalyst capable of splitting pure water with an

efficiency of greater than 10% has not been found. For UV active photocatalysts, the most efficient pure water splitting photocatalyst in terms of quantum efficiency is La:$NaTaO_3$, synthesised by Kudo, with NiO as a co-catalyst, having a quantum efficiency of 56% in pure water when illuminated with UV radiation.[54] The material is an excellent example of the ways of improving efficiency of a photocatalyst.

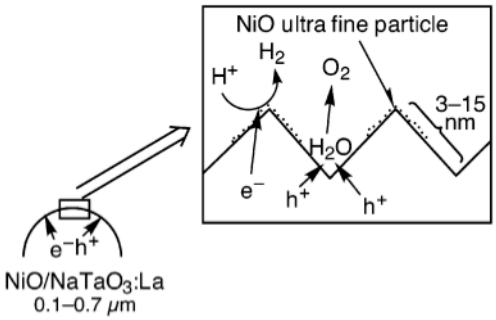


**Figure 1-9** Illustration of water splitting on the NiO/NaTaO3:La particles, showing the hydrogen generation emanating from the NiO fine particles on the surface of NaTaO3:La, and oxygen generation emanating from the grooves of the material. Obtained from the manuscript.[34]

The paper describes how by doping the original photocatalyst $NaTaO_3$ with lanthanum, the particle size decreases from 2 μm – 3 μm to 0.1 – 0.7 μm. This means that there is less chance for electrons and holes produced during illumination to combine, as the distance they have to travel to the surface is reduced; characterisation of the material also showed that the material still remained crystalline, and so minimizing defect sites which could allow electron / hole recombination. By adding NiO as a co-catalyst, the efficiency was enhanced further, by separating the holes and electrons with the NiO attracting the electrons. The lanthanum doping also produced an interesting morphology, with grooves formed on the surface of the material. As demonstrated, this again improved the efficiency by allowing distinct sites for the oxidation reaction deep in the grooves, with the reduction reaction taking place on the NiO co-catalyst on the groove itself (Figure 1-9). The most impressive gain in efficiency however, was the introduction of NiO as a co-catalysts, with

$NiO/NaTaO_3$:La generating over 44 times more hydrogen than the equivalent material without NiO present ($NaTaO_3$:La); using platinum metal nanoparticles as a co-catalyst has a similar effect.

Whilst NiO is used as a co-catalyst in this case, and has been since Domen used it as a co-catalyst for his $SrTiO_3$ material,[71] the vast majority of papers in literature that discuss generation of hydrogen from a photocatalyst use a Platinum Group Metal (PGM) as a co-catalyst to assist in the hydrogen generation reaction; for the oxidation reaction, Platinum Group Metal Oxides, are used as co-catalysts, with $RuO_2$ and $IrO_2$ generally identified as the most successful.[12, 72]

PGMs have played a significant role in photocatalysis, since the landmark paper by Honda and Fujishima generating hydrogen from rutile $TiO_2$ with a platinum electrode. [11] Upon illumination with light greater in energy than the $TiO_2$ band gap, the electrochemical cell, with a single crystal rutile $TiO_2$ as the anode, and platinum electrode at the cathode, produced detectable hydrogen when the two electrodes were connected through an external load, implying water photolysis or water splitting. By directly coupling a semiconductor such as $TiO_2$ with platinum, it was speculated that water splitting could occur upon illumination without the need of an external bias, with the platinum acting as a co-catalyst.[21]

Schrauzer and Guth demonstrated that powdered $TiO_2$, upon illumination with UV light greater than the $TiO_2$ band gap, allows photolysis of chemisorbed water on the surface of the $TiO_2$.[73] When performed under an inactive argon atmosphere, a molar ratio of 2:1 of hydrogen to oxygen is generated, implying a stoichiometric reaction for photolysis of water. However, they also noted the reaction rate was significantly less than that provided for by photoelectrochemical cells, and the rate eventually dropped to close to zero, with this the consequence of the back reaction of hydrogen and oxygen reacting to form water. Further work by Kawai and Sakata confirmed that the hydrogen was coming from water in

the photolysis reaction by using gas phase $D_2O$ as the reactant;[74] $D_2$ was produced upon illumination. The group used $RuO_2$ as a co-catalyst, well known as an electrode for oxygen evolution, with the aim of enhancing the oxygen generated; they found that significantly more hydrogen and oxygen was produced when using $TiO_2$-$RuO_2$ than $TiO_2$ alone, implying the efficiency of both the reduction and oxidation reactions improved, with the group speculating the co-catalyst improved the charge separation of holes and electrons. This paper is also significant as by using $D_2O$, and noting that $D_2$ was generated, the result confirmed that the hydrogen generated was coming from the water solution used; previously in a communication,[75] Van Damme and Hall had speculated that the hydrogen generation reported by Schrauzer and Guth had come from decomposition of hydroxyl groups on the $TiO_2$ surface rather than a photocatalytic process of water splitting.

Kraeutler and Bard, in their 1978 paper,[76] describe the photodeposition of platinum onto the surface of $TiO_2$. Reacting a chloroplatinic acid solution with $TiO_2$, and acetic acid, the platinum (IV) was reduced to platinum (0) upon illumination, with the platinum metal deposited onto the surface of the $TiO_2$. Bard also photodeposited platinum onto tungsten tri-oxide, ($WO_3$), showing the flexibility and adaptability of this photodeposition reaction. This photodeposition method was then used by Sato and White,[77] who used the subsequent Pt-$TiO_2$ catalyst to decompose water under UV light. They noted no evidence of catalytic activity when using $TiO_2$, but found measured catalytic activity for water splitting when the Pt-$TiO_2$ was wet, at a temperature of 23 °C, with both hydrogen and oxygen generated.

Grätzel and his group combined the $RuO_2$ and Pt co-catalysts with $TiO_2$ for water decomposition.[78-79] Loading the $RuO_2$ first to the $TiO_2$ by decomposing $RuO_4$, the material was then photodeposited with Pt under UV light, as described by Bard.[76] The Pt-$TiO_2$-$RuO_2$ produced more hydrogen than just $TiO_2$-$RuO_2$ alone. The Pt-$TiO_2$-$RuO_2$ was also used as a support for dye sensitization reaction under visible light, with $Ru(bpy)_3^{2+}$, a

forerunner to the Gratzel cell developed some years later. Gratzel also used a $Pt/RuO_2$ system with CdS;[80] the group found that CdS on its own does not dissociate water upon illumination; by using $RuO_2$ and Pt both oxygen and hydrogen could be generated under visible light, with the $RuO_2$ found to prevent photo-corrosion of the CdS so improving the stability of the CdS catalyst.

Yamaguti and Sato, having studied the photolysis of water with $Pt\text{-}TiO_2$, turned their attention to other PGMs as co-catalysts, notably rhodium and palladium in addition to platinum.[35] In their experiments, of the 3 PGMs, rhodium, with $Rh\text{-}TiO_2$ gave the highest generation rate of hydrogen, whilst palladium based $Pd\text{-}TiO_2$ gave the lowest rate of hydrogen generation. The group noted however, that the rhodium deposited catalyst was found to be the least active for the back reaction of oxygen and hydrogen forming from water, with palladium also less active for the back reaction when compared with platinum.

From this early work, many semiconductors were developed as photocatalysts for water splitting; all required a co-catalyst to perform to the maximum efficiency, with the vast majority using platinum as the hydrogen generation co-catalyst, with $RuO_2$ generally used as a co-catalyst for oxygen generation. It is perhaps surprising that there are relatively little comprehensive studies of the effects of co-catalysts, particularly PGMs on photocatalysts. As will be discussed in detail in the introduction to Chapter 5, work by Inoue, and in particular work by Ohtani and Bowker are the most detailed studies found.

Inoue and colleagues carried out a survey of co-catalysts including ruthenium, iridium and platinum, on their barium tetratitanate, $BaTi_4O_9$.[81]; a key feature of this work was the study of both the PGM and the PGM oxide itself as co-catalysts. Ohtani et al. presented a detailed analysis of the role of platinum deposits on $TiO_2$ in a paper published in 1997,[82] with the conclusion that only one platinum particle is required for hydrogen generation on a $TiO_2$ particle around 24 nm in size. Michael Bowker's group in a series of papers published from 1999 undertook a similarly detailed analysis of PGMs on $TiO_2$.[83-85]

Concentrating on palladium, the group detailed an interesting reaction mechanism, suggesting the hydrogen is emanating from the photocatalytic degradation of methanol in addition to degradation of water, with the active site for the generation of hydrogen from water located at the periphery of the palladium particle on $TiO_2$, and methanol liberating hydrogen on the palladium particle. The work presented in Chapter 4 of this thesis is structured to provide a similarly detailed characterisation and analysis of a series of PGM co-catalysts on a semiconductor support.

## 1.5 Aim and Scope of the Project

As stated earlier, the overall aim of the project and the work carried out in this thesis was to synthesise 'New Material for Visible Light Photocatalysis'. The simple strategy employed was to synthesise and characterise a simple, high surface area metal oxide that is active in UV light, and then modify this by adding nanoparticles of another metal oxide, inducing charge transfer between the metals of the two oxides (MMCT) utilizing visible light, with work in particular by both Frei and Hashimoto influencing the choice of metals.

The idea of using MMCT to essentially provide a new valence band in this material meant the choice of high surface area UV active support to synthesise first could be reasonably broad – the actual band gap of the material being semi-irrelevant as the band gap would be decreased into the visible region of the spectrum by the addition of the second metal oxide. Niobium (V) oxide ($Nb_2O_5$) was chosen as a support, as opposed to $TiO_2$, due to the higher conduction band potential compared with $TiO_2$, identified by Matsumoto et al.[30] Whilst $TiO_2$ is probably the most studied photocatalyst,[86-87] as discussed in Chapter 3, $Nb_2O_5$ is not so well studied, with work by Ohtani being the most well characterised work on the material.[88] A simple precipitation route was identified to synthesise $Nb_2O_5$,[89] and this route was successfully scaled up, providing a large quantity of material that could be used.

As identified in this chapter, detailed characterisation of PGMs in photocatalysis literature is limited. Therefore the $Nb_2O_5$ synthesised was used for a study of platinum group metals (PGMs), testing platinum, palladium and rhodium by adding them to the $Nb_2O_5$ support. This material was characterised notably by TEM and dispersion measurements, then tested photocatalytically by reacting under UV light with a methanol solution to produce hydrogen. A greater understanding of the PGM addition was achieved, with the simple method of impregnation used to synthesise the PGM added material affording excellent scope for scaling up this material.

The final chapter in this thesis provides perhaps the most interesting results. By adding chromium (III) oxide to the $Nb_2O_5$ support, via a comparable method to the PGM addition, visible light absorbance was achieved. The diffuse reflectance of this chromium / niobium composite was then analyzed in a level of detail not seen in literature, with the key MMCT absorbance identified. This interaction was then used to degrade the model dye Methyl Orange under visible light, with an action spectrum confirming that it is the absorbance of light from the chromium / niobium composite photocatalyst that is driving the reaction, as opposed to a dye sensitization reaction.

In terms of this thesis, the material discussed interacts with light, in the case of the niobium / chromium composite, visible light, with this interaction with light clearly demonstrated by the diffuse reflectance of the material. The material then uses this interaction to drive chemical processes, with these chemical processes demonstrated not to occur in the absence of light, or if the material itself is not present. Whilst material produced for this thesis are not world leaders in terms of efficiency of the reactions, or amount of hydrogen generated / organic material degraded, the simplicity of the synthesis methods used makes the material exceptionally straightforward to reproduce, and the strategy of characterisation, particularly identifying key absorbance features, and proving these responsible for visible light by carrying out an action spectrum, provide a platform of

characterisation that can be used to successfully characterise comparable visible light absorbing material in the future.

## 1.6 References

[1] http://www.astm.org.

[2] http://rredc.nrel.gov/solar/spectra/am1.5/.

[3] B. Ohtani, *Chem. Lett.* **2008**, *37*, 217-229.

[4] T. R. Cook, D. K. Dogutan, S. Y. Reece, Y. Surendranath, T. S. Teets, D. G. Nocera, *Chem. Rev.* **2010**, *110*, 6474-6502.

[5] K. G. McGuigan, T. M. Joyce, R. M. Conroy, *J. Med. Microbiol.* **1999**, *48*, 785-787.

[6] J. Lonnen, S. Kilvington, S. C. Kehoe, F. Al-Touati, K. G. McGuigan, *Water Res.* **2005**, *39*, 877-883.

[7] M. Grätzel, *Nature* **2001**, *414*, 338-344.

[8] L. J. Minggu, W. R. W. Daud, M. B. Kassim, *Int. J. Hydrogen Energy* **2010**, *35*, 5233-5244.

[9] S. Y. Reece, J. A. Hamel, K. Sung, T. D. Jarvi, A. J. Esswein, J. J. H. Pijpers, D. G. Nocera, *Science* **2011**, *334*, 645-648.

[10] N. S. Lewis, D. G. Nocera, *Proc. Natl. Acad. Sci. U.S.A.* **2006**, *103*, 15729-15735.

[11] A. Fujishima, K. Honda, *Nature* **1972**, *238*, 37-38.

[12] F. E. Osterloh, *Chem. Mater.* **2008**, *20*, 35-54.

[13] M. R. Hoffmann, S. T. Martin, W. Y. Choi, D. W. Bahnemann, *Chem. Rev.* **1995**, *95*, 69-96.

[14] A. Mills, S. LeHunte, *J. Photochem. Photobiol., A* **1997**, *108*, 1-35.

[15] D. S. Bhatkhande, V. G. Pangarkar, A. A. C. M. Beenackers, *J. Chem. Technol. Biotechnol.* **2002**, *77*, 102-116.

[16] K. Rajeshwar, M. E. Osugi, W. Chanmanee, C. R. Chenthamarakshan, M. V. B. Zanoni, P. Kajitvichyanukul, R. Krishnan-Ayer, *J. Photochem. Photobiol., C* **2008**, *9*, 171-192.

[17] K. Domen, J. N. Kondo, M. Hara, T. Takata, *Bull. Chem. Soc. Jpn.* **2000**, *73*, 1307-1331.

[18] J. S. Lee, *Catal. Surv. Asia* **2005**, *9*, 217-227.

[19] A. Kudo, Y. Miseki, *Chem. Soc. Rev.* **2009**, *38*, 253-278.

[20] X. B. Chen, S. H. Shen, L. J. Guo, S. S. Mao, *Chem. Rev.* **2010**, *110*, 6503-6570.

[21] K. Maeda, *J. Photochem. Photobiol., C* **2011**, *12*, 237-268.

[22] Y. Shiraishi, T. Hirai, *J. Photochem. Photobiol., C* **2008**, *9*, 157-170.

[23] M. Sakamoto, M. Fujistuka, T. Majima, *J. Photochem. Photobiol., C* **2009**, *10*, 33-56.

[24] B. O'Regan, M. Grätzel, *Nature* **1991**, *353*, 737-740.

[25] A. Hagfeldt, G. Boschloo, L. C. Sun, L. Kloo, H. Pettersson, *Chem. Rev.* **2010**, *110*, 6595-6663.

[26] A. W. Hains, Z. Q. Liang, M. A. Woodhouse, B. A. Gregg, *Chem. Rev.* **2010**, *110*, 6689-6735.

[27] H. J. Zhang, G. H. Chen, D. W. Bahnemann, *J. Mater. Chem.* **2009**, *19*, 5089-5121.

[28] J. M. Herrmann, *Appl. Catal., B* **2010**, *99*, 461-468.

[29] B. Ohtani, *J. Photochem. Photobiol., C* **2010**, *11*, 157-178.

[30] Y. Matsumoto, *J. Solid State Chem.* **1996**, *126*, 227-234.

[31] M. D. Ward, J. R. White, A. J. Bard, *J. Am. Chem. Soc.* **1983**, *105*, 27-31.

[32] J. C. Zhao, C. C. Chen, W. H. Ma, *Top. Catal.* **2005**, *35*, 269-278.

[33] H. J. Kuhn, S. E. Braslavsky, R. Schmidt, *Pure Appl. Chem.* **2004**, *76*, 2105-2146.

[34] H. Kato, K. Asakura, A. Kudo, *J. Am. Chem. Soc.* **2003**, *125*, 3082-3089.

[35] K. Yamaguti, S. Sato, *J. Chem. Soc., Faraday Trans. 1 F* **1985**, *81*, 1237-1246.

[36] Z. G. Zou, H. Arakawa, *J. Photochem. Photobiol., A* **2003**, *158*, 145-162.

[37] R. Abe, T. Takata, H. Sugihara, K. Domen, *Chem. Commun.* **2005**, 3829-3831.

[38] K. Maeda, K. Teramura, D. L. Lu, T. Takata, N. Saito, Y. Inoue, K. Domen, *Nature* **2006**, *440*, 295-295.

[39] T. Ohno, L. Bai, T. Hisatomi, K. Maeda, K. Domen, *J. Am. Chem. Soc.* **2012**, *134*, 8254-8259.

[40] J. Nowotny, C. C. Sorrell, T. Bak, L. R. Sheppard, *Sol. Energy* **2005**, *78*, 593-602.

[41] R. Asahi, T. Morikawa, T. Ohwaki, K. Aoki, Y. Taga, *Science* **2001**, *293*, 269-271.

[42] *From Web of Science Citation search*.

[43] H. G. Kim, D. W. Hwang, J. S. Lee, *J. Am. Chem. Soc.* **2004**, *126*, 8912-8913.

[44] M. Pelaez, A. A. de la Cruz, K. O'Shea, P. Falaras, D. D. Dionysiou, *Water Res.* **2011**, *45*, 3787-3796.

[45] R. G. Palgrave, D. J. Payne, R. G. Egdell, *J. Mater. Chem.* **2009**, *19*, 8418-8425.

[46] G. Hitoki, T. Takata, J. N. Kondo, M. Hara, H. Kobayashi, K. Domen, *Chem. Commun.* **2002**, 1698-1699.

[47] M. Hara, J. Nunoshige, T. Takata, J. N. Kondo, K. Domen, *Chem. Commun.* **2003**, 3000-3001.

[48] G. Hitoki, A. Ishikawa, T. Takata, J. N. Kondo, M. Hara, K. Domen, *Chem. Lett.* **2002**, 736-737.

[49] S. U. M. Khan, M. Al-Shahry, W. B. Ingler, *Science* **2002**, *297*, 2243-2245.

[50] T. Umebayashi, T. Yamaki, H. Itoh, K. Asai, *Appl. Phys. Lett.* **2002**, *81*, 454-456.

[51] X. Yan, T. Ohno, K. Nishijima, R. Abe, B. Ohtani, *Chem. Phys. Lett.* **2006**, *429*, 606-610.

[52] J. Yoshimura, Y. Ebina, J. Kondo, K. Domen, A. Tanaka, *J. Phys. Chem.* **1993**, *97*, 1970-1973.

[53] X. C. Wang, K. Maeda, A. Thomas, K. Takanabe, G. Xin, J. M. Carlsson, K. Domen, M. Antonietti, *Nat. Mater.* **2009**, *8*, 76-80.

[54] A. Kudo, *MRS Bull.* **2011**, *36*, 32-38.

[55] K. Teramura, K. Maeda, T. Saito, T. Takata, N. Saito, Y. Inoue, K. Domen, *J. Phys. Chem. B* **2005**, *109*, 21915-21921.

[56] K. Maeda, K. Teramura, D. L. Lu, T. Takata, N. Saito, Y. Inoue, K. Domen, *J. Phys. Chem. B* **2006**, *110*, 13753-13758.

[57] K. Maeda, K. Teramura, N. Saito, Y. Inoue, K. Domen, *J. Catal.* **2006**, *243*, 303-308.

[58] K. Maeda, K. Teramura, D. L. Lu, N. Saito, Y. Inoue, K. Domen, *J. Phys. Chem. C* **2007**, *111*, 7554-7560.

[59] K. Maeda, K. Teramura, K. Domen, *Catal. Surv. Asia* **2007**, *11*, 145-157.

[60] K. Maeda, A. K. Xiong, T. Yoshinaga, T. Ikeda, N. Sakamoto, T. Hisatomi, M. Takashima, D. L. Lu, M. Kanehara, T. Setoyama, T. Teranishi, K. Domen, *Angew. Chem. Int. Ed.* **2010**, *49*, 4096-4099.

[61] J. Barber, *Chem. Soc. Rev.* **2009**, *38*, 185-196.

[62] Y. Sasaki, H. Nemoto, K. Saito, A. Kudo, *J. Phys. Chem. C* **2009**, *113*, 17536-17542.

[63] H. J. Yun, H. Lee, N. D. Kim, D. M. Lee, S. Yu, J. Yi, *ACS Nano* **2011**, *5*, 4084-4090.

[64] H. Tada, T. Mitsui, T. Kiyonaga, T. Akita, K. Tanaka, *Nat. Mater.* **2006**, *5*, 782-786.

[65] W. Y. Lin, H. Frei, *J. Am. Chem. Soc.* **2005**, *127*, 1610-1611.

[66] H. Irie, S. Miura, R. Nakamura, K. Hashimoto, *Chem. Lett.* **2008**, *37*, 252-253.

[67] J. H. Clark, M. S. Dyer, R. G. Palgrave, C. P. Ireland, J. R. Darwent, J. B. Claridge, M. J. Rosseinsky, *J. Am. Chem. Soc.* **2011**, *133*, 1016-1032.

[68] G. T. Brown, J. R. Darwent, *J. Chem. Soc., Faraday Trans. 1 F* **1984**, *80*, 1631-1643.

[69] G. T. Brown, J. R. Darwent, *J. Phys. Chem.* **1984**, *88*, 4955-4959.

[70] C. Galindo, P. Jacques, A. Kalt, *J. Photochem. Photobiol., A* **2000**, *130*, 35-47.

[71] K. Domen, S. Naito, M. Soma, T. Onishi, K. Tamaru, *J. Chem. Soc., Chem. Commun.* **1980**, 543-544.

[72] A. Harriman, I. J. Pickering, J. M. Thomas, P. A. Christensen, *J. Chem. Soc., Faraday Trans. 1 F* **1988**, *84*, 2795-2806.

[73] G. N. Schrauzer, T. D. Guth, *J. Am. Chem. Soc.* **1977**, *99*, 7189-7193.

[74] T. Kawai, T. Sakata, *Chem. Phys. Lett.* **1980**, *72*, 87-89.

[75] H. Van Damme, W. K. Hall, *J. Am. Chem. Soc.* **1979**, *101*, 4373-4374.

[76] B. Kraeutler, A. J. Bard, *J. Am. Chem. Soc.* **1978**, *100*, 4317-4318.

[77] S. Sato, J. M. White, *Chem. Phys. Lett.* **1980**, *72*, 83-86.

[78] D. Duonghong, E. Borgarello, M. Grätzel, *J. Am. Chem. Soc.* **1981**, *103*, 4685-4690.

[79] E. Borgarello, J. Kiwi, E. Pelizzetti, M. Visca, M. Grätzel, *J. Am. Chem. Soc.* **1981**, *103*, 6324-6329.

[80] K. Kalyanasundaram, E. Borgarello, D. Duonghong, M. Grätzel, *Angew. Chem. Int. Ed.* **1981**, *20*, 987-988.

[81] Y. Inoue, Y. Asai, K. Sato, *J. Chem. Soc., Faraday Trans.* **1994**, *90*, 797-802.

[82] B. Ohtani, K. Iwai, S.-i. Nishimoto, S. Sato, *J. Phys. Chem. B* **1997**, *101*, 3349-3359.

[83] A. Dickinson, D. James, N. Perkins, T. Cassidy, M. Bowker, *J. Mol. Catal. A: Chem.* **1999**, *146*, 211-221.

[84] L. Millard, M. Bowker, *J. Photochem. Photobiol., A* **2002**, *148*, 91-95.

[85] L. S. Al-Mazroai, M. Bowker, P. Davies, A. Dickinson, J. Greaves, D. James, L. Millard, *Catal. Today* **2007**, *122*, 46-50.

[86] A. Fujishima, T. N. Rao, D. A. Tryk, *J. Photochem. Photobiol., C* **2000**, *1*, 1-21.

[87] O. Carp, C. L. Huisman, A. Reller, *Prog. Solid State Chem.* **2004**, *32*, 33-177.

[88] H. Kominami, K. Oki, M. Kohno, S. Onoue, Y. Kera, B. Ohtani, *J. Mater. Chem.* **2001**, *11*, 604-609.

[89] N. Uekawa, T. Kudo, F. Mori, Y. J. Wu, K. Kakegawa, *J. Colloid Interface Sci.* **2003**, *264*, 378-384.

# 2 Experimental Methods

As described in the introduction, this Ph.D. thesis is predominantly based on niobium oxide ($Nb_2O_5$) based material, both the synthesis of the $Nb_2O_5$ and related material, and the characterisation of this material. In order to appropriately compare the properties of the material prepared, key characterisation protocols were developed.

This experimental methods section, in addition to describing experimental techniques used in the characterisation of the material such as x-ray photoelectron spectroscopy (XPS) and x-ray diffraction (XRD), also discusses the development of methods used to determine the properties of the material; notably the development of protocols for measuring the hydrogen generated in photocatalytic reactions as well as benchmarking the results, and developing a method to accurately measure the dispersion of platinum group metals on support particles, with the aim of measuring the dispersion of minute amounts of PGMs on supported particles.

## 2.1 Hydrogen Generation

One of the most desirable applications for photocatalysts is the generation of hydrogen from water. Therefore testing photocatalysts for hydrogen generation is a key characterisation technique. Whilst pure water splitting is studied and reported in literature, with both hydrogen and oxygen being formed, the majority of experiments performed for this thesis in terms of hydrogen generation investigated the reduction part of the water splitting reaction, with the oxidation reaction taking place with sacrificial reagents. As with experiments performed by the Bowker group,[1] and the Ohtani group,[2] hydrogen generation was performed by using methanol as a sacrificial reagent, to limit the oxidation of water to oxygen, and so allow hydrogen to be generated without oxygen and the back reaction of oxygen and hydrogen to water.

### 2.1.1 Standard Hydrogen Generation Protocol

The hydrogen generation reactions described in this thesis were all carried out using identical protocol. A 20% methanol / 80% water solution was prepared separately, by adding 100 ml of HPLC grade methanol to a 500 ml volumetric flask, then making up to the 500 ml mark with deionized water. 100 ml of this solution were added to a reactor, in addition to 0.1 g of the catalyst. The reactor was then sealed with a super-seal septum, and completely covered with aluminum foil to ensure the solution with the catalyst were in the dark. With the septum in place, the total volume of the reactor including liquid and gas phase was 110 ml, therefore a total gas phase of 10 ml. This reactor was then purged with nitrogen for 40 min to ensure that the solution was anaerobic, and the gas phase consisted of nitrogen. Before the start of the reaction, a lockable gas-tight syringe was used to take 0.2 ml of the gas phase of the reactor; this was then injected into a gas chromatograph (Varian 4000), with a TCD detector, with nitrogen as the carrier gas. With the TCD measuring the difference between thermal conductivity of gasses, nitrogen should therefore be undetectable on the GC. The GC graph was checked to ensure no peak was detected, i.e. air had been purged from the reactor. The reactor was then placed under a 300 W Xe light source (Oriel) with a infra-red filter attached to remove infra-red radiation. If visible light was required for the reaction, a 420 nm cut off filter was attached to the light source, in front of the infra-red filter. A photograph of the equipment is illustrated in Figure 2-1. At suitable times, the gas phase was again sampled with the lockable gas-tight syringe, with 0.2 ml of gas phase removed, and injected into the GC. A peak at a retention time of 0.38 minutes, indicative of hydrogen, was recorded.

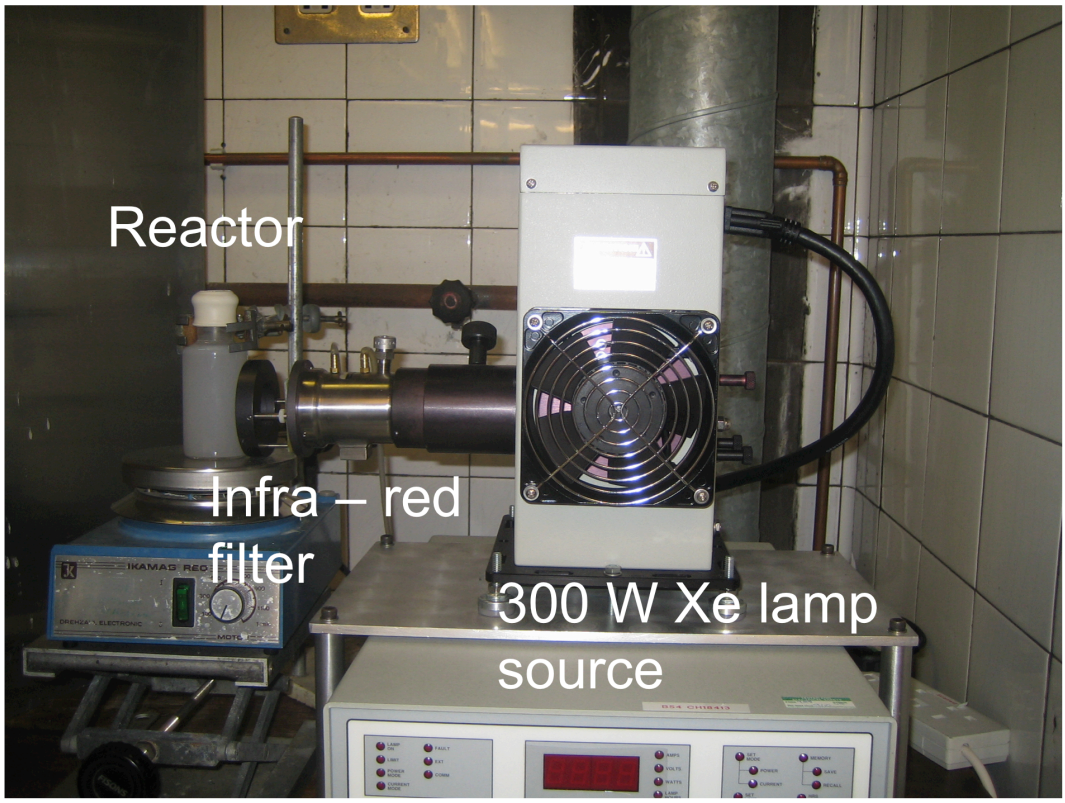


**Figure 2-1** Photograph of the equipment used in hydrogen generation experiments.

A calibration curve was produced to convert the area of the peak into amount of hydrogen. Measured volume amounts of hydrogen were injected into the GC using the lockable gas tight syringe, with a peak appearing at 0.38 minutes retention time on the GC spectra, and no other peaks identified after running for 20 minutes. With the TCD measuring differences in conductivity between nitrogen and another gas, the consistent retention time of pure hydrogen indicated that the retention time of hydrogen was 0.38 minutes with the column used; the intensity of the peak, and so the area under the peak, is indicative of the amount of hydrogen injected. Each volume was injected into the GC 20 times to ensure consistency, and an average of the 20 area values was used to provide a point on the calibration curve graph for the particular volume. The calibration curve used is plotted in Figure 2-2.

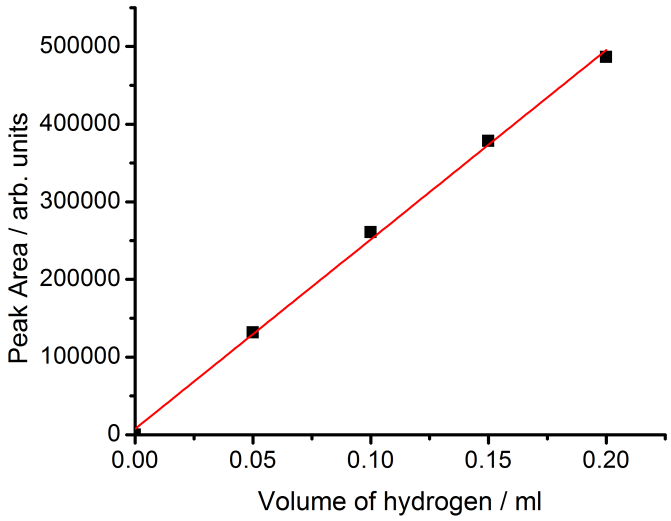


**Figure 2-2** Calibration curve used in hydrogen generation measurements, showing the relationship between the volume of hydrogen injected, and the area of the graph of the peak at a retention time of 0.38 minutes; $R^2$ value 0.998.

Using this calibration curve, the area of the peak at a retention time of 0.38 minutes of samples injected can be converted to the actual amount of hydrogen injected into the GC from the 0.2 ml sample. Scaling this up to the volume of gas phase gives the total amount of hydrogen in the gas phase of the reactor vessel i.e. the total amount of hydrogen produced in ml. To convert to moles, the ideal gas equation was used. The value reported, generally given in µmol, is the total amount in µmol of the hydrogen in the gas phase of the reactor at that point in the reaction.

### 2.1.2 Benchmarking of Hydrogen Measurements

In order to benchmark the hydrogen generation set up described, a comparison was carried out between the set up in Liverpool University, described in Section 2.1.1, and the setup used by Michael Bowker's group in Cardiff University, used successfully in a number of publications.[1, 3-6] The Bowker group used a comparable set up to Liverpool, utilizing a sealed reactor for photocatalytic experiments, and a gas chromatograph to determine hydrogen content, with samples of the gas phase manually injected into the GC.

Johnson Matthey supplied $TiO_2$ (P25) loaded with 1% by weight platinum, which was used as a test material. 0.1 g of this was reacted using the standard hydrogen generation reaction described in Section 2.1.1, with the exception that 90 ml of methanol solution was used, with 0.09 g of catalyst, due to the amount of hydrogen expected to be produced by the reactive 1%Pt-$TiO_2$. The same material was then tested using the reactor and equipment provided by the laboratory in Cardiff.

In Cardiff, 0.1 g of 1%Pt-$TiO_2$ was added to 100 ml of a 20% methanol / 80% water mixture in a 165 ml round bottomed flask Pyrex reactor. The reactor was sealed, and then purged with argon. A 0.2 ml sample of the gas phase was taken, using a gas tight lockable syringe. This was then injected into a GC, with TCD detector and an argon carrier gas. The peak area at a retention time of 90 s was analyzed for hydrogen content. After ensuring there was no peak, the reactor was placed in front of a 400 W Xe lamp. At suitable time intervals, 0.2 ml of the gas phase of the reactor was taken, and placed into the GC, with the area of the peak at 90 s noted, and converted into ml of hydrogen using a calibration curve comparable to the one produced at Liverpool.

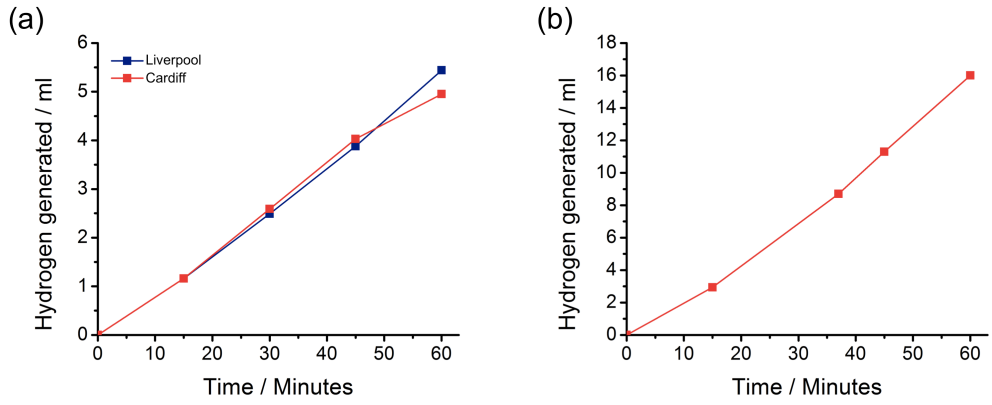


**Figure 2-3** (a) Hydrogen generation results with 1%Pt-$TiO_2$ carried out using equipment at Liverpool and Cardiff laboratories; (b) Hydrogen generation result with 1%Pt-$TiO_2$ carried out using Liverpool reactor with Cardiff light source and GC.

The results of the two experiments are plotted in Figure 2-3(a). Despite the difference in power of the light source, the two results are comparable. A possible reason for this could be the thicker Pyrex glass of the Cardiff reactor compared to the Liverpool reactor (Figure 2-4), with the thicker glass acting as a more effective infrared filter than the thinner Liverpool reactor glass; another factor could be the more efficient stirring of the suspension using the straight Liverpool reactor compared to the more rounded Cardiff reactor. Another test performed was using the Liverpool reactor with the Cardiff lamp and GC; the result shows significantly more hydrogen generated compared to the same reactor at Liverpool Figure 2-3(b). Again the significantly thinner glass of the Liverpool reactor being a less effective infrared shield, in addition to the lack of an infrared filter, and the more powerful 400 W lamp could be significant factors in the increase in hydrogen generation.

### 2.1.3 Henry's Law Considerations

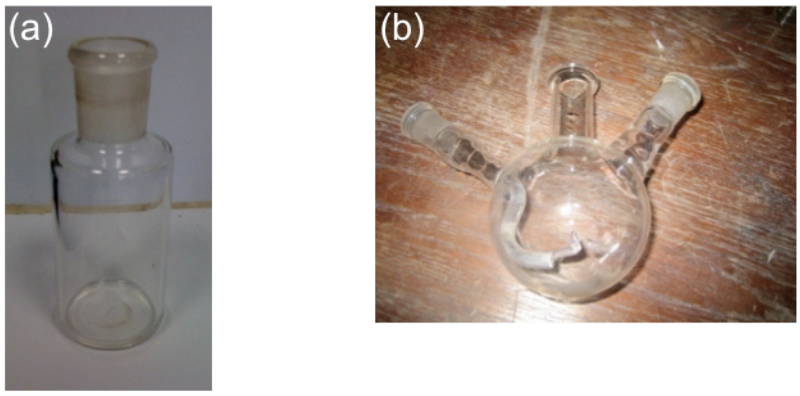


**Figure 2-4** Photographs of the reactor used in Liverpool (a) and the reactor used by the Bowker group in Cardiff (b).

A significant difference in the reactor used in Liverpool, and that used by the Bowker group in Cardiff is the volume of the reactor. After adding 100 ml of solution, the gas phase of the Liverpool reactor is 10 ml, compared to the gas phase of the Cardiff reactor of 65 ml. As the reactor is sealed in order to capture the hydrogen being produced, as the

hydrogen content increases, the pressure of the gas phase also increases. Henry's Law can be used to determine the concentration of hydrogen in solution for a given partial pressure of hydrogen above the solution.

$$p = k_{\mathrm{H}} c$$

**Equation 2-1** Henry's law: $p$ = pressure; $k_{\mathrm{H}}$ = Henry's law constant, depending on solute, solvent and temperature, and $c$ = concentration of the solute.

Therefore with 10 ml of gas phase, after 1 ml (42 μmol) of hydrogen is produced, there is a partial pressure of hydrogen of 0.1 atm. By using the Henry's Law constant of hydrogen in water at 298K as an approximation for the 80% water / 20 % methanol solution (1282.1 L atm $m^{-1}$)[7] the equation can be used to determine that at this pressure, there will be a concentration of hydrogen in solution of 78 μmol $l^{-1}$. With the Cardiff reactor, the partial pressure of hydrogen after producing 1 ml of hydrogen will be significantly less (~0.02 atm), and so the concentration of hydrogen dissolved will be less also, therfore Henry's law is not considered for the majority of experiments preformed at Cardiff; the group notes that if around 1/3 of the gas phase is hydrogen (i.e. around 20 ml of hydrogen is generated), the pressure in the reactor needs to be considered. A comparable system was therefore used in the reactions at Liverpool, with the amount of gas phase tailored to the amount of hydrogen expected by the reaction, so as to complete the reaction when 1/3 of the gas phase volume of hydrogen is generated.

## 2.2 Methyl Orange Degradation

Methyl orange is an azo dye commonly used as a pH indicator in titrations, due to the colour change from orange/yellow in neutral pH, to red in acidic pH. The dye is also used as a model dye for photocatalysis reactions, with increasing numbers of photocatalytic methyl orange papers published since the first reported paper detailing the photo-oxidation and photo-reduction of methyl orange in 1984.[8-9] One of the major advantages of using

methyl orange as a model dye system for visible light photocatalysis, as opposed to for example, methylene blue,[10] is the stability of methyl orange under visible light. The dye undergoes rapid trans – cis photo-isomerization, and as a result, has short excited state lifetimes,[11] eliminating the self-degradation of the dye.[8] This indicates the dye is stable under light, allowing the success of visible light photocatalysts to be determined more effectively, with degradation of methyl orange under visible light due to the presence of the photocatalyst. As will be described, an action spectrum can further be used to define the type of interaction taking place between the dye and photocatalyst, indicating a dye sensitization reaction, or a visible light photocatalytic reaction with the photocatalyst absorbing visible light and producing holes and electrons responsible for the degradation.

In this thesis, methyl orange dye degradation reactions were carried out at neutral pH under both UV/Vis light, and visible light. In addition, reactions were carried out using the red protonated form of methyl orange, using visible light, with the dye dissolved at acidic pH. The usefulness of methyl orange as a pH indictor is due to the colour change from basic / neutral to acidic pH; this colour change is accompanied by a change in the UV/Vis spectra from neutral to acidic pH. In terms of monitoring the concentration of the dye from the UV/Vis spectra, it is essential that the pH must remain constant throughout the reaction, therefore dye degradation reactions performed at a acidic pH were carried out in the presence of an acetate buffer to maintain a constant pH, with the pH monitored throughout the reaction.

The standard protocol used in methyl orange degradation reactions testing the materials synthesised is discussed below.

### 2.2.1 Neutral pH Methyl Orange Degradation Reactions

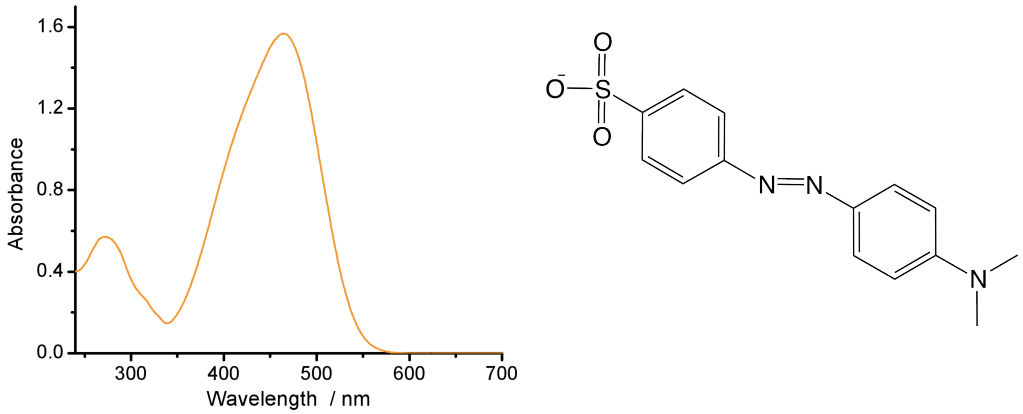


**Figure 2-5** UV/Vis absorbance of the yellow/orange unprotonated methyl orange, and the structure. The extinction coefficient for this compound is 2.68 x $10^4$ $dm^3$ $mol^{-1}$ $cm^{-1}$.[8]

Methyl orange solution was prepared by dissolving 0.02 g (6.11 x $10^{-5}$ M) of solid methyl orange in 1 L of deionized water (pH 6.9) to give a 6.11 x $10^{-5}$ M concentration of methyl orange. The methyl orange solution was stable for a period of months, with no loss in concentration noted. The UV/Vis spectrum of the solution had a characteristic spectrum, with a peak at 465 nm (Figure 2-5).

Methyl orange degradation reactions with catalysts were carried out under UV/Vis or visible light. 100 ml of the 6.11 x $10^{-5}$ M methyl orange solution was placed in a Pyrex reactor, along with 0.1 g of catalyst. Oxygen was bubbled in the reactor at a constant rate; this ensured the reaction suspension was continually saturated with oxygen. Typically the reaction suspension was allowed to equilibrate in the dark under oxygen for one hour. The reaction was initiated by turning on the 300W Xe lamp (Oriel). Under UV/Vis conditions, the light was shone on the reactor with a water based IR filter. When carried out under visible light conditions, additionally a 420 nm cut off filter was placed in front of the IR filter. At points in the reaction, the light was turned off, and approximately 8 ml of sample was removed from the reactor. The catalyst was filtered from the reaction suspension using

0.2 μm GMP membrane filters, and 3 x 2 ml samples were measured by UV/Vis spectroscopy, using a Perkin-Elmer Lambda 650 S UV/vis spectrometer. A 1 cm path length cell was used, and the spectrum was measured from 240 nm – 700 nm. The absorbance at wavelength 465 nm was noted; typically, the three measurements for each sample were averaged. The data was routinely plotted as $A/A_0$, with A being the absorbance at 465 nm of the sample, and $A_0$ being the absorbance at 465 nm of the initial methyl orange solution before catalyst was added. The methyl orange solution was then recombined with the catalyst filtered out from the reactor, and this suspension was placed back in the reactor; the light was then turned on, and the reaction continued.

### 2.2.2 Acid pH Methyl Orange Degradation Reactions

A comparable procedure was used for the degradation of protonated methyl orange under visible light. A 0.010 M acetate buffer solution was prepared, by dissolving 0.5685 g of acetic acid, and 0.0725 g of sodium acetate in 1 L of deionized water (pH 6.9), to generate a pH 3.5 buffer solution. A pH meter confirmed the pH of this buffer solution to be 3.50. UV/Vis spectroscopy of this clear buffer solution shows no absorbance between the range 240 to 700 nm. To this 1 L solution, 0.02 g of methyl orange was dissolved, producing the protonated form of methyl orange, with its characteristic red colour ($6.11 \times 10^{-5}$ M). As with the unprotonated form, this solution was stable for a period of months, with no loss in concentration. The UV/Vis spectrum of this red solution showed a shift in absorbance compared to the yellow/orange solution, with the maximum absorbance in the spectrum of the buffered methyl orange solution occurring at 495 nm (Figure 2-6).

The visible light degradation of the protonated methyl orange solution was carried out in an identical procedure to the unprotonated form, with the only difference being the absorbance at wavelength 495 nm noted to deduce $A/A_0$ for the point in reaction being measured. The pH was monitored and found to be at a pH of 3.50 +/– 0.05 throughout all degradation reactions with the unprotonated form of methyl orange.

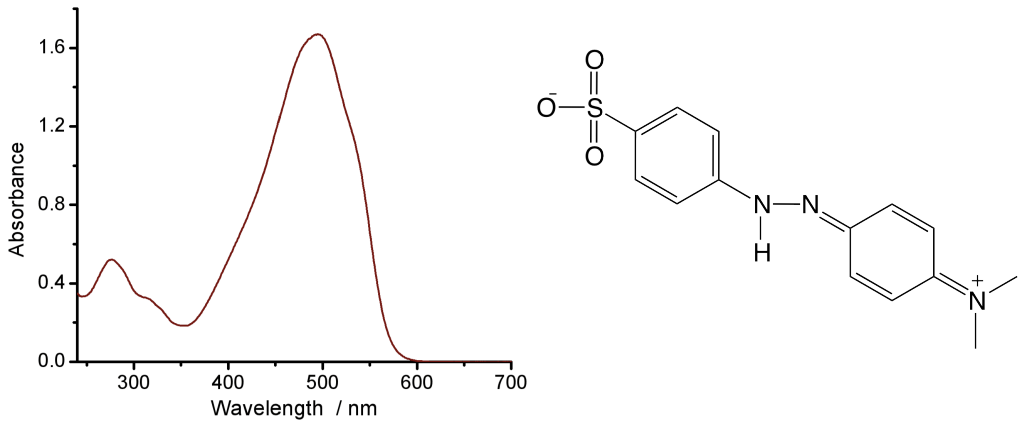


**Figure 2-6** UV/Vis absorbance of methyl orange, dissolved in acetate buffer at pH 3.5, and the structure of the red form of methyl orange; extinction coefficient 4.57 x $10^4$ $dm^3$ $mol^{-1}$ $cm^{-1}$.[8]

## 2.3 Diffuse Reflectance

The key characterisation technique in terms of determining whether solid material synthesised is able to absorb light in the UV or visible region of the electromagnetic spectrum can be found from the optical absorption of the material, determined from the optical absorption coefficient as a function of the energy of photon corresponding to wavelengths of light. As transmission in solid powder samples is very low, the actual absorption coefficient cannot be measured directly. The Kubelka Munk remission function F($R$) is used to represent the absorption coefficient α, and is calculated from the reflectance of the solid sample, with $s$ the scattering coefficient.

$$\mathrm{F}(R) = \frac{(1-R)^2}{2R} = \frac{\alpha}{s}$$

**Equation 2-2** The Kubelka Munk function

Assuming the scattering coefficient $s$ is constant across the given wavelength range, the function F($R$) is proportional to the absorption coefficient α, and so can represent the absorbance of the solid sample.

The diffuse reflectance of solid material synthesised for this thesis was measured on a Perkin-Elmer Lambda 650 S UV/vis spectrometer equipped with a Labsphere integrating sphere. The powdered sample was ground, then placed in a solid sample holder with a quartz glass window, and placed in the UV/Vis spectrometer. The reflectance was recorded over the spectral range 190 – 900 nm (6.53 – 1.38 eV), with barium sulphate used as a standard for 100% reflectance. The reflectance at each wavelength was converted to F(*R*) using Equation 2-2.

The absorption coefficient as a function of energy can be fitted to a power law relationship at energies greater than the band gap, with *B* as a constant, *Eg* the band gap energy, and *n* taking a value that depends on the nature of the band gap transition, with a linear fit seen for $n = ½$ indicating a direct transition, or a linear fit for $n = 2$ seen for a indirect transition.

$$E\alpha(E) = B(E - E_g)^n, E \geq E_g$$

**Equation 2-3** Power law relationship to determine the band gap

Using this equation, at energy equal to or greater than the band gap of the sample, a plot of $(E\alpha(E))^{1/n}$ vs *E* will be linear, and will intercept the x axis at the value of the band gap, where $E = Eg$. As the Kubelka Munk function can be used to represent the absorption coefficient, α, a plot of $(F(R)xE)^{1/n}$ against *E* will be linear at energies equal or above the band gap of the sample.

In this thesis, the direct band gap was determined by plotting $(F(R)xE)^2$ vs *E*, with F(*R*) determined from the reflectance as described. The linear section of the plot was then fitted to a straight line, and the equation of the straight line calculated, with the intercept of the x-axis (when y = 0) calculated by the formula [– y intercept / gradient = x-axis intercept]. As described, the value of *E* at the intercept is equal to the direct band gap energy. The indirect band gap was determined by a comparable method, by plotting $(F(R)xE)^{1/2}$ vs *E*, with the intercept equal to the indirect band gap energy.

## 2.4 Chemical Actinometry

Chemical actinometry is a technique that can be used to determine the moles of photons incident on the reactor emanating from a light source in a photocatalytic reaction. This is achieved by performing a photo-induced reaction that has a known quantum yield at a specific wavelength. Although many such reactions are known,[12] the one selected to be used to determine this for the 300 W Xe lamp was the Potassium Ferrioxalate Chemical Actinometer, based on the work by Hatchard and Parker.[13] In the reaction, iron (III) is reduced to iron (II) by oxalate by light; the iron (II) can then be complexed with phenanthroline, and the concentration of the resulting coloured complex measured by calculation from the absorbance of the complex. By using band-pass filters, light centred on specific wavelengths can be utilized. By using the quantum efficiency that has been previously determined for this reaction at the specific wavelength of light being shone into the reactor,[14] from the moles of iron (II) formed, the moles of photons of light that were required to complete the reduction entering the reactor can be determined; this value is the moles of photons incident on the reactor.

The reaction described was carried out by Joanna Clark, using the 300 W Xe lamp with band pass filters centered at 400 nm, and 450 nm. The calculations gave values of 1.15 x $10^{20}$ photons $h^{-1}$ at 400 nm, and 2.10 x $10^{20}$ photons $h^{-1}$ at 450 nm. By using these values with moles of product degraded per unit time (for methyl orange degradation) or moles of product generated per unit time (for hydrogen or oxygen generation), the quantum efficiency, of these reactions can therefore be calculated. By plotting the quantum efficiencies with the Diffuse Reflectance of the photocatalyst, it can be seen whether the quantum efficiency increases with increasing absorbance of the photocatalyst; this action spectrum can therefore confirm the type of photocatalytic reaction taking place.

## 2.5 PGM dispersion Analysis

A key characterisation technique for identifying how well dispersed a PGM is on a particular support can be carried out using carbon monoxide (CO) adsorption, taking into account the fact that CO adsorbs onto reactive platinum group metal (PGM) surfaces. Assuming a 1:1 ratio of moles of CO to moles of PGM; that one molecule of CO will adsorb onto one active site of PGM, if pulses are passed over the PGM added material, the amount of CO adsorbed will give an indication of how much of the PGM is available. This, quoted as a percentage of total PGM available, is therefore a great technique for determining how successful the PGM addition has been; a high dispersion indicates that much of the PGM is available to be used in catalysis; a low dispersion indicates the much of the PGM is not available to be used in the catalysis reaction.

PGM work for this thesis was carried out at the research center of Johnson Matthey at Sonning Common (JMTC), with the assistance of Dr. Andrew Steele.

In the standard Dispersion Analysis reaction, 0.20 g of PGM added material was placed in a reactor, with an inlet and outlet to allow gas to pass through the reactor. The reactor was placed in a furnace, and a mixture of 10% hydrogen / 90% argon was passed through the reactor. This was then heated to 300 °C for 10 minutes; the reactor was then allowed to cool back to room temperature. This reduction step ensures that the PGM is in its metallic state. The reactor was purged with helium, and a series of 10 pulses of carbon monoxide (CO) from a column with volume 100 µl was pulsed into the sample. The volume of CO adsorbed by the PGM added material was recorded, and converted into µmol of CO adsorbed. The moles of PGM in samples tested was calculated from the ICP weight percentage of each sample, and so the total dispersion was calculated based as a ratio of the moles of CO adsorbed per unit gram of the sample, and then moles of PGM per unit gram of the sample.

Alternatively, for lower weight percentage of PGM samples, a comparable analysis was carried out, with the amount of sample placed in the reactor ~ 1.5 g, and the volume of the CO pulse was reduced to 50 µl, to ensure a greater percentage of CO pulsed in was adsorbed by the PGM.

A third system was also tried, with a 5 µml pulse of CO used, however the equipment used for dispersion analysis was unable to pulse such a small amount of CO through the reactor, and error messages were recorded. This meant that whilst 1% and 0.5% weight PGM added samples gave reliable results that were repeatable, material with less than 0.5% by weight PGM was unable to be measured accurately for dispersion analysis, with results inconsistent between analysis of the same sample.

For the Dispersion characterisation discussed in this thesis therefore, only results carried out with 1% and 0.5% by added PMGs will be discussed, with the Dispersion results of the lower weight added PGMs being discarded.

## 2.6 Other Characterisation

### 2.6.1 X-Ray Diffraction

Probably the most important and widely used method of characterising crystalline inorganic solids is via x-ray diffraction. From the x-ray diffraction pattern, the identification of a crystalline solid and its structure can take place, in addition to other information such as the size of the primary particles in the solid. X-rays for such diffraction experiments can be produced by bombarding a target such as cobalt with a beam of electrons. This beam will ionize electrons from the K shell of the metal atoms, emitting x-rays as the ionized electron vacancies are filled by electrons from the higher energy $L$ or $M$ levels, with intense $K\alpha_1$, $K\alpha_2$ and $K\beta_1$, $K\beta_2$ radiation resulting from $L - K$ transitions ($K\alpha$) and $M - K$ transitions ($K\beta$). A filter of element (atomic number $Z - 1$) for the metal (atomic number $Z$) will absorb the $K\beta$ emission; a appropriate monochromator

can remove the $K\alpha_2$ radiation, so leaving a $K\alpha$ beam as an x-ray source to interact with the sample.

For the material in this thesis, x-ray diffraction was used as a way of confirming the identification of material, the structure of which has already been determined, and available in a database of known compounds (Powder Diffraction File). Additionally in material where the x-ray diffraction pattern showed distinct peaks, the particle size was calculated by the Scherrer equation.

X-ray diffraction analysis was carried out on a Panalytical X'pert Pro diffractometer. The diffractometer produced X-rays from a cobalt anode operating at 40 kV and 40 mA. $K\alpha$ radiation (with $K\alpha$ = 1.7890 Å) was removed using a germanium monochromator. Diffracted intensities were detected using an X'Celerator X-ray detector, which uses Real Time Multiple Strip (RTMS) technology; the diffractometer was set up in Bragg-Brentano geometry. In typical experiments, the sample under investigation was loaded in a Backloading Sample Holder, which reduces preferred orientation of the grains. Typically the pattern was measured from 10 °2 theta to 70 °2 theta, with a step size of 0.05 °2 theta. In order to determine the phase of the material, the peak data was searched against the PDF2 database.

The average particle size of crystalline material can be estimated from the x-ray diffraction pattern, assuming spherical morphology, by using the Scherrer equation, where B is the full width half maximum (FWHM) of the reflection, L is the linear dimension of the particle, θ is the Bragg angle, and K = 0.93.[15]

$$B = \frac{K\lambda}{L\cos\theta}$$

**Equation 2-4** The Scherrer Equation

## 2.6.2 X-Ray Photoelectron Spectroscopy (XPS)

X-Ray Photoelectron Spectroscopy (XPS) is a technique used to provide information about the chemical environment of the elements at the surface of a substance. In XPS, the sample is irradiated with a beam of high energy x-rays; atoms absorb the photons, and then eject electrons from the core energy levels of the element irradiated. As electrons are strongly scattered by atoms, only the surface layers can be detected, with the kinetic energy of the ejected electrons measured and used to calculate the electron binding energy. With elements providing characteristic binding energies, and so characteristic XPS spectra, XPS analysis can be used to identify the elements present at the surface of a material including the oxidation state of the element. XPS can also be used to investigate the electronic band structure of the filled valance band in the sample by identifying the energy of the electrons in the valence band relative to the Fermi level. As described in the introduction, an aim of the project was to synthesise material that would be able to facilitate visible light charge transfer between metal ions, therefore XPS is a key technique able to identify the oxidation state of these metal ions.

Dr. Robert Palgrave recorded high resolution XPS data on a Scienta ESCA 300 spectrometer located at Daresbury Laboratory, which incorporated a rotating anode Al $K_{\alpha}$ ($h\nu$ = 1486.6 eV) X-ray source and had an effective instrument resolution of 400 meV. The spectrometer was calibrated regularly to set the Fermi edge of a silver reference sample at zero binding energy. Results were plotted as binding energy vs intensity, with the binding energy of the intense peaks used to quantify the elements present and the oxidation state of the element, comparing this binding energy to literature values.

## 2.6.3 BET Method for Calculating Surface Area

A key characterisation technique used in catalysis is the determination of the surface area of material, which can be measured using the BET method. BET theory assumes that gas

molecules physically adsorb on a solid in layers infinitely; there is no interaction between adsorption layer, and Langmuir monolayer adsorption theory can be applied to each layer.[16] The limiting case of an infinite number of adsorbate layers, which provides a reasonable approximation for multilayer adsorbates with more than four layers,[17] yields Equation 2-5, where $v_m$ is the volume of gas adsorbed for monolayer coverage, $p_0$ is the saturation pressure of the adsorptive gas, and $c$ is the BET constant.

$$\frac{p}{v(p_0 - p)} = \frac{1}{v_m c} + \frac{c - 1}{v_m c}\frac{p}{p_0}$$

**Equation 2-5** BET theory expression

A plot of $\frac{p}{v(p_0-p)}$ against $\frac{p}{p_0}$ should be linear over the pressure range measured, and the y intercept of $\frac{1}{v_m c}$ and the gradient $\frac{c-1}{v_m c}$. The value of $v_m$ (the volume of gas adsorbed for monolayer coverage) can therefore be obtained from the intercept and gradient, in addition to $c$, which must be positive. From $v_m$, the surface area can be calculated.

A key requirement for a catalyst is a high number of active sites where the catalysis reaction can take place. The area of surface the catalyst has available therefore is a good indication of the amount of active sites available, with the surface area usually quoted in meters squared per gram ($m^2g^{-1}$). Assuming spherical particles, an estimate for the particle size of material could also be gained from this material.

The 5 point BET surface area was determined using a Quantachrome Nova Gas sorption analyzer. In a typical analysis, 0.20 g of material was placed in a reactor, set up to degas at a temperature of 105 °C overnight. After degassing, the reactor was placed in the sorption analyzer, with nitrogen as the sorption gas, and the BET isotherm measured at 5 points along the linear section of the full adsorbance isotherm ($p/p_0$ = 0.05 to 0.35). The volume of a monolayer of nitrogen adsorbed onto the available surface of the sample was calculated from Equation 2-5, and the surface area in $m^2\ g^{-1}$ was calculated from this value.

Additionally, from the surface area, an estimate of particle size can be calculated. Assuming the primary particles are spheres, the surface area and volume of each individual particle of the material can be calculated, and through the density, the mass of the particle can be determined. From the surface area per gram of material therefore, the size of the particles can be determined using Equation 2-6.

$$\text{Surface Area} = \frac{3 \times 10^3}{\text{density} \times \text{radius}}$$

**Equation 2-6** Equation relating the surface area of material to the radius of the primary particle of the material.

## 2.6.4 Thermogravimetric Analysis and Microanalysis

Thermogravimetric analysis (TGA) is an excellent characterisation tool for determining what is taking place as material is being heated, by measuring the weight of material as the material is being heated. Oxidation of a sample to a higher oxidation state can lead to weight gain; similarly reduction of a sample can lead to weight loss. Additionally, moisture or non-inorganic material can be desorbed on heating with a decrease in weight indicative of this. Processes taking place on heating, including crystalisation, are endothermic or exothermic, therefore a difference in heat between a sample and an inert material on heating can signify a process taking place. For inorganic material synthesised by a precipitation method, TGA is a useful technique for determining the amount of hydroxide or water adsorbed to the surface still remaining after drying, and also determining the temperature at which crystalisation takes place.

Thermogravimetric Analysis was carried out using a TA instruments Q600 SDT simultaneous DSC-TGA. In typical experiments, 0.0400 g of material was placed in an aluminum pan, and then placed in the TGA furnace. The TGA was programed to heat to a temperature at a certain rate, typically 5 °C $min^{-1}$ with the weight of sample recorded, in addition to the heat difference between the sample being measured, and the reference

sample. The data was plotted as % weight loss vs temperature on one axis, and heat difference vs temperature on the other axis.

Complementary to this, microanalysis is a technique to determine the hydrogen, nitrogen and carbon content of material; from this the molecular material present in the sample can be determined. The analysis was carried out on a Thermo EA1112 Flash CHNS-O Analyzer by the departmental service, with results quoted as percentage carbon, nitrogen or oxygen based on the weight of sample.

### 2.6.5 Microscopy (SEM, TEM and EDX)

Scanning electron microscopy (SEM) and transmission electron microscopy (TEM) can give excellent qualitative information about the morphology of the material. Whilst optical microscopy can give a resolution only around the wavelength of light, electron microscopy can give resolution of less than 1 nm. TEM in particular can give a qualitative method of viewing nanoparticles of PGMs on the surface of the support. A complementary quantitative analysis is EDX, which can give information about the elements present in a specimen. A disadvantage of these characterisation techniques however, is the fact that only an extremely limited part of the material is imaged and characterised.

TEM imaging of PGM added samples (characterised in Chapter 4) was carried out at the research center of Johnson Matthey at Sonning Common (JMTC) by Dr. Dogan Ozkaya. For the analysis, a FEI Tecnai F20 TEM/STEM was used. Analysis of the samples was carried out in STEM (scanning transmission electron microscopy) mode with an atomic number sensitive high angle annular dark field (HAADF) detector. High resolution imagining was carried out in HREM (high resolution electron microscopy) mode. EDX analysis was performed on a EDAX EDX detector, running on integrated FEI software. TEM samples were prepared by grinding a small amount of sample between two glass plates. A quantity of this ground material was then transferred to a copper TEM grid, and

this was then transferred to the TEM machine. Typically both TEM imaging and EDX analysis were performed on the same prepared sample in the same session.

SEM imaging was carried out in the Centre for Materials Discovery (CMD) at Liverpool University, using a Hitachi S-4800 scanning electron microscope. Analysis of the sample was performed using a low KV electron beam (3 KV). Typically, the sample was prepared by distributing an amount of powder onto a carbon tab, placed on a SEM sample holder. This sample holder was then coated with gold using splutter deposition, depositing a layer approximately 5 – 10 nm thick of gold.

## 2.7 References

[1] A. Dickinson, D. James, N. Perkins, T. Cassidy, M. Bowker, *J. Mol. Catal. A: Chem.* **1999**, *146*, 211-221.

[2] H. Kominami, K. Oki, M. Kohno, S. Onoue, Y. Kera, B. Ohtani, *J. Mater. Chem.* **2001**, *11*, 604-609.

[3] L. Millard, M. Bowker, *J. Photochem. Photobiol., A* **2002**, *148*, 91-95.

[4] L. S. Al-Mazroai, M. Bowker, P. Davies, A. Dickinson, J. Greaves, D. James, L. Millard, *Catal. Today* **2007**, *122*, 46-50.

[5] H. Bahruji, M. Bowker, P. R. Davies, *Int. J. Hydrogen Energy* **2009**, *34*, 8504-8510.

[6] H. Bahruji, M. Bowker, P. R. Davies, F. Pedrono, *Appl. Catal., B* **2011**, *107*, 205-209.

[7] R. Sadler, http://www.Henrys-Law.org **1999**.

[8] G. T. Brown, J. R. Darwent, *J. Chem. Soc., Faraday Trans. 1 F* **1984**, *80*, 1631-1643.

[9] G. T. Brown, J. R. Darwent, *J. Phys. Chem.* **1984**, *88*, 4955-4959.

[10] X. Yan, T. Ohno, K. Nishijima, R. Abe, B. Ohtani, *Chem. Phys. Lett.* **2006**, *429*, 606-610.

[11] H. Goerner, H. Gruen, D. Schulte-Frohlinde, *J. Phys. Chem.* **1980**, *84*, 3031-3039.

[12] H. J. Kuhn, S. E. Braslavsky, R. Schmidt, *Pure Appl. Chem.* **2004**, *76*, 2105-2146.

[13] C. G. Hatchard, C. A. Parker, *Proc R Soc Lon Ser-A* **1956**, *235*, 518-536.

[14] D. E. Nicodem, O. M. V. Aquilera, *J Photochem* **1983**, *21*, 189-193.

[15] A. L. Patterson, *Phys. Rev.* **1939**, *56*, 972-977.

[16] S. Brunauer, P. H. Emmett, E. Teller, *JACS* **1938**, *60*, 309-319.

[17] J. U. Keller, R. Staudt, *Gas Adsorption Equilibria: Experimental Methods and Adsorptive Isotherms, Springer* **2005**.

# 3 Niobium Oxide

## 3.1 Introduction

In his review of inorganic material used in photochemical water splitting reactions in 2008,[1] Osterloh noted that niobates, extended oxides that contain niobium, are well studied for photocatalysis, particularly water splitting. One of the most well-studied catalysts is $K_4Nb_6O_{17}$, discovered by Domen in 1986.[2] Domen et al. exploit the layered structure of the niobate, which includes a layer consisting of potassium, to utilize ion exchange. Replacing $K^+$ with $H^+$ in this way increases the amount of hydrogen generated when reacted under UV light compared to the unprotonated compound by a factor of 5, with methanol as the sacrificial reagent.

Osterloh, along with Ebina and Mallouk have led research on layered niobates, such as $KCa_2Nb_3O_{10}$, where the layered structure allows exfoliation of the material into nanosheets of $Ca_2Nb_3O_{10}$.[3-6] These sheets can be loaded with platinum or other co-catalysts, and restacked allowing an increase in hydrogen generation efficiency compared to the pre-exfolaition material, with the co-catalyst more integrated into the structure,[3-4] or sensitized with ruthenium complexes,[6] promoting the application of the material in dye sensitized solar cells, comparable to the cells pioneered by O'Regan and Gratzel.[7]

Although not as extensively characterised as a photocatalyst as titanium dioxide ($TiO_2$), niobium oxide ($Nb_2O_5$), is well known as a UV active catalyst.[1] A key similarity between $Nb_2O_5$ and $TiO_2$ is the position of the conduction band and valence bands of the two semiconductors, with the reduction and oxidation potentials of the conduction band and valence band respectively allowing the material to oxidize and reduce water.[8] The larger band gap of niobium oxide implies a greater reduction potential of niobium (IV) compared to titanium (III), with the conduction band of $Nb_2O_5$ at a more negative reduction potential compared to $TiO_2$, illustrated in Figure 3-1.

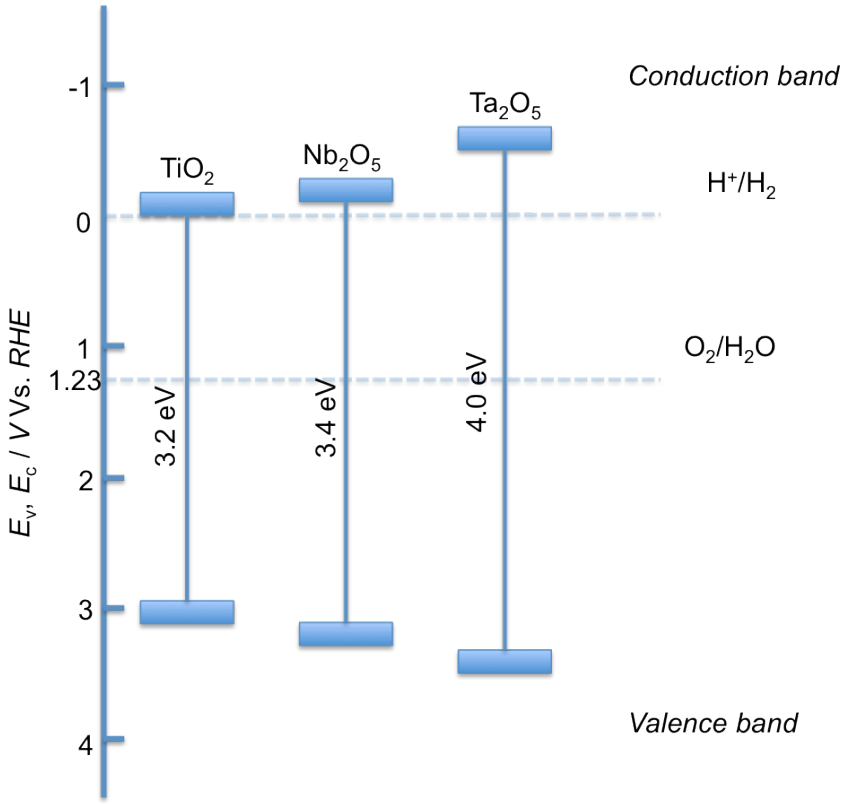


**Figure 3-1** The band gap and conduction and valence band potentials of niobium oxide ($Nb_2O_5$), compared with titanium dioxide ($TiO_2$) and tantalum oxide ($Ta_2O_5$), relative to the reduction and oxidation potential of water ($H^+/H_2$; $O_2/H_2O$).[8]

As with niobiates, $Nb_2O_5$ has been applied to dye sentized solar cell systems.[7] Sayama et al[9] studied the photochemical properties of semiconductor films, including $Nb_2O_5$, $TiO_2$ and tantalum oxide ($Ta_2O_5$), with the films sensitized by a ruthenium (II) complex. The group found that $Nb_2O_5$ had a high monochromatic photon to current (ICPE) efficiency, and the highest open circuit photo voltage out of all the films synthesised, with the group relating this property to the flatband potential of the $Nb_2O_5$ material, promoting the application of $Nb_2O_5$ in the dye sensitized solar cells. Further work by other groups has supported the idea of $Nb_2O_5$ in dye-sensitized solar cells over the past 10 years,[10-12] with the superior flat band potential of $Nb_2O_5$ the key distinction between the material and $TiO_2$.

The photocatalytic properties of $Nb_2O_5$ have also been explored by a number of groups. Kominami et al,[13] in 2001, synthesised $Nb_2O_5$ powder from a solvothermal reaction of

niobium pentabutoxide, and by varying conditions, produced niobium oxide material of various degrees of crystallinity and surface area. Significantly, the most photocatalytically active material for hydrogen generation from a methanol solution was material amorphous from XRD, consisting of a Nb-O-Nb network, characterised by Raman spectroscopy. Although platinum was added as a co-catalyst for the majority of photocatalytic testing, $Nb_2O_5$ without any co-catalyst was also found to produce hydrogen; the paper notes negligible hydrogen generation when $TiO_2$ was used. Ohtani uses this observation to confirm the higher reducing power of $Nb^{V}/Nb^{IV}$ compared to $Ti^{IV}/Ti^{III}$, signified by the higher conduction band potential of $Nb_2O_5$ compared to $TiO_2$.

Based on a novel synthesis method for mesoporous metal oxides first suggested by Yang et al.,[14-15] Chen et al.[16] synthesised mesoporous $Nb_2O_5$; using platinum as a co-catalyst, they induced a greater efficiency of hydrogen generation with methanol solution under UV light with the mesoporous $Nb_2O_5$ compared to the bulk $Nb_2O_5$, with platinum used as a co-catalyst in both cases. They attributed this to the porous network minimizing the photo-generated electrons and holes recombining. The group claims the porous network provides a place for the methanol to react with the photo generated holes, a separate site away from the platinum particles, which are the active site for hydrogen generation. Whilst this explanation may be valid, aside from the significant difference between the hydrogen yields of the bulk and mesoporous material, there is a lack of evidence to support the groups claim of the holes reacting with methanol exclusively in the porous network.

Other groups have utilized $Nb_2O_5$ in photocatalytic degradation reactions. Silva et al,[17] used $Nb_2O_5$ as a semiconductor to degrade textile dyes under UV light, as an alternative to the standard degradation techniques for wastewater, whilst also noting the difficulty in degrading dyes in microbiological treatment. Silver was added as a co-catalyst, which improved the efficiency of the $Nb_2O_5$.

The Prado group published a series of papers from 2004, applying $Nb_2O_5$ based catalysts in organic degradation reactions.[18-20] The group attached $Nb_2O_5$ to a cellulose acetate support to promote easy removal of the catalyst after the reaction is complete, and used it to degrade the model dye indigo carmine.[18] The group improved the system by attaching $Nb_2O_5$ to chitosan, a natural product found in abundance in Brazil, the home country of the group.[19] Whilst the group claimed the role of chitosan was as a support, a more detailed study of the effect of chitosan in the actual degradation reaction was not carried out. $Nb_2O_5$ was also compared to other oxides, again degrading indigo carmine.[20] Although the $Nb_2O_5$ does not compare favorably with zinc oxide (ZnO), and $TiO_2$ in terms of initial reaction rate, the catalyst material was continually recycled; by the $10^{th}$ cycle, both ZnO and $TiO_2$ had lost their effectiveness; $Nb_2O_5$ was still able to degrade the dye with 85% of its initial activity by this point.

From literature therefore, it is clear that $Nb_2O_5$ is an effective UV photocatalyst, although not as well studied as titanium dioxide, with relatively few papers published; also notable is the lack of detailed characterisation and explanations into much of the behavior of the material.

Mesoporous $Nb_2O_5$ can be synthesised via the soft template method first prepared by Yang et al, [14-15] using a niobium precursor with an organic polymer; calcining burns off the polymer, leaving a mesoporous structure. A comparable synthesis was used by Lee et al. to synthesize a three-dimensional ordered mesoporous $Nb_2O_5$.[21] The organic template was removed by calcination, with the mesoporosity dramatically improved by the introduction of a positive cation $Ca^{2+}$. Alternatively, Antonelli and Ying formulated a low temperature synthesis avoiding calcination, by using a niobium precursor with tetradecylamine as the structural directing agent, with this surfactant being removed by treatment with nitric acid.[22]

In addition to the solvothermal route used by Kominami et al, [13] Brayner and Bozon-Verduraz synthesised $Nb_2O_5$ by a soft chemical route.[23] The group synthesised the material, and then calcined at different temperatures, noting the structure of the calcined material from x-ray diffraction, referring back to previous work on the structural phases of $Nb_2O_5$. They noted the polymorphic forms, with amorphous $Nb_2O_5$ existing below 500 °C; between 500 °C – 800 °C the pseudo-hexagonal phase predominates (TT-$Nb_2O_5$), with the orthorhombic phase T-$Nb_2O_5$ at 800 °C – 1000 °C, and finally the high temperature monoclinic phase H-$Nb_2O_5$ at temperatures greater than 1000 °C.[24-27] The phase transitions noted are summarized in Scheme 3-1

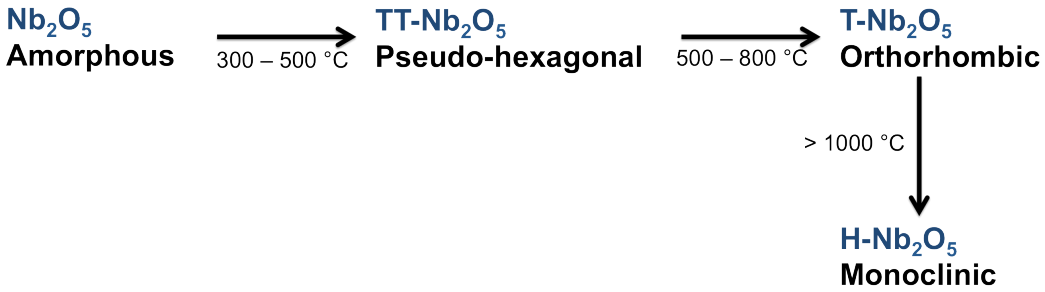


**Scheme 3-1** Scheme showing the various structures of $Nb_2O_5$, and the approximate temperatures the structures change upon calcination. Data taken from Brayner and Bozon-Verduraz, [23] adapted from Jeng and Wachs.[27]

The structure of the highly ordered monoclinic H-$Nb_2O_5$ consists of 6 oxygen atoms attached to a central niobium atom octahedrally; these form 4x3 or 5x3 units of $NbO_6$ octahedra, with the structure of the high temperature H-$Nb_2O_5$ phase consisting of highly ordered sequences of these blocks (Figure 3-2).[24, 26] Similar to the H-$Nb_2O_5$ phase, the less ordered orthorhombic T-$Nb_2O_5$ phase has each Nb atom surrounded by oxygen atoms, however the niobium atoms are surrounded by either 6 or 7 oxygen atoms, forming distorted octahedra or pentagonal bipyramids that are linked by either edge or corner sharing. The low temperature TT-$Nb_2O_5$ pseudo hexagonal phase has a constitutional defect of an oxygen atom per unit cell, and forms tetragonal and pentagonal bipyramids

with 6 or 7 atoms coordinated to a niobium atom. The three crystalline phases of $Nb_2O_5$ are sketched in Figure 3-3.[26]

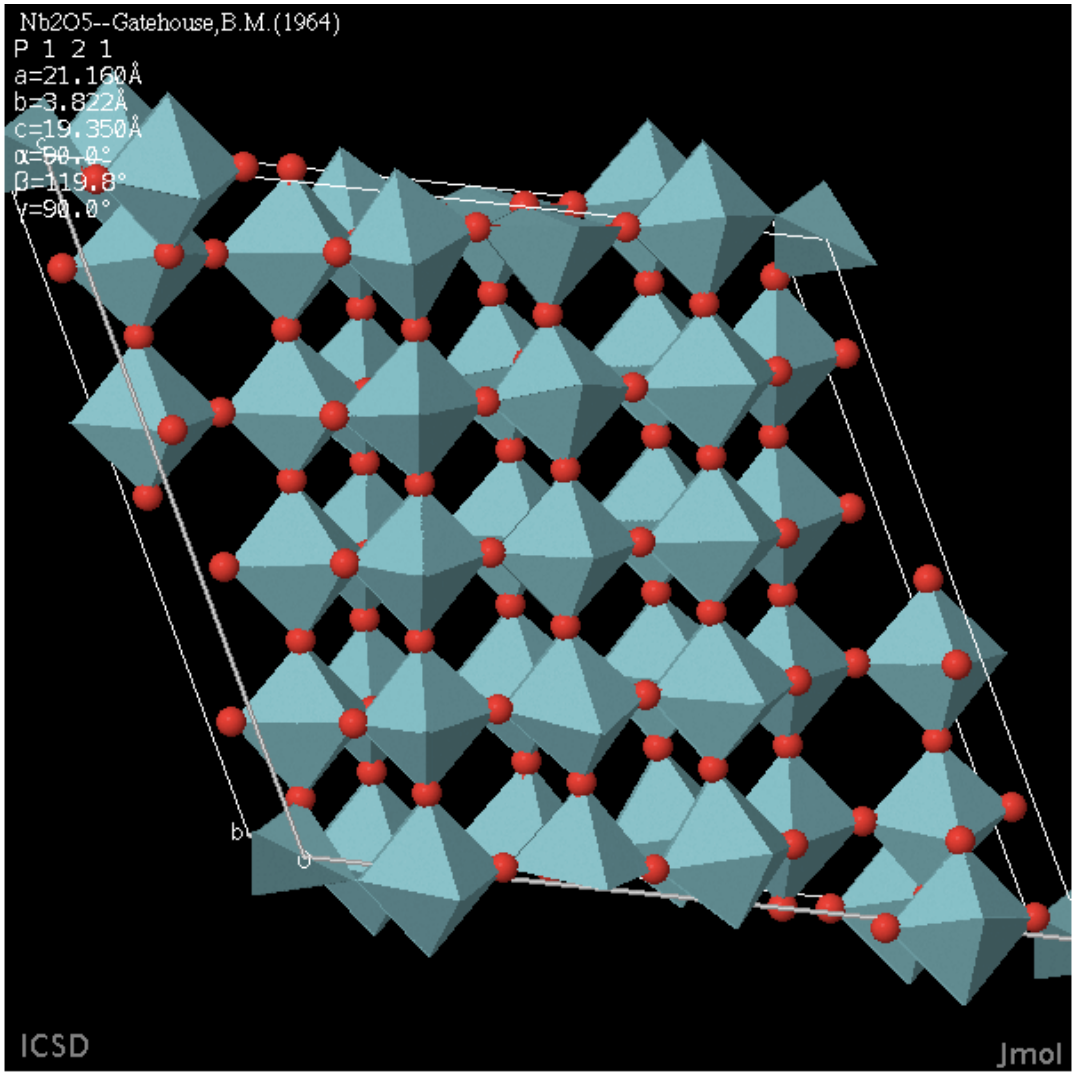


**Figure 3-2** The structure of the high temperature monolclinc phase of $Nb_2O_5$ (H-$Nb_2O_5$), drawn using jmol, data provided by Gatehouse et al.[24]

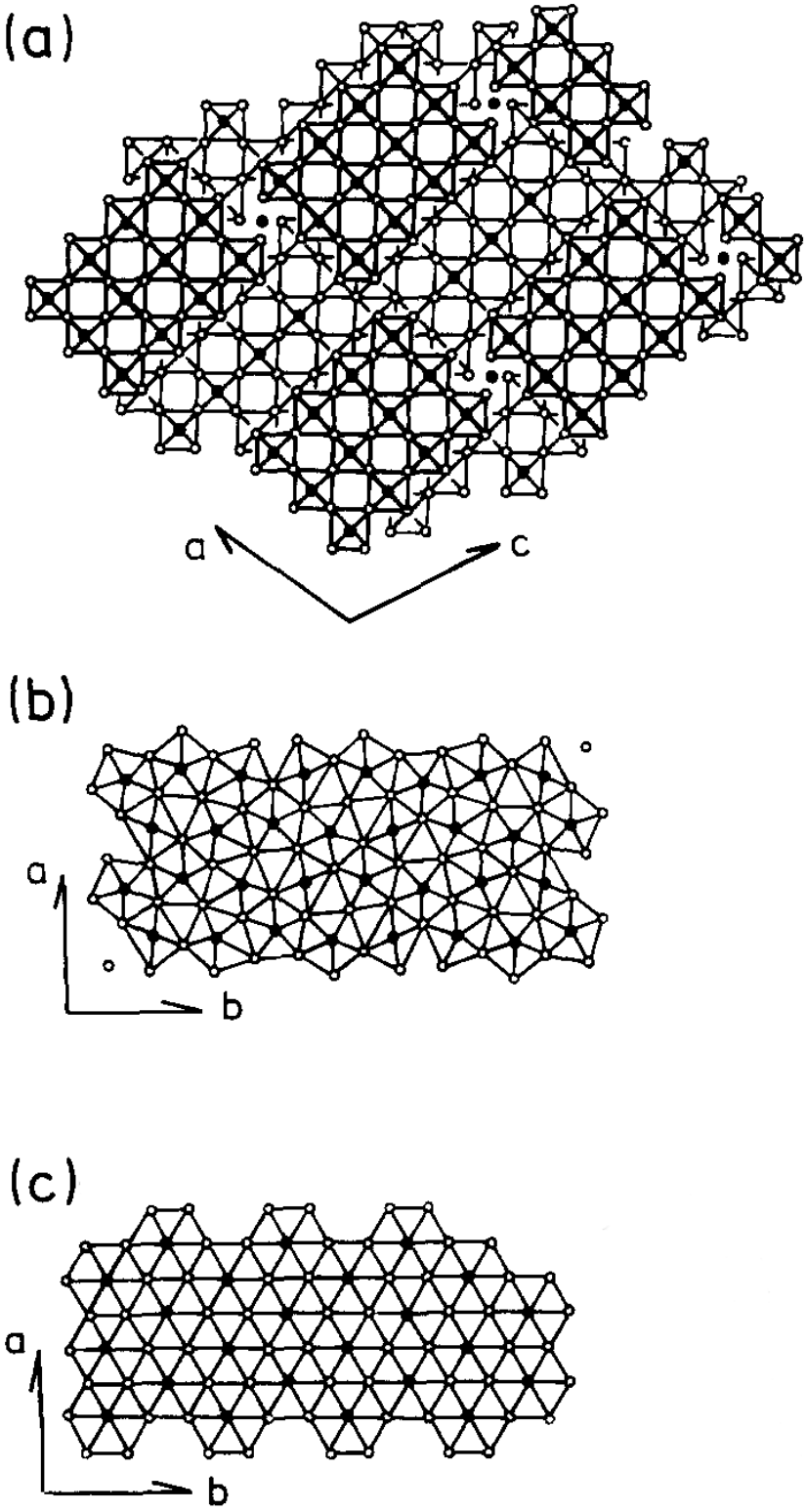


**Figure 3-3** A sketch showing the crystalline phases of $Nb_2O_5$ from Ikeya and Senna:[26] a) shows the H-$Nb_2O_5$ phase; b) shows the T-$Nb_2O_5$ phase in the *ab*-plane; c) shows the TT-$Nb_2O_5$ phase in the ab-plane, with filled circles Nb atoms, unfilled circles O atoms.

Examples of sol-gel film synthesis, for use in applications taking advantage of the electrochromism of $Nb_2O_5$,[28-30] in addition to chemical vapour deposition,[31] pulsed laser deposition of $Nb_2O_5$,[32] and chemical spray pyrolysis,[33] along with routes previously mentioned provide a rich array of methods for synthesising $Nb_2O_5$. However a simple precipitation route, utilized by Uekawa et al. can also be employed,[34] with niobium chloride precipitating nanoparticles of niobium precipitate material when added to a basic solution of ammonia.

In this chapter, $Nb_2O_5$ material was synthesised, with the aim of synthesising material that can be used as the starting point for the two main aims of the project: platinum group metal addition to an oxide, and obtaining visible light active material. Two examples of $Nb_2O_5$ synthesis were chosen: the mesoporous route based on Yang et al.,[14-15] and the nanoparticulate precipitation route, based on Uekawa et al.,[34] with the resulting material fully characterised. Although both the mesoporous and the nanoparticulate routes provided photocatalytic material, the nanoparticulate precipitation route was judged more suitable to scaling up. This precipitation route has a number of variables, and a series of experiments were carried out, altering the variables to produce different $Nb_2O_5$ material, which again was fully characterised. Finally, the most promising of this material was scaled up further, with one batch producing over 200 g of product. The material synthesised in this large scale reaction was comparable to the material fabricated on the much smaller scale initially, implying the synthesis had been successfully scaled up. This fully characterised material was then used as the starting material for platinum group metal addition (Chapter 4) and chromium oxide addition (Chapter 5).

## 3.2 Mesoporous $Nb_2O_5$

As briefly discussed in Section 3.1, Chen et al. synthesised mesoporous $Nb_2O_5$, and after photodepositing with platinum, tested the material for hydrogen generation with methanol as the sacrificial reagent.[16] The material was synthesised using a template technique for

synthesising mesoporous oxides initially published by Yang et al. in Nature (1998),[14] with further characterisation published the following year.[15] The material is synthesised firstly by dissolving the metal precursor, which in the majority of cases is a metal chloride, with a co-block organic polymer already dissolved in anhydrous ethanol. The ethanol is allowed to evaporate; this leaves a gel like material that is aged at a set temperature for a set amount of time. The gel is then calcined at a temperature that removes the organic polymer template, generating a mesoporous oxide material.

### 3.2.1 Synthesis of Mesoporous $Nb_2O_5$

The niobium-based gel was synthesised by firstly dissolving 1 g of Poly(ethylene glycol)-block-poly(propylene glycol)-block-poly(ethylene glycol) with an average $M_n$ of 5,800 [P123 co-block organic polymer], (Sigma Aldrich), in 6 ml of anhydrous ethanol in a 50 ml flask. After the polymer had dissolved, 2.70 g (0.01 mol) of niobium chloride was added to the flask, and allowed to dissolve, leaving a clear, green tinged liquid. The open flask was placed in an oil bath, where the solution was heated to 40 °C; the ethanol was allowed to evaporate off, leaving a lime coloured gel, which was allowed to age at 40 °C for 48 hours. The gel was heated in an oven at 105 °C for 2 hours, then ground into a brown powder (**$NbO_x$-Gel**). **$NbO_x$-Gel** was initially calcined at 350 °C for 2 hours, then ground and split into two. Material was calcined at either 450 °C (**$Nb_2O_5$-450**) or 550 °C, (**$Nb_2O_5$-550**) for three hours. In all calcinations, the material was heated up at 0.5 °C $min^{-1}$, and cooled at 5 °C $min^{-1}$. The synthesis is summarized in Scheme 3-2.

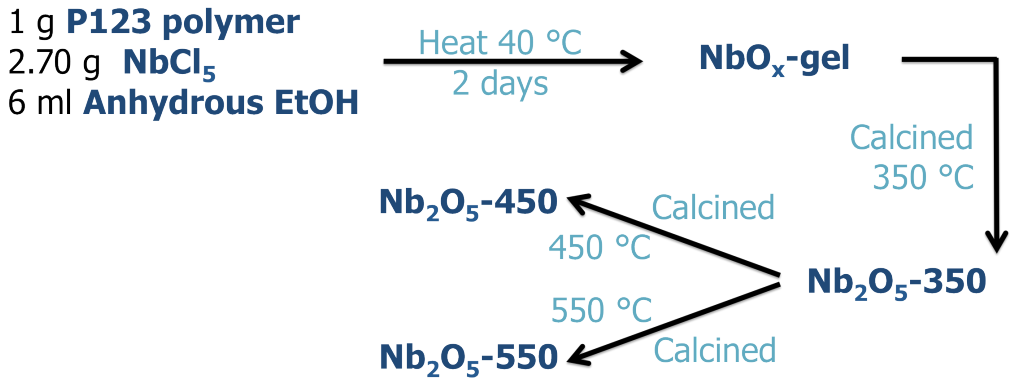


**Scheme 3-2** Schematic showing the synthesis of mesoporous **$Nb_2O_5$-450** and **$Nb_2O_5$-550**, from niobium chloride, P123 co-block organic polymer and anhydrous ethanol.

## 3.2.2 Characterisation of Mesoporous $Nb_2O_5$

Figure 3-4 shows TGA data for **$NbO_x$-Gel,** indicating significant weight loss corresponding to the co-block organic polymer template decomposing and being removed as the temperature increases, leaving just the niobium oxide material as the weight loss concludes. For the experiment, the **$NbO_x$-Gel** in the TGA was heated at the same rate as in the calcination procedure, i.e. 0.5 °C $min^{-1}$. The most intense weight loss occurs before 400 °C, however the weight loss continues up to around 500 °C. Although TGA data for the niobium based material synthesised by Yang et al. is not presented in the paper, the group do present TGA data for comparable zirconium based mesoporous material.[15] As with the data presented in Figure 3-4 for **$NbO_x$-Gel**, using the same co-block organic polymer template as the zirconium material (P123), TGA data presented by the group for the zirconium material shows weight loss up to 500 °C.

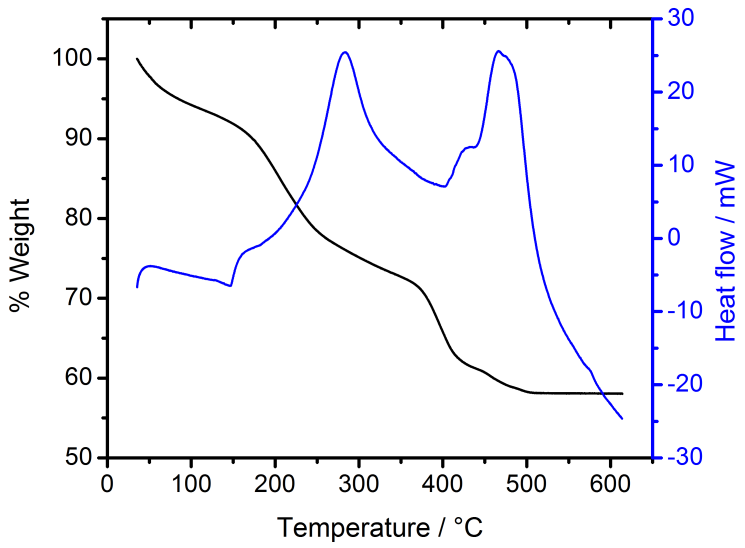


**Figure 3-4** TGA data for **$NbO_x$-Gel**, showing the weight loss and the heat flow difference when heated to 620 °C, at a rate of 0.5 °C $min^{-1}$.

The mesoporous material calcined at 450°C (**$Nb_2O_5$-450**) shows 0.3% carbon content by CHN analysis, confirming the TGA data showing that there is some organic precursor still remaining, with weight loss being evident past 450 °C. Carbon is not detected by CHN analysis in the higher temperature calcined material synthesised at 550 °C (**$Nb_2O_5$-550**), confirming the TGA data showing that the organic co-block organic polymer has decomposed and has been removed at this temperature.

Whilst the heat flow increasing at 300 °C is at the same temperature as the significant weight loss corresponding to the polymer decomposing and being removed, the peak around 500 °C is likely to be the heat of crystallization. Brayner and Bozon-Verduraz demonstrated a phase transition of niobium oxide takes place around this temperature, with amorphous $Nb_2O_5$ being crystallized to the pseudo-hexagonal form, TT-$Nb_2O_5$.[23] Material calcined at a higher temperature than this heat flow peak should therefore have a crystalline structure that could be indexed to the pseudo-hexagonal form of $Nb_2O_5$.

XRD spectra of **$Nb_2O_5$-450** and **$Nb_2O_5$-550** are shown in Figure 3-5. **$Nb_2O_5$-450**, (Figure 3-5(a)) as expected, shows a semi-amorphous structure, with broad peaks roughly corresponding to the pseudo-hexagonal phase of $Nb_2O_5$, comparable to the wide angled XRD pattern delivered by niobium based mesoporous material synthesised by Yang et al.[15] Contrary to this material however, the XRD of **$Nb_2O_5$-450** at low angle does not show any significant peaks (Figure 3-5(b)). An ordered mesoporous structure would be expect to diffract at low angles, with material synthesised by the group showing a x-ray diffraction peak at around 1.3° 2 Theta. This is not the case for both **$Nb_2O_5$-450** and **$Nb_2O_5$-550 (**Figure 3-5(d)), which signifies that any mesoporosity is not ordered. XRD of **$Nb_2O_5$-550** (Figure 3-5(c)), as expected due to the heat of crystallization peak from the TGA data of **NbOx-Gel** (Figure 3-4), shows crystalline peaks, which can be indexed to the pseudo-hexagonal phase of $Nb_2O_5$ (TT-$Nb_2O_5$).

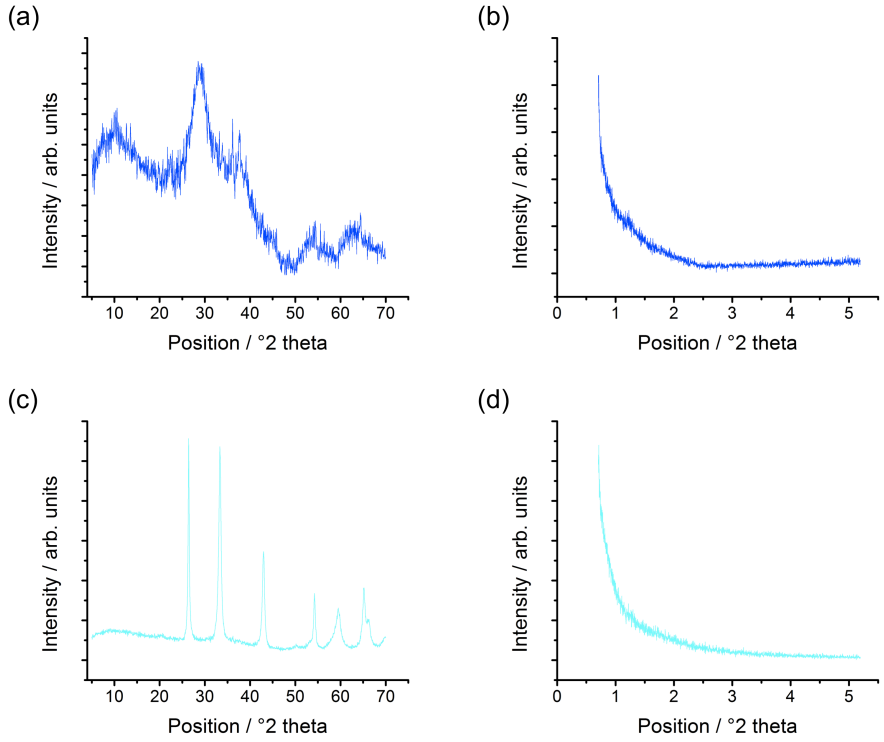


**Figure 3-5** (a) X-ray diffraction spectra of **$Nb_2O_5$-450**, showing a semi-amorphous structure, with the low angle XRD (b). (c) X-ray diffraction spectra of **$Nb_2O_5$-550**, showing a crystalline phase indexed to the pseudo-hexagonal form of $Nb_2O_5$ (TT-$Nb_2O_5$) with the low angle XRD (d).

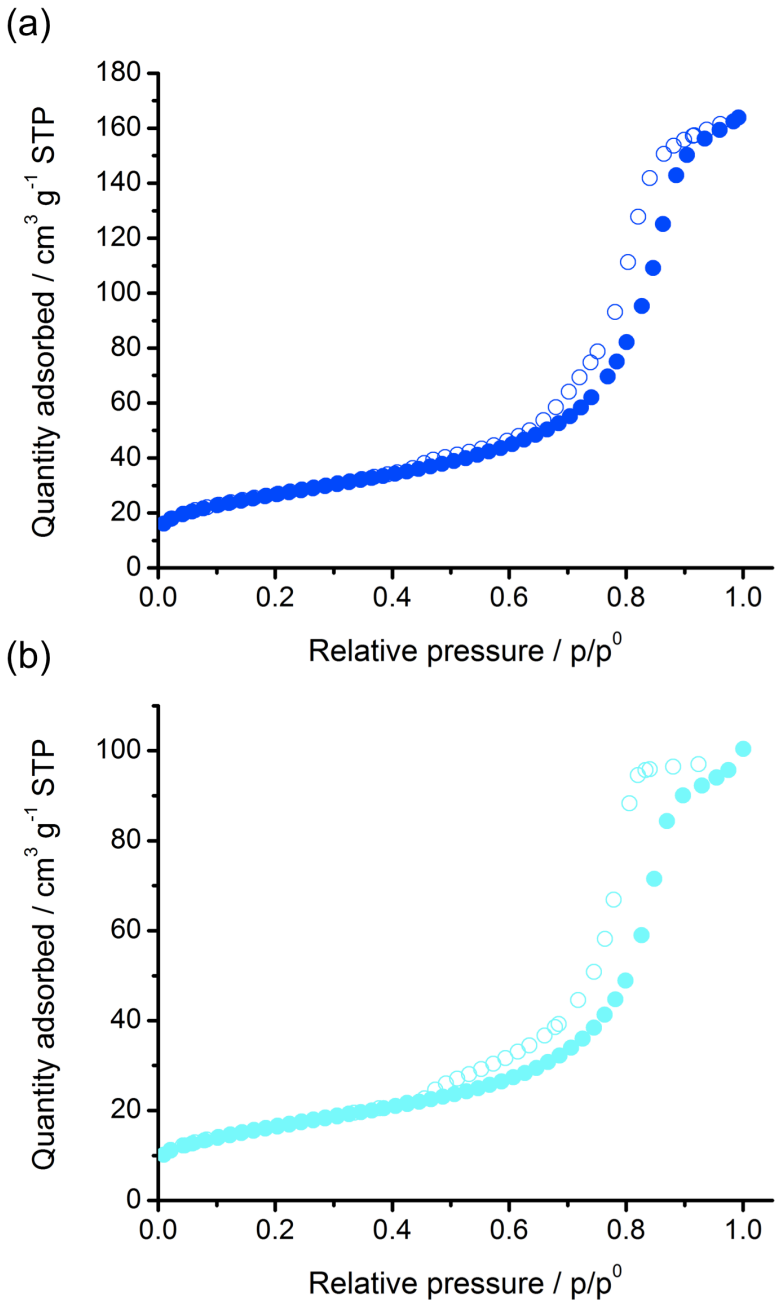


**Figure 3-6** Volumetric nitrogen absorption – desorption isotherm for **$Nb_2O_5$-450** (a) and **$Nb_2O_5$-550** (b), indicating type IV porosity: solid blue circles absorption; open blue circles desorption.

Whilst the XRD spectra disappointingly do not appear to show ordered mesoporosity in either **$Nb_2O_5$-450** or **$Nb_2O_5$-550**, nitrogen volumetric absorption / desorption isotherms show that the material does contain mesoporosity, with the shape of both isotherms Type IV, indicating a mesoporous structure.[35] The BET surface area of **$Nb_2O_5$-450** calculated

from the isotherm is 94 $m^2$ $g^{-1}$, with a pore size of around 10 nm, and significantly, a pore volume of 0.27 $cm^3$ $g^{-1}$. The BET surface area of **$Nb_2O_5$-550** shows a significant decrease compared with **$Nb_2O_5$-450**, with a BET surface area of 58 $m^2$ $g^{-1}$. In addition, with **$Nb_2O_5$-550**, the pore volume is lower at 0.15 cm $g^{-1}$ compared with the **$Nb_2O_5$-450**, despite the pore diameter remaining comparable. This is consistent with the pore structure collapsing on calcination at higher temperature, resulting in larger aggregated particles with less pore volume, and so reduced mesoporosity.

| | $Nb_2O_5$-450 | $Nb_2O_5$-550 |
|---|---|---|
| BET surface area / $m^2$ $g^{-1}$ | 94 | 58 |
| Langmuir surface area / $m^2$ $g^{-1}$ | 133 | 81 |
| Pore volume / $cm^3$ $g^{-1}$ | 0.27 | 0.16 |
| Pore size / nm | 10 | 10 |
| XRD determined particle size | - | 20 |

**Table 3-1** Table showing the BET and Langmuir determined surface area, pore volume and pore size, from volumetric nitrogen absorption – desorption isotherms carried out on **$Nb_2O_5$-450** and **$Nb_2O_5$-550**, and the XRD determined particle size of **$Nb_2O_5$-550**.

Optical measurements were carried out on **$Nb_2O_5$-450** and **$Nb_2O_5$-550** and compared to bulk $Nb_2O_5$ supplied by Alfa-Aesar (**$Nb_2O_5$-bulk**). The diffuse reflectance of the 3 materials was determined by firstly measuring the % reflectance from 190 nm – 900 nm, and then converting to Kubelka-Munk units [F(R)], as described in Chapter 2. As explained, plotting the Kubelka-Munk function multiplied by energy to the power of 2, ($[F(R)xE]^2$) vs energy (*E*, which can be calculated from the wavelength of light), will result in a linear plot at energies above the energy of the band gap. This linear section can

be extrapolated, with the intercept on the x-axis equal to the direct band gap of the material. For $Nb_2O_5$, with niobium in the +5 oxidation state, there are no *d* electrons, and so *d* – *d* transitions will not be expected in the absorbance spectrum. The only transitions evident will be transitions between the oxygen O2*p* orbitals, constituting the valence band, being excited to the conduction band, consisting of niobium 4*d* orbitals. The wavelength or energy at which these transitions occur will therefore be the band gap of $Nb_2O_5$, signified by an increase in the absorbance, represented by the Kubelka-Munk function, F(R), in the diffuse reflectance.

Wang and Herron studied the effect of particle size on semiconductors, noting an increase in band gap as the particle size decreases, described as the Quantum Confinement Effect.[36] They attributed this to the idea that as the bulk size of the particle decreases, and so the number of atoms decreases, the energy bands of the semiconductor become more discrete, allowing greater separation between the bands, and so an increase in the energy separating the band i.e. the band gap. The direct band gap of **$Nb_2O_5$-450** is larger than the direct band gap of **$Nb_2O_5$-550**, implying an increase in particle size as the calcination temperature increases. This is expected, as the higher calcination temperature causes the particles to sinter more, implying larger particles. The Quantum Confinement Effect becomes less relevant as the particle size increases; the band gap of **$Nb_2O_5$-550** is comparable with **$Nb_2O_5$-bulk**. XRD determines the particle size of **$Nb_2O_5$-550** to be 20 nm; whereas with a surface area of 1.8 $m^2$ $g^{-1}$, **$Nb_2O_5$-bulk** has a particle size of around 700 nm, significantly higher than that of **$Nb_2O_5$-550**.

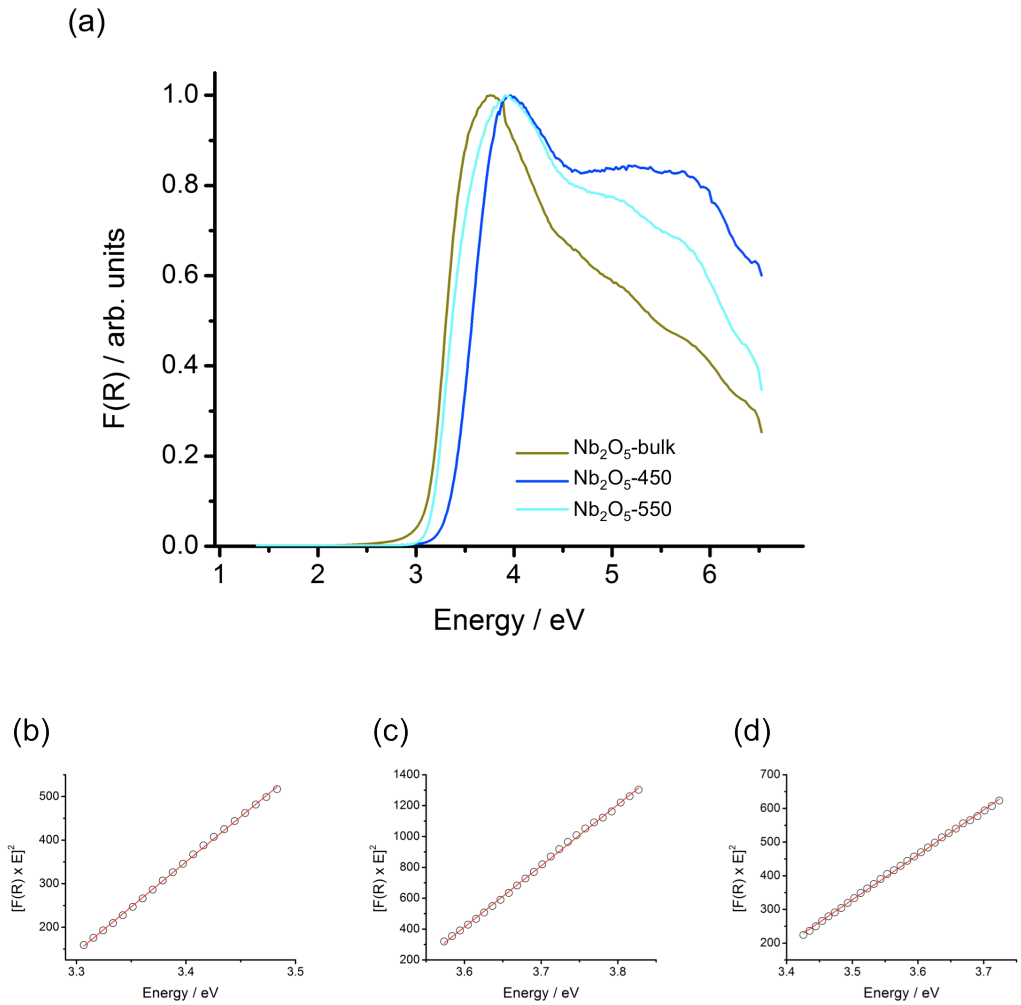


**Figure 3-7** (a) Diffuse reflectance of **$Nb_2O_5$-450** and **$Nb_2O_5$-bulk**, supplied by Alfa-Aesar. The extrapolation of the linear section of the diffuse reflectance of **$Nb_2O_5$-bulk** (b), **$Nb_2O_5$-450** (c) and **$Nb_2O_5$-550** (d), plotted to determine the direct band gap, with the intercept of the x axis (the direct band gap) at 3.23 eV for **$Nb_2O_5$-bulk**, 3.49 eV for **$Nb_2O_5$-450** and 3.26 eV for **$Nb_2O_5$-550**.

Despite the lack of order of mesoporosity evidenced by the absence of a low angle diffraction peak, the nitrogen absorption / desorption isotherm confirms that the **$Nb_2O_5$-450** material is mesoporous, with a pore volume of 0.27 $cm^3$ $g^{-1}$, which is significant for impregnation techniques planned to be developed in the project for adding platinum group metals and metal oxides.

## 3.3 Nanoparticulate $Nb_2O_5$

A comparatively simpler route than the sol-gel based synthesis described for synthesising mesoporous $Nb_2O_5$ was also carried out, as a comparison to the mesoporous material. Uekawa et al synthesised $Nb_2O_5$ based on a precipitate route where niobium (V) chloride ($NbCl_5$) is hydrolyzed to form $Nb_2O_5$ precipitate material.[34] Material synthesised in this way was used successfully by Alsalme et al. as support for their Keggin Heteropoly Acid catalysts, used in esterification and transesterification reactions.[37] In the $Nb_2O_5$ synthesis by Uekawa et al., $NbCl_5$ is hydrolyzed by adding a solution of $NbCl_5$ dissolved in ethanol, to a basic solution of ammonia, precipitating out the $Nb_2O_5$ material. This is then filtered and washed to remove the ammonia and chloride ions, before being dried in an oven overnight.

### 3.3.1 Synthesis of Nanoparticulate $Nb_2O_5$

The nanoparticulate $Nb_2O_5$ precipitate material was synthesised by firstly dissolving 5 g (0.02 M) of $NbCl_5$ into 10 ml of anhydrous ethanol (EtOH), generating a clear, yellow green tinged 2 M solution of $NbCl_5$. This was added drop wise by pipette to 200 ml of a previously prepared 0.3 M ammonia ($NH_3$) solution over the course of 20 minutes, under vigorous stirring. White precipitate was formed on contact of the $NbCl_5$ solution with the $NH_3$ solution. On completion of the addition of $NbCl_5$, the suspension was allowed to stir for a further hour, before the material was filtered using a Buchner Flask under vacuum. This precipitated material was continually washed with deionized water, with the washings tested with silver nitrate solution for chloride content. When there was no evidence of chloride, the precipitated material was removed from the filter, and dried overnight in an oven at 105 °C. The material (**$Nb_2O_5$-Nano**) was then ground into a fine white powder.

## 3.3.2 Characterisation of Nanoparticulate $Nb_2O_5$

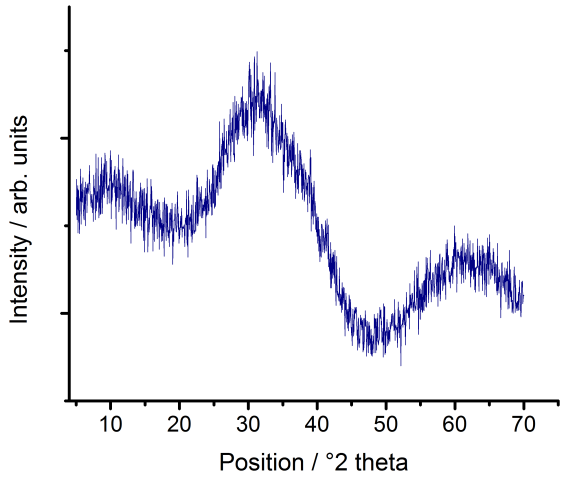


**Figure 3-8** X-ray diffraction spectra of **$Nb_2O_5$-nano**, showing a semi-amorphous structure.

XRD of **$Nb_2O_5$-Nano** showed a semi-amorphous structure with broad peaks roughly corresponding to the pseudo hexagonal phase of $Nb_2O_5$, comparable with the mesoporous material (**$Nb_2O_5$-450**) synthesised using the method by Yang et al.[15] This XRD is consistent with the material synthesised by both Uekawa et al and Alsalme et al.[34, 37] The BET surface area of this material was determined to be 214 $m^2$ $g^{-1}$, over twice that of **$Nb_2O_5$-450**. As described in Chapter 2, the particle size can be calculated from the surface area from non porous material, by assuming the particles are spheres, and using the bulk density of $Nb_2O_5$ as the density. The particle size of the material calculated this way from the surface area, is 6 nm; significantly smaller than the particle size determined from the XRD of **$Nb_2O_5$-550**.

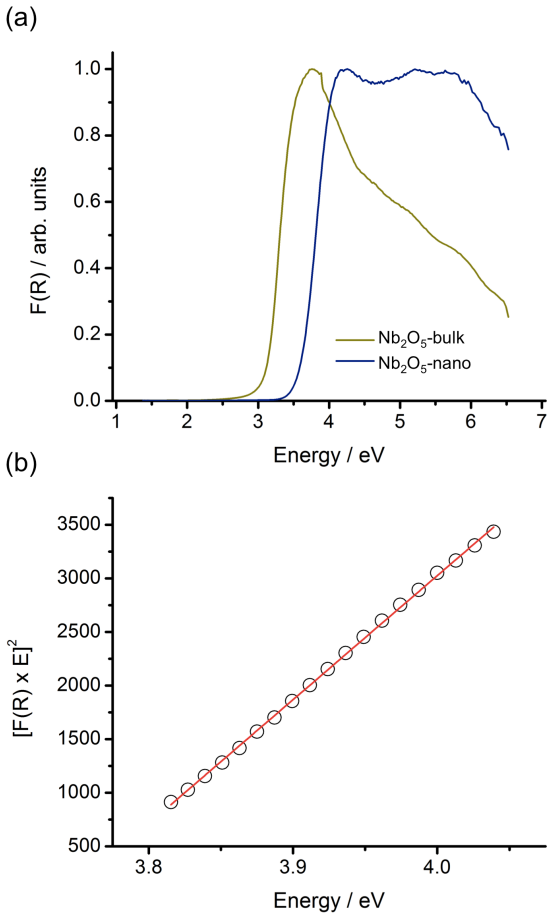


**Figure 3-9** (a) Diffuse reflectance of **$Nb_2O_5$-nano** and **$Nb_2O_5$-bulk**. (b) The extrapolation of the linear section of the diffuse reflectance of **$Nb_2O_5$-nano** plotted to determine the direct band gap, with the intercept of the x axis (the direct band gap) at 3.74 eV.

The small particle size is also indicative in the diffuse reflectance; in a comparable way to **$Nb_2O_5$-450** and **$Nb_2O_5$-550**, the direct band gap can be calculated from the extrapolation of $[F(R)xE]^2$ vs energy (Figure 3-9). The direct band gap calculated for **$Nb_2O_5$-Nano** is 3.74 eV, significantly larger than **$Nb_2O_5$-bulk**, calculated to 3.23 eV, and also larger than 3.49 eV for **$Nb_2O_5$-450** and 3.25 for **$Nb_2O_5$-550**. The reason for this shift is due to the Quantum Confinement Effect, with the very small particle size of **$Nb_2O_5$-Nano** (6 nm) responsible for such the large shift in direct band gap when compared in particular with **$Nb_2O_5$-bulk**, with a particle size determined to be 700 nm by a comparable method.

## 3.4 Methyl Orange Degradation with Nano and Meso $Nb_2O_5$

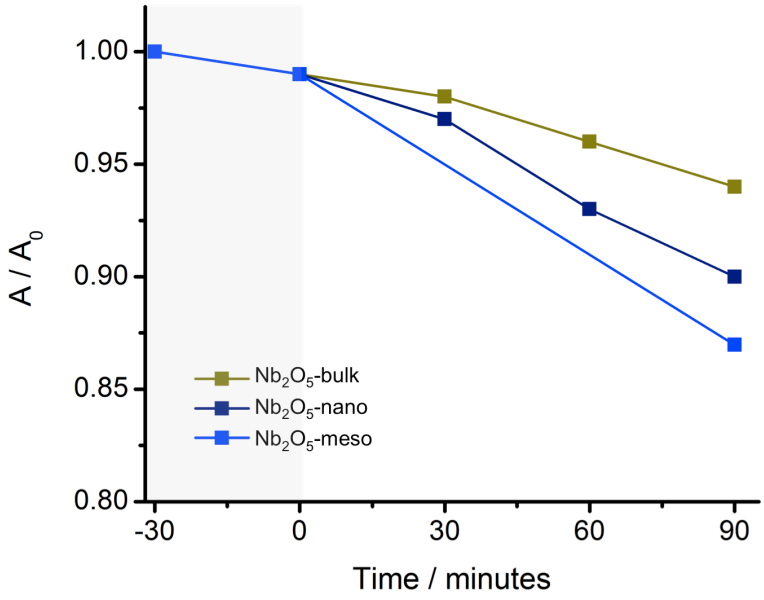


**Figure 3-10** The change in concentration of methyl orange over the course of 90 minutes of a UV light reaction with **$Nb_2O_5$-bulk**, **$Nb_2O_5$-450** and **$Nb_2O_5$-nano**.

In order to test the photocatalytic properties of nanoparticulate and mesoporous $Nb_2O_5$ synthesised, the material was reacted with the model azo dye methyl orange. As explained in Chapter 2, methyl orange is stable under near UV and visible light, due to the molecule undergoing rapid trans – cis photo-isomerization, powered by the energy absorbed from light..[38] By reacting the synthesised material under UV light with methyl orange, a decrease in concentration will be due to the excited holes and electrons from the $Nb_2O_5$ degrading the methyl orange. For comparison, **$Nb_2O_5$-bulk** used for the optical comparisons was also tested.

In all cases, 1 g $L^{-1}$ of catalyst was reacted with 6.11 x $10^{-5}$ M methyl orange under UV light (300 W Xe lamp) for 90 minutes using the experimental set up and measurement

protocol described in Chapter 2. As expected due to the higher surface area and porosity of **$Nb_2O_5$-450** and higher surface area of **$Nb_2O_5$-nano**, both degraded significantly more Methyl orange over the course of the reaction than the **$Nb_2O_5$-bulk**. This is despite the larger direct band gap of **$Nb_2O_5$-450** and **$Nb_2O_5$-nano**, which implies a lower total amount of light can be absorbed with this higher band gap material when compared to the **$Nb_2O_5$-bulk**. The higher amount of methyl orange degraded is also significant, when comparing the crystallinity; the highly crystalline **$Nb_2O_5$-bulk** degrades less than the semi-amorphous **$Nb_2O_5$-nano** and **$Nb_2O_5$-450**. It is clear that the surface area is a key factor, with the surface area of **$Nb_2O_5$-nano** and **$Nb_2O_5$-450** significantly higher than **$Nb_2O_5$-bulk**, determined to be 1.8 $m^2$ $g^{-1}$. However despite **$Nb_2O_5$-nano** having more than twice the surface area of **$Nb_2O_5$-450**, **$Nb_2O_5$-nano** degrades less methyl orange than **$Nb_2O_5$-450**, implying factors other than surface area determine the photocatalytic activity of the material in terms of methyl orange degradation.

## 3.5 Scaled Up Nanoparticulate $Nb_2O_5$

Both the mesoporous and nanoparticulate $Nb_2O_5$ material are clearly good photocatalysts, able to degrade methyl orange without any further modification. The high surface area makes them ideal candidates for loading with platinum group metals (PGM) or metal oxides. In order to further characterise the material, it would be extremely desirable to synthesise the material on a larger scale. As the ultimate aim is to use this material in PGM addition work, where a number of different PGMs can be used, with various percentage loadings of the metal, in addition to modification of material with the aim of promoting visible light catalysis, synthesising 100 – 200 g quantities would be ideal. The precipitation route offers a somewhat simple way of scaling up, by merely using a larger quantity of starting reagents and larger containers.

### 3.5.1 Synthesis of Scaled Up Nanoparticulate $Nb_2O_5$-1

Initially, the synthesis of **$Nb_2O_5$-nano** was scaled up by a factor of 10, and so the starting reagents $NbCl_5$, EtOH and $NH_3$ were all increased in terms of amount of starting material used, with the actual concentrations of the solutions involved remaining consistent.

50 g (0.2 mol) of $NbCl_5$ were added slowly into 100 ml of anhydrous EtOH, generating a clear yellow/green 2 M solution of $NbCl_5$. This solution was added drop wise from a separation funnel into 2 L of a previously prepared 0.3 M solution of $NH_3$ under vigorous stirring, over the course of 1 hour. White precipitate was formed on contact of the $NbCl_5$ solution with the $NH_3$ solution. On completion the suspension was allowed to stir for a further hour, before the precipitated material was collected by filtration under vacuum. The precipitate was continually washed with deionized water at a temperature of 60 °C. This continued until the washings collected showed conductivity of less than 50 μS, as measured with a conductivity meter. This material was then further washed with 2 L of 60 °C deionized water, and collected and dried overnight in an oven at 105 °C. The material was finally ground into a fine white powder (**$Nb_2O_5$-1**).

### 3.5.2 Further modification of the synthesis

The precipitation route, whilst quite straightforward, does have a number of variables that could affect the nanoparticulate product. For example, the concentration of the starting $NbCl_5$ solution, or the $NH_3$ solution could affect the way the material is precipitated. The temperature at which the reaction takes place at could also have some impact on the precipitated material.

Although the synthesis of **$Nb_2O_5$-1** followed the synthesis reported by Uekawa et al,[34] in particular using the same concentrations of starting materials reported by the group, it can be seen that the concentration of ammonia the group used in the reported synthesis was not concentrated enough to ensure the entire precipitation was carried out under basic

conditions. The 0.2 M $NH_3$ solution would neutralize some of the HCl produced in the precipitation synthesis, but not all, implying that some of the **$Nb_2O_5$-1** product would be synthesised under acidic conditions. By increasing the concentration of $NH_3$ from 0.3 M to 0.55 M, whilst maintaining the concentration of $NbCl_5$, a 20% excess of ammonia will be present compared to the amount of HCl that will be generated on addition of the $NbCl_5$ / ethanol solution, leading to basic conditions throughout the reaction.

A peristaltic pump, used to add the $NbCl_5$ solution to the $NH_3$ solution, might also be advantageous compared with the system used to synthesis **$Nb_2O_5$-1**, where the $NbCl_5$ solution is added drop-wise. By using the peristaltic pump, the $NbCl_5$ solution can be pumped directly into the $NH_3$ solution as opposed to deposited on the surface. Another advantage of using a peristaltic pump is that an actual rate of addition can be calculated more accurately, with the solution pumped consistently ensuring better reproducibility.

In addition to the synthesis of **$Nb_2O_5$-1** therefore, a further 5 synthetic procedures were carried out, yielding 5 further $Nb_2O_5$ precipitates, labeled **$Nb_2O_5$-2** – **$Nb_2O_5$-6**. The synthesis conditions are summarized in **Table 3-2**, in addition to data for initial characterisation of the synthesised material: the surface area, particle size determined from the surface area, and the direct band gap of the material.

The surface area in particular demonstrates that the synthesis method employed produces a significant difference in particles, with surface areas ranging from 148 – 334 $m^2\ g^{-1}$. The direct band gap also varies with the synthesis conditions, with higher band gaps corresponding to smaller particles as calculated from surface area, as expected from the Quantum Confinement Effect.

| Exp | $NbCl_5$ / EtOH | $NH_3$ Conc / M | Temp | Dropper / Pump | EtOH to Base | Surface area / $m^2\ g^{-1}$ | Particle size from SA / nm | Direct Band Gap / eV |
|---|---|---|---|---|---|---|---|---|
| 1 | 50 g / 100 ml | 0.3 | RT | Dropper | Yes | 264 | 4.9 | 3.77 |
| 2 | 50 g / 100 ml | 0.55 | RT | Dropper | Yes | 148 | 8.8 | 3.72 |
| 3 | 50 g / 400 ml | 0.55 | RT | Pump | Yes | 299 | 4.4 | 3.84 |
| 4 | 50 g / 100 ml | 0.55 | RT | Pump | Yes | 159 | 8.2 | 3.77 |
| 5 | 50 g / 400 ml | 0.55 | 60 °C | Pump | Yes | 332 | 3.9 | 3.86 |
| 6 | 50 g / 400 ml | 0.55 | RT | Pump | No | 334 | 3.9 | 3.89 |

**Table 3-2** Table showing the synthetic conditions for synthesising nanoparticulate **$Nb_2O_5$-1** to **$Nb_2O_5$-6**, with initial characterisation: surface area, particle size determined from surface area and the direct band gap.

From these initial results, it is clear that the synthetic route producing **$Nb_2O_5$-3**, **$Nb_2O_5$-5** and **$Nb_2O_5$-6** provide material with the highest surface area and smallest particle size. Significantly, these three synthetic routes use the same concentration of $NbCl_5$: 50 g $NbCl_5$ in 400ml of EtOH, leading to a 0.5 M $NbCl_5$ solution. Higher concentrated 2 M $NbCl_5$ solution procedures (50 g $NbCl_5$ in 100ml of EtOH) producing **$Nb_2O_5$-2** and **$Nb_2O_5$-4**, generate significantly larger particles, with material synthesised this way having less than half the surface area of the lower concentration of $NbCl_5$ material although this is not the case for the original synthetic route producing **$Nb_2O_5$-1**, which uses a 2 M $NbCl_5$ solution. In terms of surface area, higher temperature or adding base to $NbCl_5$ has negligible effect, with the surface areas of **$Nb_2O_5$-5** and **$Nb_2O_5$-6** comparable to **$Nb_2O_5$-3**. Increasing the concentration of $NH_3$ does have an effect on the surface area, noted by comparing **$Nb_2O_5$-1** with **$Nb_2O_5$-2**, with a significant decrease in surface area when increasing the concentration of $NH_3$. However decreasing the concentration of the $NbCl_5$ solution

seemingly mitigates that, with an increase in surface area visible when comparing the low $NH_3$ concentration / high $NbCl_5$ concentration route **$Nb_2O_5$-1** with the higher concentration $NH_3$ route / low $NbCl_5$ concentration route forming **$Nb_2O_5$-3**. An explanation for this could be that in cases where the reagents are concentrated when precipitating out (either from the $NH_3$ or $NbCl_5$ solution), the close proximity of the reagents in solution determined by the high concentration, means the precipitate material aggregates on precipitation, producing larger particles. In low concentration solutions, the proximity of the reagents in solution is less, and so there is less aggregation of the material on precipitation, leading to smaller particle size and higher surface area.

From these initial results therefore, it can be concluded that basic conditions using a concentration of 50 g / 400 ml $NbCl_5$ (0.5 M) would be the ideal reaction to produce high surface area / small particle size precipitate $Nb_2O_5$. Carrying the synthesis out at a higher temperature, or adding base to $NbCl_5$ does not have a significant impact on the surface area of the nanoparticles produced, therefore performing the reaction at room temperature would give satisfactory particles; using a peristaltic pump is preferable in terms of reaction set up and ease of use, and has no significant impact on the particles compared to the dropper system employed for the smaller scale synthesis.

### 3.5.3 Characterisation of $Nb_2O_5$-1 and $Nb_2O_5$-3

In addition to the BET surface area, calculated to be 264 $m^2 g^{-1}$, **$Nb_2O_5$-1** was characterised by TGA and XRD (Figure 3-11). XRD showed a semi-amorphous structure with broad peaks, roughly corresponding to the pseudo-hexagonal phase of $Nb_2O_5$, and comparable to previously synthesised mesoporous **$Nb_2O_5$-450**, nanoparticulate **$Nb_2O_5$-nano** (Section 3.2, 3.3), and material synthesised by Uekawa et al,[34] and Alsalme et al.[37]

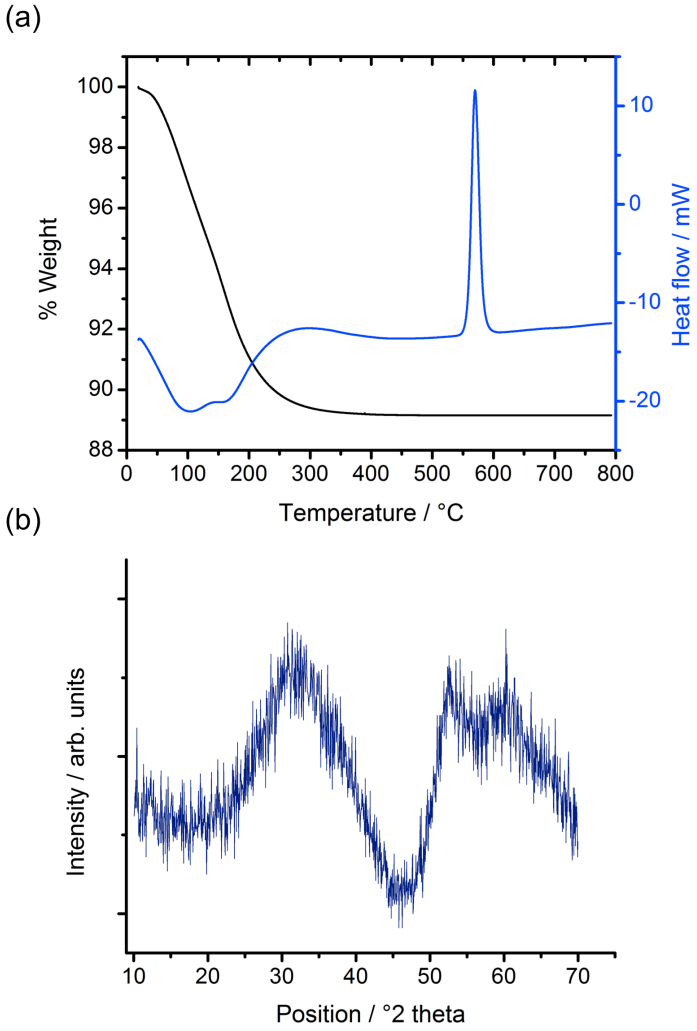


**Figure 3-11** (a) TGA data for **$Nb_2O_5$-1** showing the weight loss and the heat flow difference when heated to 800 °C. (b) X-ray diffraction pattern of **$Nb_2O_5$-1**, showing a semi-amorphous structure.

The TGA showed a significant weight loss of nearly 11%, up to a temperature of around 350 °C. CHN analysis of **$Nb_2O_5$-1** showed total hydrogen content of 1.245%, and nitrogen content of 0.906%. The significant nitrogen content must come from the starting reagents used to synthesise **$Nb_2O_5$-1**, implying there is some ammonia still present in the material from the synthesis, despite the continuous washing. Chlorine analysis confirmed there was negligible chlorine present, with less than 20 ppm of chlorine detected, indicating the washing procedure to remove chloride was successful.

As seen with the TGA of the **$NbO_x$-gel** (Figure 3-4) the precursor for **$Nb_2O_5$-450** and **$Nb_2O_5$-550**, a heat of crystalisation peak is evident. In this case, the actual heat flow increase is sharper, and occurs at a higher temperature (580 °C) than the mesoporous material which occurs at around 530 °C, but is consistent with the behavior of $Nb_2O_5$ nanoparticles on calcination.[23] From the TGA weight loss, and the CHN data, an actual formula for this precipitate material can be calculated: **$Nb_2O_5(H_2O)_{1.5}(NH_3)_{0.2}$**. The TGA data suggests that calcining at a temperature higher than 350°C will remove the ammonia content and the excess water, which may be present as hydroxide. Calcining at a temperature higher than 580 °C should also produce crystalline material, comparable to the mesoporous **$Nb_2O_5$-550**, which was indexed to the pseudo-hexagonal phase of $Nb_2O_5$ (TT-$Nb_2O_5$).

**$Nb_2O_5$-3** was characterised in a comparable way; with the BET surface area of the material calculated to be 299 $m^2$ $g^{-1}$. XRD and TGA data are comparable with **$Nb_2O_5$-1**, however the TGA indicates there is significantly more weight loss on heating with **$Nb_2O_5$-3**, although the weight loss (over 20%) is complete at a comparable temperature as **$Nb_2O_5$-1** at 350 °C. With a smaller particle size and higher surface area than **$Nb_2O_5$-1**, **$Nb_2O_5$-3** will be expected to adsorb a larger quantity of moisture and ammonia onto the surface of the particles, hence a greater amount of $H_2O$ and $NH_3$ content would be expected. The chlorine content for the material was determined to be below 20 ppm, indicating removing the chloride content by washing was again successful. From the TGA data, calcining at a temperature above 350 °C should remove the ammonia and the excess water / hydroxide; calcining above 580 °C should produce crystalline $Nb_2O_5$.

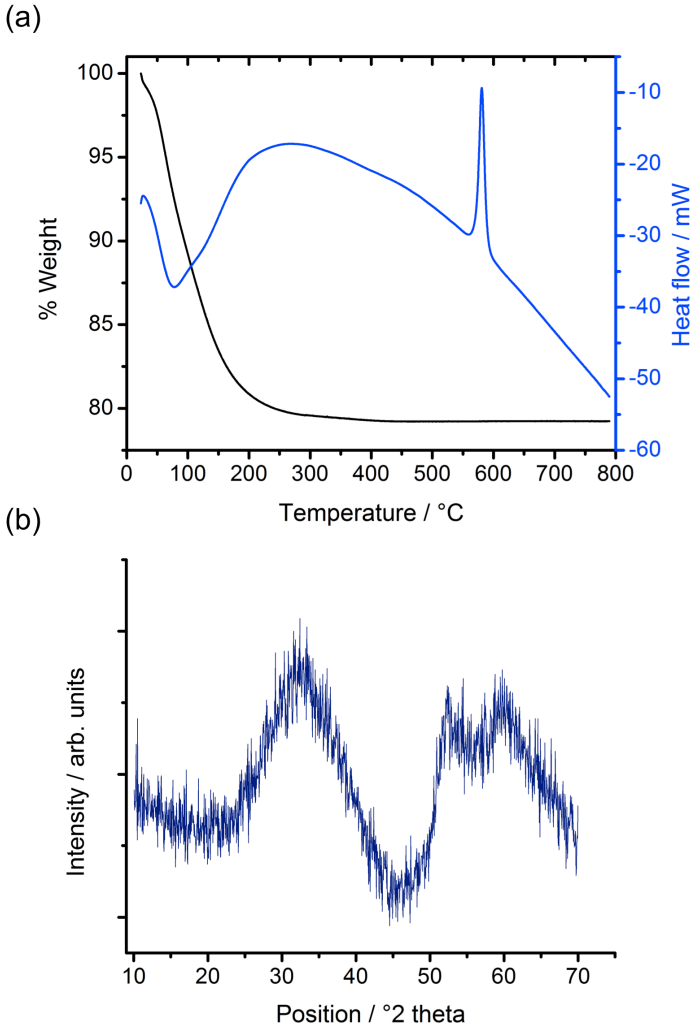


**Figure 3-12** (a) TGA data for **$Nb_2O_5$-3** showing the weight loss and the heat flow difference when heated to 800 °C. (b) X-ray diffraction pattern of **$Nb_2O_5$-3**, showing a semi-amorphous structure.

## 3.5.4 Calcining $Nb_2O_5$-1 and $Nb_2O_5$-3

Based on the TGA results indicating non $Nb_2O_5$ material was present in the precipitated materials **$Nb_2O_5$-1** and **$Nb_2O_5$-3**, this material was calcined at temperatures of either 350 °C, 500 °C or 600 °C for 2 hours, in all cases heating the material from room temperature to the assigned temperature at 5 °C $min^{-1}$ and cooling at 10 °C $min^{-1}$.

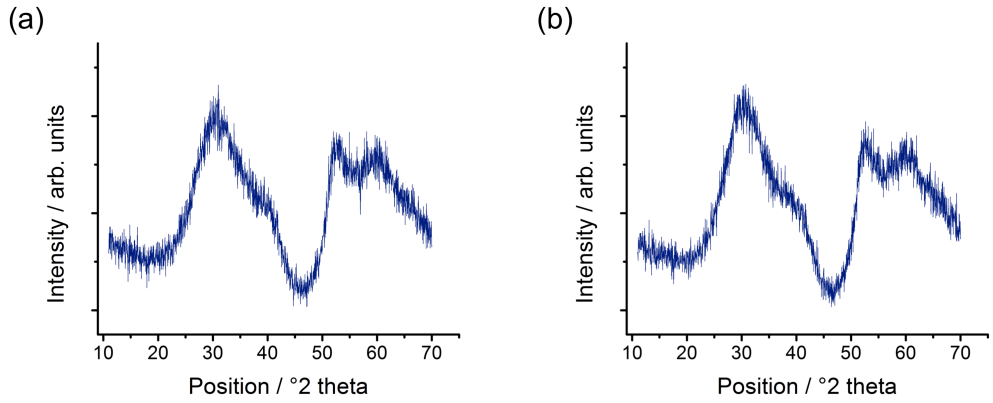


**Figure 3-13** X-ray diffraction spectra of (a) **$Nb_2O_5$-1:350** and (b) **$Nb_2O_5$-1:500**, showing a semi-amorphous structure.

The XRD spectra of **$Nb_2O_5$-1** material calcined at 350 °C (**$Nb_2O_5$-1:350**), and 500 °C (**$Nb_2O_5$-1:500**) is shown (Figure 3-13). Material again shows a semi-amorphous structure, comparable with the initial precipitate material **$Nb_2O_5$-1** and with the mesoporous **$Nb_2O_5$-450**. The BET surface area for this material decreases from 264 $m^2$ $g^{-1}$ to 206 $m^2$ $g^{-1}$ for **$Nb_2O_5$-1:350**), and to 170 $m^2$ $g^{-1}$ for material calcined at 500 °C **$Nb_2O_5$-1:500**. CHN analysis of both of these materials confirms there is no nitrogen present, signifying that the calcination has removed the ammonia; TGA of calcined material shows weight loss of between 4% and 2.5%, consistent with CHN data indicating some water adsorbed onto the surface of the nanoparticles.

TEM images of material before and after calcination provide a qualitative method of inspecting the material. From the images, the **$Nb_2O_5$-1:500**, calcined at a temperature of 500 °C, show more defined particles than the material pre calcination **$Nb_2O_5$-1**. This could be due to the decrease in non-niobium oxide material present in **$Nb_2O_5$-1:500**. Although the XRD spectra does not show significant differences between **$Nb_2O_5$-1** and **$Nb_2O_5$-1:500**, the TEM images do suggest qualitatively that **$Nb_2O_5$-1:500** is more crystalline.

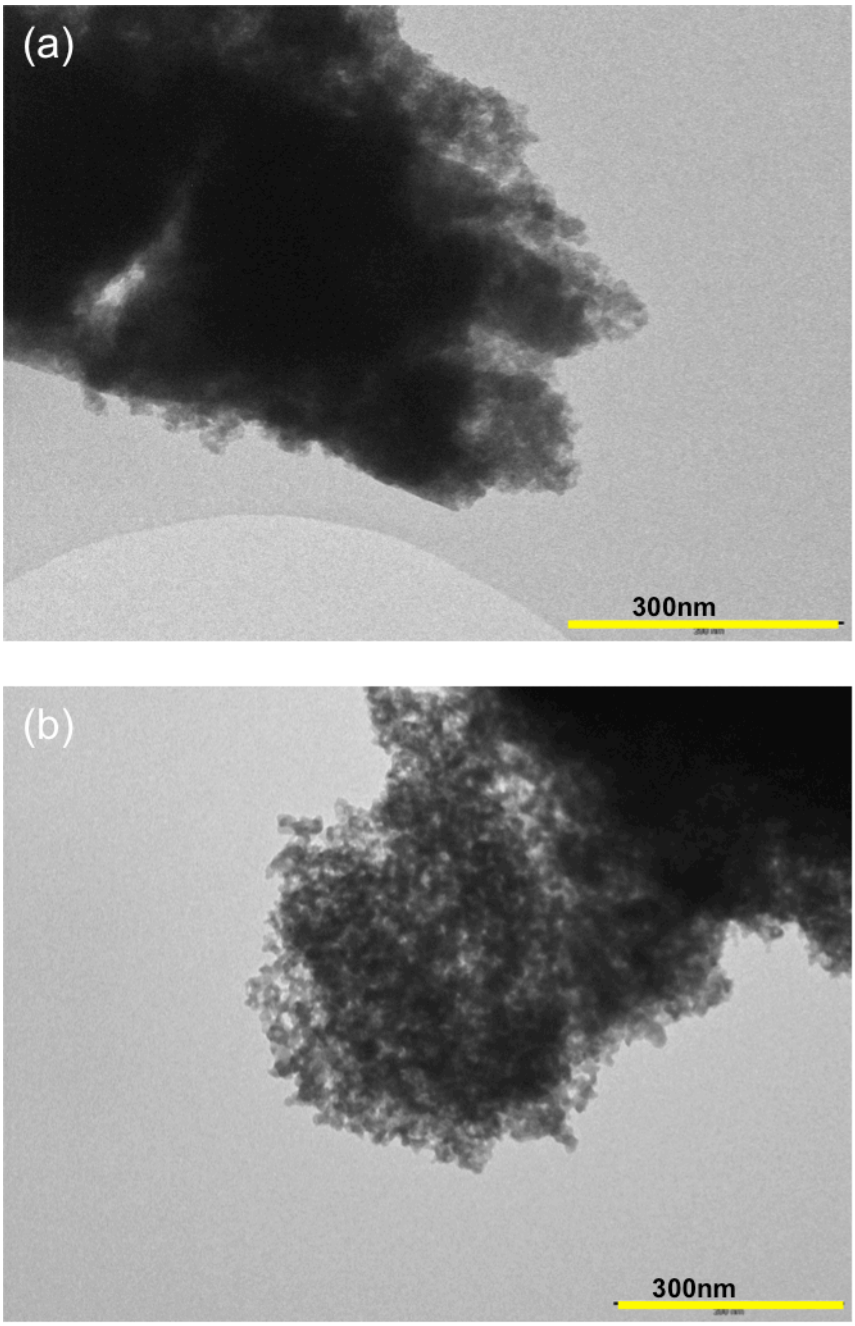


**Figure 3-14** Transmission elctron microscopy (TEM) images of (a) **$Nb_2O_5$-1** and (b) **$Nb_2O_5$-1:500**.

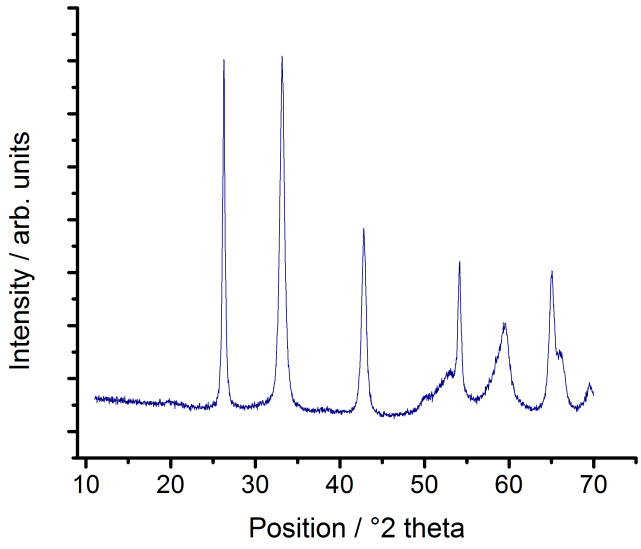


**Figure 3-15** X-ray diffraction spectra of **$Nb_2O_5$-1:600**, showing a crystalline phase that can be indexed to the pseudo-hexagonal form of $Nb_2O_5$ (TT-$Nb_2O_5$).

XRD of **$Nb_2O_5$-1:600,** material calcined at 600°C, shows crystalline peaks, which can be indexed to the pseudo-hexagonal phase of $Nb_2O_5$. The surface area of this material is 57 $m^2$ $g^{-1}$, comparable to the crystalline mesoporous **$Nb_2O_5$-550** (58 $m^2$ $g^{-1}$). The particle size, calculated from the XRD spectra using the Scherrer Equation, is 14 nm, comparable with that calculated from surface area (23 nm).

As would be expected due to the Quantum Confinement Effect, the direct band gap of $Nb_2O_5$ material decreases, from the small particle **$Nb_2O_5$-1** through to the larger particle **$Nb_2O_5$-1:600**. By plotting $[F(R)xE]^2$ vs E, the direct band gap can be calculated from the extrapolation of the linear section of the plot; this gives the direct band gap as **$Nb_2O_5$:350**, 3.62 eV; **$Nb_2O_5$:500**, 3.63 eV; **$Nb_2O_5$:600**, 3.47 eV). The diffuse reflectance of the material is shown in Figure 3-16, illustrating the decreasing band gap with increasing particle size.

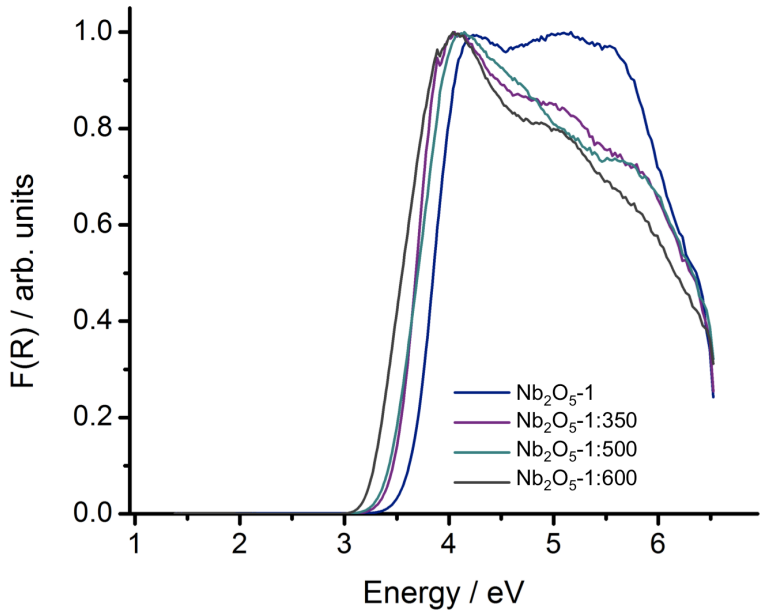


**Figure 3-16** Difuse reflectance of **$Nb_2O_5$-1**, **$Nb_2O_5$-1:350**, **$Nb_2O_5$-1:500** and **$Nb_2O_5$-1:600**.

To test the photocatalytic properties of the material, **$Nb_2O_5$-1**, **$Nb_2O_5$-1:350, $Nb_2O_5$-1:500** and **$Nb_2O_5$-1:600** were reacted with the model dye methyl orange. As with the reactions with the lower scale material (**$Nb_2O_5$-450** and **$Nb_2O_5$-nano**), the degradations were carried out with 1 g $L^{-1}$ of catalyst, reacted with 6.11 x $10^{-5}$ M methyl orange under UV light (300 W Xe lamp) using the experimental set up and measurements described in Chapter 2 (Figure 3-17). Despite the lower surface area, the methyl orange degradation effectiveness of the material improved on calcination. Whereas **$Nb_2O_5$-1** degraded 5% of the methyl orange solution in 1 hour, **$Nb_2O_5$-1:350** and **$Nb_2O_5$-1:500** degraded around 10% per hour. This could be due to the lack of ineffective water / hydroxide / ammonia content in the calcined material compared to the as made **$Nb_2O_5$-1**, that could have a detrimental effect on the degradation. Alternatively, the more crystalline in appearance **$Nb_2O_5$-1:500** may degrade methyl orange more effectively.

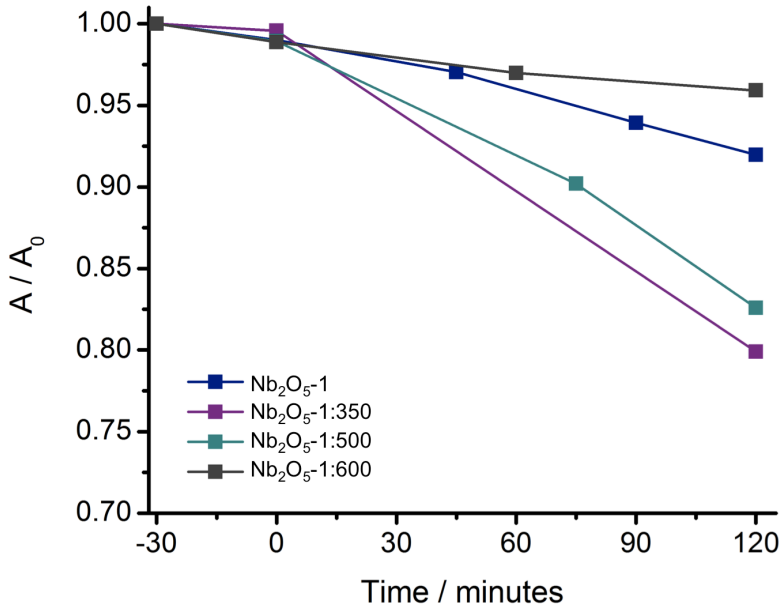


**Figure 3-17** The change in concentration of methyl orange over the course of 2 hours of a UV light reaction with **$Nb_2O_5$-1**, **$Nb_2O_5$-1:350**, **$Nb_2O_5$-1:500** and **$Nb_2O_5$-1:600**.

| Sample | Surface area / $m^2$ $g^{-1}$ | MO degradation % / hour | % MO degraded per unit surface area / % $h^{-1}$ $m^{-2}$ |
|---|---|---|---|
| $Nb_2O_5$-1 | 264 | 5 | 0.0189 |
| $Nb_2O_5$-1:350 | 206 | 10 | 0.0485 |
| $Nb_2O_5$-1:500 | 170 | 9 | 0.0529 |
| $Nb_2O_5$-1:600 | 57 | 2 | 0.0351 |

**Table 3-3** Methyl orange degradation data for **$Nb_2O_5$-1**, **$Nb_2O_5$-1:350**, **$Nb_2O_5$-1:500** and **$Nb_2O_5$-1:600**, comparing the % methyl orange degraded per unit surface area.

Normalizing to unit of surface area illustrates the quality of the $Nb_2O_5$ being used to degrade the methyl orange, with **$Nb_2O_5$-1:500** showing the maximum degradation per unit surface area, significantly higher than **$Nb_2O_5$-1** (Table 3.3)

The calcination products of **$Nb_2O_5$-3**: **$Nb_2O_5$-3:350** calcined at 350 °C, **$Nb_2O_5$-3: 500** calcined at and **$Nb_2O_5$-3:600** calcined at 600 °C were similarly characterised for surface

area, optical properties and photocatalytic properties with respect to methyl orange degradation, showing comparable results compared to the calcined material based on **$Nb_2O_5$-1**.

A summary of the characterisation of **$Nb_2O_5$-1** and the calcination products, along with **$Nb_2O_5$-1** and the material calcined from this is illustrated in Table 3-4.

| Sample | Calcination temp / °C | Surface area / $m^2$ $g^{-1}$ | Direct band gap / eV | MO degradation % / hour | Cl content / ppm | TGA weight loss / % | CHN |
|---|---|---|---|---|---|---|---|
| $Nb_2O_5$-1 | - | 264 | 3.77 | 5 | < 20 | 14 | C - / H 1.416 / N 0.791 |
| | 350 | 206 | 3.62 | 10 | | 4 | |
| | 500 | 170 | 3.63 | 9 | | 2.5 | C - / H 0.412 / N - |
| | 600 | 57 | 3.47 | 2 | | 1.5 | |
| $Nb_2O_5$-3 | - | 299 | 3.84 | 5 | < 20 | 21 | C - / H 1.570 / N 0.926 |
| | 350 | 224 | 3.61 | 7 | | 3 | |
| | 500 | 151 | 3.61 | 8 | | 3 | C - / H 0.55 / N - |
| | 600 | 61 | 3.49 | 3 | | 2.5 | |

**Table 3-4** Summary of the characterisation of **$Nb_2O_5$-1** and the calcination products from this, along with characterisation of **$Nb_2O_5$-3** and the material calcined from this.

The improvement of the $Nb_2O_5$ on calcination at 350 °C and 500 °C with respect to methyl orange degradation signifies that the calcined material is a superior photocatalyst to the as-made precipitated material, with the % methyl orange degraded per unit surface area superior for the material calcined at 500 °C, using both **$Nb_2O_5$-1** and **$Nb_2O_5$-3** as starting material. Whist the series of reactions identified key factors and conditions on synthesising the precipitated $Nb_2O_5$, the data on calcined material signifies that when scaling up the work further to produce a large quantity of material that can be used for PGM addition and

modification for visible light photocatalysis, the as made material should be calcined in order to obtain the best photocatalytic properties.

## 3.6 Further Scaling Up of Nanoparticulate $Nb_2O_5$

The initial scaling up by a factor of 10 produced material that was well characterized, and very comparable to the original material synthesised at a lower scale. In altering some of the variables of the precipitation, the scaled up material was superior to the original material in terms of surface area for example, with the surface area of **$Nb_2O_5$-nano** 214 $m^2$ $g^{-1}$, and **$Nb_2O_5$-6** 334 $m^2$ $g^{-1}$. It could be concluded therefore, that the synthetic technique is well suited to be scaled up, and scaling up by an addition factor is viable. Equipment was therefore used to synthesis a larger amount of material, to check the viability of scaling up the synthesis further; an added advantage is that this large amount of material could be used for further post synthetic modification such as the addition of PGMs or modification of material to promote visible light through addition of oxides.

The permanent equipment used for this scaled up synthesis is photographed in Figure 3-18. The equipment is comparable with that used previously, however is significantly larger in scale. The quantities of reagents chosen were chosen with the scale of the equipment in mind; the large container is able to hold 10 L of liquid, therefore the synthesis was scaled up so a maximum of 10 L would be present at the conclusion of the $NbCl_5$ solution addition. Two batches of $Nb_2O_5$ precipitate material were synthesised using this equipment: initially, the synthesis procedure that produced **$Nb_2O_5$-3** was used, scaled up by a factor of 3. The second batch was synthesized with the aim of producing the maximum amount of material that the equipment could provide, therefore the **$Nb_2O_5$-3** synthesis was modified so the concentration of the $NbCl_5$ solution was doubled to a 1 M solution, with the concentration of ammonia increased comparably.

**Figure 3-18** Equipment used in the synthesis of further scaled up material (**$Nb_2O_5$-B1** and **$Nb_2O_5$-B2**)

### 3.6.1 Synthesis of Further Scaled Up Nanoparticulate $Nb_2O_5$-B1 and $Nb_2O_5$-B2

Batch 1 of the further scaled up synthesis was synthesised by scaling up by a factor of 3 the synthetic route for **$Nb_2O_5$-3**, with the concentrations of the reagents consistent, but an increase in the amount of reagents used.

150 g (0.6 mol) of $NbCl_5$ were added slowly to 1.2 L of anhydrous EtOH, generating a clear yellow/green 0.5 M solution of $NbCl_5$. This solution was added to 6 L of a previously prepared 0.55 M solution of $NH_3$, under vigorous stirring, using a peristaltic pump, set to a rate of 20 ml $min^{-1}$. White precipitate was formed on addition of the $NbCl_5$ solution. At the conclusion of the addition, the suspension was allowed to stir for a further hour, before the precipitate material was collected by filtration, by transferring the suspension to a filter funnel under vacuum. This white precipitate material was continuously washed with

deionized water at a temperature of 60 °C, until the conductivity of the washings collected showed conductivity of less than 50 μS, as measured by a conductivity meter. This material was then further washed with 2 L of deionized water, and collected and dried overnight in an oven at 105 °C. The material was ground into a fine white powder (**$Nb_2O_5$-B1**). Calcined material (**$Nb_2O_5$-B1:500**) was synthesised by calcining **$Nb_2O_5$-B1** in a furnace at 500 °C for 2 hours, heating at 5 °C $min^{-1}$ and cooling at 10 °C $min^{-1}$.

Batch 2 of the further scaled up synthesis was synthesised by scaling the synthesis of **$Nb_2O_5$-B1** by 1.3, as this gave close to 10 L of suspension after final addition of the $NbCl_5$ solution. The synthesis procedure was further modified by doubling the concentration of the $NbCl_5$ solution, in addition to doubling the concentration of the ammonia solution to ensure the entire precipitation occurs under basic conditions. The $NbCl_5$ solution was added to the ammonia solution at the same rate of addition of moles $min^{-1}$, therefore as the solution of the Batch 2 $NbCl_5$ is double the concentration of Batch 1 $NbCl_5$, the addition rate of the $NbCl_5$ solution for halved for the Batch 2 synthesis.

390 g (1.4 mol) of $NbCl_5$ were added slowly to 1.56 L of anhydrous EtOH, generating a clear yellow/green 1 M solution of $NbCl_5$. This solution was added to 7.8 L of a previously prepared 1.11 M solution of $NH_3$, under vigorous stirring, using a peristaltic pump, set to a rate of 10 ml $min^{-1}$. After the addition, the suspension was allowed to age for a further hour under vigorous stirring. The precipitate material was collected by filtration, by transferring the suspension to a filter funnel under vacuum. This white precipitate material was continuously washed with deionized water at a temperature of 60 °C, until the conductivity of the washings collected showed conductivity of less than 50 μS, as measured by a conductivity meter. The material was then washed with a further 2 L of deionized water, and collected and dried overnight in an oven at 105 °C. The material was ground into a fine white powder (**$Nb_2O_5$-B2**). Calcined material (**$Nb_2O_5$-B2:500**) was synthesised by

calcining **$Nb_2O_5$-B2** in a furnace at 500 °C for 2 hours, heating at 5 °C $min^{-1}$ and cooling at 10 °C $min^{-1}$.

## 3.6.2 Characterisation of $Nb_2O_5$-B1 and $Nb_2O_5$-B2

| | $NbCl_5$ / EtOH | $NH_3$ Conc / M | Temp | Dropper / Pump | EtOH to Base | Surface area / $m^2$ $g^{-1}$ | Particle size from SA / nm | Direct Band Gap / eV |
|---|---|---|---|---|---|---|---|---|
| B1 | 150 g / 1.2 L | 0.55 | RT | Pump | Yes | 254 | 5.1 | 3.82 |
| B2 | 390 g / 1.56 L | 1.11 | RT | Pump | Yes | 228 | 5.7 | 3.86 |

**Table 3-5** Table showing the synthetic conditions for synthesising nanoparticulate **$Nb_2O_5$-B1** and **$Nb_2O_5$-B2**, with initial characterisation: surface area, particle size determined from surface area and the direct band gap.

A summary of the conditions used in the two synthesis procedures is illustrated in Table 3-5 in addition to initial characterisation of BET surface area, particle size determined from surface area, and the direct band gap of the material. Both **$Nb_2O_5$-B1** and **$Nb_2O_5$-B2** show properties comparable with previously synthesised material by the precipitation route. The surface area of 254 $m^2$ $g^{-1}$ and 228 $m^2$ $g^{-1}$ for **$Nb_2O_5$-B1** and **$Nb_2O_5$-B2** respectively is lower in value than **$Nb_2O_5$-3**, synthesised by a comparable route, however both **$Nb_2O_5$-B1** and **$Nb_2O_5$-B2** show surface areas slightly higher than **$Nb_2O_5$-nano**, the low scale material, indicating initially that the reaction has been successfully further scaled up. The direct band gap calculation is also comparable to previously synthesised precipitate material, with 3.82 eV and 3.86 eV for **$Nb_2O_5$-B1** and **$Nb_2O_5$-B2** respectively consistent with comparable particle size material.

As with previous synthesised material, TGA showed weight loss, in the case of **$Nb_2O_5$-B1**, just over 11% up to a temperature of around 400 °C. CHN analysis of **$Nb_2O_5$-B1** showed a hydrogen content of 1.42%, and a nitrogen content of 1.88% indicating that ammonia is

still present is the material from the synthesis; chlorine analysis confirmed negligible chlorine present, with less than 20 ppm of chlorine detected. From the TGA and CHN data, the precipitate formula can be calculated to be $\mathbf{Nb_2O_5(H_2O)_{1.53}(NH_3)_{0.39}}$.

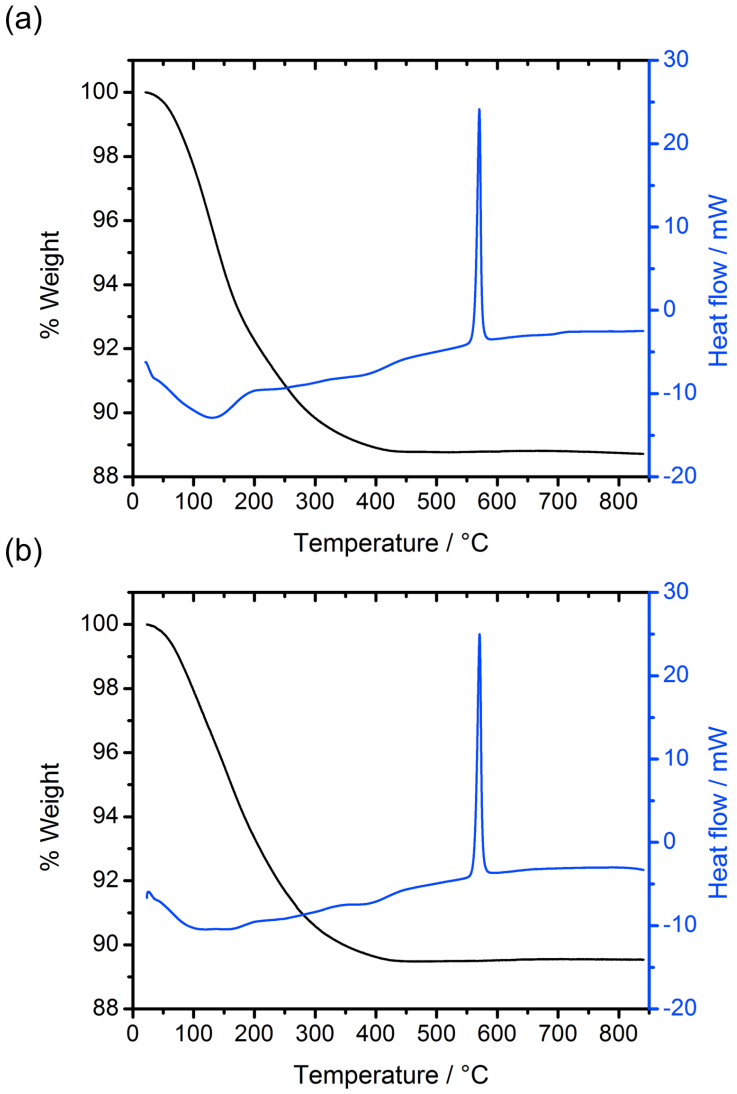


**Figure 3-19** TGA data for **$Nb_2O_5$-B1** (a) and **$Nb_2O_5$-B2** (b) showing the weight loss and the heat flow difference when heated to 800 °C

**$Nb_2O_5$-B2** was similarly characterised by TGA, which showed 10% weight loss up to around 400 °C. CHN analysis of **$Nb_2O_5$-B2** showed comparable hydrogen content of 1.42% compared with **$Nb_2O_5$-B1**, however the nitrogen content of **$Nb_2O_5$-B2** was larger, at 2.29%. This indicates more ammonia is present in this material compared with **$Nb_2O_5$-**

**B1**, indicating the washing procedure used in this synthesis was not as effective in removing the ammonia, as with the **$Nb_2O_5$-B1** synthesis although chlorine analysis indicated negligible chlorine (less than 20 ppm). The larger amount of material present in the filtration apparatus – more than double compared with **$Nb_2O_5$-B1**, could indicate further washing would have been required. The formula calculated from this material from the TGA and CHN data is **$Nb_2O_5(H_2O)_{1.39}(NH_3)_{0.48}$**.

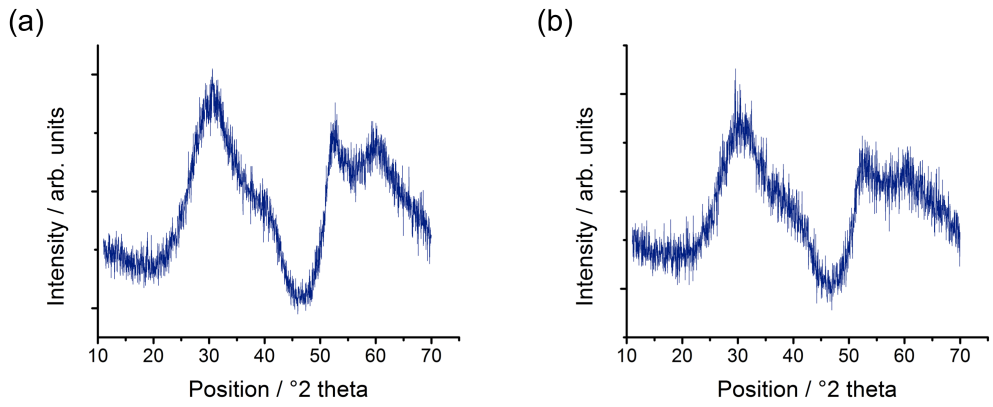


**Figure 3-20** X-ray diffraction pattern of **$Nb_2O_5$-B1:500** (a) and **$Nb_2O_5$-B2:500** (b), both showing a semi-amorphous structure.

XRD of material calcined at 500 °C showed patterns comparable with previously synthesised material calcined at 500 °C (Figure 3-20). Both **$Nb_2O_5$-B1:500** and **$Nb_2O_5$-B2:500** showed a semi-amorphous structure with broad peaks roughly corresponding to the pseudo-hexagonal phase of $Nb_2O_5$. This is expected due to the calcination taking place at a temperature below that of the heat of crystalisation evident by the increase in heat at 580 °C on the TGA of both **$Nb_2O_5$-B1** and **$Nb_2O_5$-B2**.

Methyl orange degradation was carried out with **$Nb_2O_5$-B1:500** and **$Nb_2O_5$-B2:500**, with 1 g L-1 of catalyst, reacted with 6.11 x $10^{-5}$ M methyl orange under UV light (300 W Xe lamp) for using the experimental set and measurements described in Chapter 2. Both **$Nb_2O_5$-B1:500** and **$Nb_2O_5$-B2:500** show degradation of methyl orange comparable with previous material calcined at 500 °C (**$Nb_2O_5$-1:500**, **$Nb_2O_5$-3:500**).

The characterisation data of **$Nb_2O_5$-B1**, **$Nb_2O_5$-B1:500** and **$Nb_2O_5$-B2 $Nb_2O_5$-B2:500**, is summarized in Table 3-6.

| Sample | Calcination temp / °C | Surface area / $m^2$ $g^{-1}$ | Direct band gap / eV | MO degradation % / hour | Cl content / ppm | TGA weight loss / % | CHN |
|---|---|---|---|---|---|---|---|
| B1 | - | 254 | 3.82 | - | < 20 | 11 | C - / H 1.42 / N 1.88 |
| | 500 | 129 | 3.59 | 9 | | 2.5 | C - / H 0.59 / N - |
| B2 | - | 228 | 3.86 | - | < 20 | 12 | C - / H 1.27 / N 2.34 |
| | 500 | 118 | 3.56 | 9 | | 3 | C - / H 0.58 / N - |

**Table 3-6** Summary of the characterisation of **$Nb_2O_5$-B1**, **$Nb_2O_5$-B1:500** and **$Nb_2O_5$-B2**, **$Nb_2O_5$-B2:500**.

## 3.7 Conclusion

As evident from literature discussed in the introduction, $Nb_2O_5$ is an interesting and viable photocatalyst; the nanoparticulate synthetic route described in this chapter provides a comparatively simple way of synthesising a quantity of over 200 g of $Nb_2O_5$ material that can be successfully used as a photocatalyst. The comparable properties of the low, medium and large-scale material synthesised demonstrate the viability of scaling up this type of precipitation synthesis. The simplicity of this synthesis also opens up the possibility of synthesising comparable material such as tantalum oxide ($Ta_2O_5$) in this way.

The well characterised **$Nb_2O_5$-B1:500** and **$Nb_2O_5$-B2:500** can be used as the starting material for work involving the addition of PGMs discussed in Chapter 4, and addition of chromium (III) oxide as a route to visible light photocatalysis, discussed in Chapter 5.

## 3.8 References

[1] F. E. Osterloh, *Chem. Mater.* **2008**, *20*, 35-54.

[2] K. Domen, A. Kudo, M. Shibata, A. Tanaka, K. Maruya, T. Onishi, *J. Chem. Soc., Chem. Commun.* **1986**, 1706-1707.

[3] Y. Ebina, T. Sasaki, M. Harada, M. Watanabe, *Chem. Mater.* **2002**, *14*, 4390-4395.

[4] Y. Ebina, N. Sakai, T. Sasaki, *J. Phys. Chem. B* **2005**, *109*, 17212-17216.

[5] O. C. Compton, E. C. Carroll, J. Y. Kim, D. S. Larsen, F. E. Osterloh, *J. Phys. Chem. C* **2007**, *111*, 14589-14592.

[6] K. Maeda, M. Eguchi, S.-H. A. Lee, W. J. Youngblood, H. Hata, T. E. Mallouk, *J. Phys. Chem. C* **2009**, *113*, 7962-7969.

[7] B. O'Regan, M. Grätzel, *Nature* **1991**, *353*, 737-740.

[8] Y. Matsumoto, *J. Solid State Chem.* **1996**, *126*, 227-234.

[9] K. Sayama, H. Sugihara, H. Arakawa, *Chem. Mater.* **1998**, *10*, 3825-3832.

[10] K. Eguchi, H. Koga, K. Sekizawa, K. Sasaki, *J. Ceram. Soc. Jpn.* **2000**, *108*, 1067-1071.

[11] F. Lenzmann, J. Krueger, S. Burnside, K. Brooks, M. Grätzel, D. Gal, S. Ruhle, D. Cahen, *J. Phys. Chem. B* **2001**, *105*, 6347-6352.

[12] X. Ai, J. C. Guo, N. A. Anderson, T. Q. Lian, *J. Phys. Chem. B* **2004**, *108*, 12795-12803.

[13] H. Kominami, K. Oki, M. Kohno, S. Onoue, Y. Kera, B. Ohtani, *J. Mater. Chem.* **2001**, *11*, 604-609.

[14] P. D. Yang, D. Y. Zhao, D. I. Margolese, B. F. Chmelka, G. D. Stucky, *Nature* **1998**, *396*, 152-155.

[15] P. D. Yang, D. Y. Zhao, D. I. Margolese, B. F. Chmelka, G. D. Stucky, *Chem. Mater.* **1999**, *11*, 2813-2826.

[16] X. Chen, T. Yu, X. Fan, H. Zhang, Z. Li, J. Ye, Z. Zou, *Appl. Surf. Sci.* **2007**, *253*, 8500-8506.

[17] M. K. Silva, R. G. Marques, N. Machado, O. A. A. Santos, *Braz. J. Chem. Eng.* **2002**, *19*, 359-363.

[18] A. G. S. Prado, E. A. Faria, J. R. SouzaDe, J. D. Torres, *J. Mol. Catal. A: Chem.* **2005**, *237*, 115-119.

[19] J. D. Torres, E. A. Faria, J. R. SouzaDe, A. G. S. Prado, *J. Photochem. Photobiol., A* **2006**, *182*, 202-206.

[20] A. G. S. Prado, L. B. Bolzon, C. P. Pedroso, A. O. Moura, L. L. Costa, *Appl. Catal., B* **2008**, *82*, 219-224.

[21] B. Lee, D. L. Lu, J. N. Kondo, K. Domen, *J. Am. Chem. Soc.* **2002**, *124*, 11256-11257.

[22] D. M. Antonelli, J. Y. Ying, *Angew. Chem. Int. Ed.* **1996**, *35*, 426-430.

[23] R. Brayner, F. Bozon-Verduraz, *PCCP* **2003**, *5*, 1457-1466.

[24] B. M. Gatehouse, A. D. Wadsley, *Acta Crystallogr.* **1964**, *17*, 1545-1554.

[25] A. A. Mcconnell, J. S. Anderson, C. N. R. Rao, *Spectrochim. Acta, Part A* **1976**, *32*, 1067-1076.

[26] T. Ikeya, M. Senna, *J. Non-Cryst. Solids* **1988**, *105*, 243-250.

[27] J. M. Jehng, I. E. Wachs, *Chem. Mater.* **1991**, *3*, 100-107.

[28] N. Ozer, M. D. Rubin, C. M. Lampert, *Sol. Energy Mater. Sol. Cells* **1996**, *40*, 285-296.

[29] C. O. Avellaneda, A. Pawlicka, M. A. Aegerter, *J. Mater. Sci.* **1998**, *33*, 2181-2185.

[30] M. Macek, B. Orel, *Sol. Energy Mater. Sol. Cells* **1998**, *54*, 121-130.

[31] S. A. O'Neill, I. P. Parkin, R. J. H. Clark, A. Mills, N. Elliott, *J. Mater. Chem.* **2003**, *13*, 2952-2956.

[32] M. E. Gimon-Kinsel, K. J. Balkus, *Microporous Mesoporous Mater.* **1999**, *28*, 113-123.

[33] R. Romero, J. R. Ramos-Barrado, F. Martin, D. Leinen, *Surf. Interface Anal.* **2004**, *36*, 888-891.

[34] N. Uekawa, T. Kudo, F. Mori, Y. J. Wu, K. Kakegawa, *J. Colloid Interface Sci.* **2003**, *264*, 378-384.

[35] K. S. W. Sing, D. H. Everett, R. A. W. Haul, L. Moscou, R. A. Pierotti, J. Rouquerol, T. Siemieniewska, *Pure Appl. Chem.* **1985**, *57*, 603-619.

[36] Y. Wang, N. Herron, *J. Phys. Chem.* **1991**, *95*, 525-532.

[37] A. Alsalme, E. F. Kozhevnikova, I. V. Kozhevnikov, *Appl. Catal., A* **2008**, *349*, 170-176.

[38] G. T. Brown, J. R. Darwent, *J. Phys. Chem.* **1984**, *88*, 4955-4959.

# 4 Platinum Group Metals on Niobium Oxide

## 4.1 Introduction

As described in Chapter 1, Platinum Group Metals (PGMs) have played a significant role in photocatalysis, in particular since the landmark paper by Honda and Fujishima generating hydrogen from rutile $TiO_2$ with a platinum electrode. [1] Whilst in this system, the platinum was used as an electrode in the photolysis of water, the major role of PGMs in photocatalysis involving particulate material is as a co-catalyst. In a co-catalyst/semiconductor system, the co-catalyst plays the role of active site for the reduction or oxidation processes that take place after photo-excitation takes place, assisting with the separation of holes and electrons; in the case of platinum, it is thought to act as an electron trap, and so limiting surface electron / hole recombination, and facilitating the transfer of the electron to the absorbent such as water.[2]

In 1985, Yamaguti and Sato, having studied the photolysis of water with powdered Pt-$TiO_2$,[3] also looked at other PGMs as co-catalysts in the photolysis reaction, testing rhodium and palladium in addition to platinum.[4] In their experiments, of the 3 PGMs, rhodium, with Rh-$TiO_2$ gave the highest generation rate of hydrogen, whilst palladium Pd-$TiO_2$ gave the lowest rate of hydrogen generation. The group also noted that the rhodium deposited catalyst was found to be the least active for the back reaction of oxygen and hydrogen forming water, with palladium based Pd-$TiO_2$ less active than Pt-$TiO_2$ for the back reaction. From this early work, many powdered semiconductors were developed as photocatalysts for water splitting; all required a co-catalyst to perform to the maximum efficiency, with the vast majority using platinum as the hydrogen generation co-catalyst, with $RuO_2$ generally used as a co-catalyst for oxygen generation.[5] In more recent years, work has been carried out to survey PGMs as a co-catalyst.

Ohtani et al. presented a detailed analysis of the role of platinum nanoparticles on $TiO_2$ in a paper published in 1997,[6] where $TiO_2$ photocatalysts with varying amounts of platinum were prepared by an impregnation method, impregnating the $TiO_2$ with a platinum precursor (chloroplatinic acid), and then calcining in a hydrogen / nitrogen atmosphere – this reduction step ensuring that platinum metal nanoparticles were deposited on the surface. The resulting material was characterised by XPS, confirming the platinum (0) oxidation state, and TEM, observing 1 – 2 nm size platinum particles on the surface of the $TiO_2$. The group also determined the surface area of platinum by volumetric gas adsorption measurements, with hydrogen as the adsorption gas. IR analysis indicated that after the reduction step of the synthesis of Pt-$TiO_2$, there is gradual oxidation of the platinum (0) surface under storage under ambient conditions. The group found, when reacting with water and 2-propanol as a sacrificial reagent, the maximum rate of hydrogen generation occurred between 0.2 and 0.5% weight platinum on $TiO_2$, with increasing the platinum content beyond 1% by weight having little effect on the rate of reaction. The group concluded that only one platinum particle is required for hydrogen generation on a $TiO_2$ particle around 24 nm in size. This type of detailed analysis of the platinum on the surface of $TiO_2$ is rarely seen in literature; the group also notes that negligible hydrogen is generated from the system when using the unpromoted $TiO_2$.

Michael Bowker's group in a series of papers published from 1999 undertook a similarly detailed analysis of PGMs on $TiO_2$.[2, 7-8] The group found that significant amounts of hydrogen were generated from a methanol solution with only 0.001% by weight palladium on $TiO_2$ (P25) and so possibly agreeing with the work by Ohtani, who suggested one platinum particle per particle of $TiO_2$ is required to improve the efficiency. The maximum rate of hydrogen production was found with material modified by 0.5% by weight palladium on P25, with the palladium added from a chlorine based metal salt ($PdCl_2$) via an incipient wetness impregnation technique. Although detailed characterisation of the palladium on the surface of the $TiO_2$ was not performed, the group did suggest an

interesting reaction mechanism, suggesting the hydrogen is emanating from the photocatalytic degradation of methanol in addition to degradation of water, with the active site for the generation of hydrogen from water located at the periphery of the palladium particle on $TiO_2$, and methanol liberating hydrogen from the palladium particle.

Photocatalytic literature surveyed in the introduction of this thesis stresses the importance of co-catalysts in improving the efficiency of the photocatalytic reactions, and in some cases, points out that the reaction products are negligible without the co-catalyst support. It is therefore surprising that there is not more detailed analysis on exactly the interaction between the semiconductor and co-catalyst, with the studies by Ohtani and Bowker discussed previously being the most detailed studies found. The work in this Chapter was structured to provide a similarly detailed characterisation and analysis of a series of PGM co-catalysts. Unlike the work by Bowker and Ohtani, which used $TiO_2$ as the PGM support, the work described here used $Nb_2O_5$, the synthesis and characterisation of which is described in Chapter 3. This material, as will be seen, can generate a significant amount of hydrogen without any PGMs added, unlike $TiO_2$ (P25), which can produce only a negligible amount, possibly due to the hydrogen being generated by the anatase portion of P25, with rutile claimed have a reduction potential more positive than $H^+/H_2$, and so unable to generate hydrogen.[9] This contrasts with $Nb_2O_5$, which with a larger band gap, has a greater reduction potential than anatase or rutile $TiO_2$.[10]

Two methods were used to add platinum to the $Nb_2O_5$, based on literature methods, which are the most common methods of depositing platinum group metals onto photocatalysts[5]: photodeposition, based on the method first used by Bard,[11] and an impregnation method, comparable to that used by the Ohtani group,[6] and the Bowker group.[2] In addition to platinum, rhodium, found to have the best rate for hydrogen generation in Yamaguti and Sato's work,[4] and palladium, used extensively in Bowker's work were chosen.[2, 7-8] Whilst chloroplatinic acid was used in the photodeposition of platinum, PGM nitrates were

used in the impregnation addition. By using the nitrate, there is no issue of removing the chlorine; additionally CHN will be able to determine whether there is any nitrate remaining after calcination.

As a final experiment, the work of Gratzel was replicated, by adding both $RuO_2$ and platinum to the $Nb_2O_5$, with the aim of further improving the efficiency. Whilst the results were not positive in respect of pure water splitting, the data produced in this chapter are an excellent starting point to improving the addition of PGMs to the $Nb_2O_5$ system, so pure water splitting with material based on $Nb_2O_5$ is a real possibility.

## 4.2 Synthesis and Characterisation of PGM Added Material

### 4.2.1 Addition of Platinum to $Nb_2O_5$ by the Impregnation Method

Platinum was added to the $Nb_2O_5$ support by taking advantage of the incipient wetness method for the impregnation of the platinum solution.[12] The synthesis of the $Nb_2O_5$ used in the impregnation was described in Chapter 3 (**$Nb_2O_5$-B2:500**); a significant feature of this material was the high surface area (118 $m^2\ g^{-1}$). This high surface area, in conjunction with the small particle size (11 nm), gives the material a high incipient wetness property, with the point of incipient wetness at 0.4 ml $g^{-1}$, indicating that 0.4 ml of liquid is required to coat 1 g of the particles. By dissolving a metal precursor in this liquid, the metal ions will also coat the surface of the particles. Calcining this material will remove the non-metal content of the precursor; calcining in oxidizing conditions will provide the metal oxide; calcining under reducing conditions will allow the metal itself. Due to its high solubility in water, platinum (IV) nitrate is an ideal precursor for the addition of platinum using this method. Calcining in air at 350 °C will remove the nitrate precursor, and give nanoparticles of platinum oxide on the surface of the $Nb_2O_5$; by continuing the synthesis

and calcining this material under a mixture of 5% hydrogen and 95 % nitrogen, the platinum oxide on the surface should be reduced to platinum metal. A range of platinum impregnation samples were prepared, ranging from 0.01% by weight platinum content through to 1% by weight platinum content; the synthesis method was identical for each sample apart from the amount of platinum precursor used.

In the 1% by weight platinum synthesis, 10 g of $Nb_2O_5$ (**$Nb_2O_5$-B2:500)** was used. 0.6223 g of platinum (IV) nitrate solution ($Pt(NO_3)_4$, Pt assay of the solution determined to be 16.07%, provided by Johnson Matthey) was weighed out in a beaker, and distilled water was added to make up the final solution to 4 ml. The 10 g of **$Nb_2O_5$-B2:500** was added to the solution, and mixed thoroughly with a spatula over the space of 30 minutes, with the material at the point of incipient wetness. This material was dried overnight in an oven at 105 °C (**1Pt-$Nb_2O_5$-U**). To remove the nitrate precursor, the material was placed in a boat crucible, and calcined in a furnace at 350 °C for 3 hours, heating at 5 °C $min^{-1}$, cooling at 10 °C $min^{-1}$. The material (**1Pt-$Nb_2O_5$-A**) was then ground, placed back into a aluminum boat crucible, and placed in a tube furnace with flowing 5% hydrogen / 95 % nitrogen gas. The tube furnace was kept at room temperature for 30 minutes with the gas flowing; the furnace was then heated to 300 °C at 5 °C $min^{-1}$, kept at 300 °C for 3 hours, then cooled to room temperature with flowing 5% hydrogen / 95% nitrogen at 10 °C $min^{-1}$. The hydrogen / nitrogen flow was turned off once the furnace was at room temperature. The tube furnace was exposed to air, and the grey powder was removed from the furnace (**1Pt-$Nb_2O_5$**).

0.5% added platinum by weight was synthesised by a comparable method, **(2Pt- $Nb_2O_5$)** as was 0.1% (**3Pt-$Nb_2O_5$**) and 0.01% platinum by weight (**4Pt-$Nb_2O_5$**), with the amount of platinum (IV) nitrate modified to reflect the amount of platinum required.

### 4.2.2 Addition of Platinum to $Nb_2O_5$ by the Photodeposition Method

As a comparison to the impregnation method, 1% by weight platinum was added to $Nb_2O_5$ by the photodeposition method. Again the $Nb_2O_5$ used in the synthesis was the material characterised in Chapter 3 (**$Nb_2O_5$-B2:500**). Placing a suspension of $Nb_2O_5$, chloroplatinic acid ($H_2PtCl_6$) and methanol ($CH_3OH$) under anaerobic conditions under UV light allows the platinum (IV) to be reduced to platinum (0) nanoparticles by the photo-electrons produced by irradiating the $Nb_2O_5$; the photo-holes oxidise the methanol into acetone.

For the photodeposition, 1.2 g of $Nb_2O_5$ (**$Nb_2O_5$-B2:500**) was used. 0.3151 g of $H_2PtCl_6$ (Sigma-Aldrich; 8% $H_2PtCl_6$ assay) was added to 1 L of a 1% methanol solution previously prepared (10 ml of $CH_3OH$ added to a volumetric flask, with distilled water added to make up the solution to 1000 ml). 500 ml of this solution was added to both of two 500 ml reactors, and 0.6 g of $Nb_2O_5$ was added to each reactor, with both reactors then sealed. The reactors were both purged with nitrogen in the dark for 1 hour, to ensure anaerobic conditions. Each reactor was then placed under a UV light set up, consisting of two half-cylinder arrangements of 6 x 8 W Coast Wave Backlight UVA lamps. The reactors were irradiated for 4 hours; the two suspensions were then combined, and the platinized $Nb_2O_5$ was then collected by centrifuging the suspension for 15 minutes at a speed of 3000 rpm. The material was washed by adding distilled water, and centrifuging for a further 15 minutes at 3000 rpm. This grey material was then collected and dried overnight at 105 °C (**6Pt- $Nb_2O_5$**).

### 4.2.3 Addition of Rhodium or Palladium to $Nb_2O_5$ by the Impregnation Method

Rhodium or palladium metal was also added to $Nb_2O_5$ support, to provide additional PGMs for comparison with platinum. As with the platinum addition synthesis, a range of PGM weight percentages were synthesised, ranging from 0.01% to 1%.

In the 1% by weight rhodium addition synthesis, 10 g of $Nb_2O_5$ (**$Nb_2O_5$-B2:500**) was used. 0.8137 g of rhodium (III) nitrate solution ($Rh(NO_3)_3$, Rh assay of the solution determined to be 12.29%, provided by Johnson Matthey) was weighed out, and distilled water was added to make the final solution up to 4 ml. The 10 g of **$Nb_2O_5$-B2:500** was added to the solution, and mixed thoroughly with a spatula over the space of 30 minutes, with the material at the point of incipient wetness. This material was dried overnight in an oven at 105 °C (**1Rh-$Nb_2O_5$-U**). **1Rh-$Nb_2O_5$-U** was calcined in an identical fashion to **1Rh-$Nb_2O_5$-U**, proceeding through the calcination step in air (**1Rh-$Nb_2O_5$-A**), finally yielding 1% added rhodium metal – $Nb_2O_5$ after the reduction step in 5% hydrogen / 95% nitrogen (**1Rh-$Nb_2O_5$**).

0.5% added rhodium by weight was synthesised by a comparable method, (**2Rh- $Nb_2O_5$**) as was 0.1% (**3Rh-$Nb_2O_5$**) and 0.01% platinum by weight (**4Rh- $Nb_2O_5$**), with the amount of rhodium (III) nitrate modified to reflect the amount of rhodium required.

In the 1% by weight palladium synthesis, 10 g of $Nb_2O_5$ (**$Nb_2O_5$-B2:500**) was used. 0.19 g of palladium (II) nitrate solution ($Pd(NO_3)_2$, Pd assay of the solution determined to be 8.37%, provided by Johnson Matthey) was weighed out, and distilled water was added to make up the final solution to 4 ml. The 10 g of **$Nb_2O_5$-B2:500** was added to the solution, and mixed thoroughly over the space of 30 minutes with a spatula, with the material at the point of incipient wetness. This material was dried overnight in an oven at 105 °C (**1Pd-$Nb_2O_5$-U**). **1Pd-$Nb_2O_5$-U** was calcined in an identical fashion to **1Pt-$Nb_2O_5$-U**,

proceeding through the calcination step in air, yielding 1% added palladium metal – $Nb_2O_5$ after the reduction step in air (**1Pd-$Nb_2O_5$**).

0.5% added palladium by weight was synthesised by a comparable method, (**2Pd- $Nb_2O_5$**) as was 0.1% (**3Pd-$Nb_2O_5$**) and 0.01% platinum by weight (**4Pd-$Nb_2O_5$**), with the amount of palladium (II) nitrate modified to reflect the amount of palladium required.

| Material | Code | ICP % PGM |
|---|---|---|
| 1% Pt-$Nb_2O_5$ | **1Pt-$Nb_2O_5$** | 0.94 |
| 0.5% Pt- $Nb_2O_5$ | **2Pt-$Nb_2O_5$** | 0.46 |
| 0.1% Pt- $Nb_2O_5$ | **3Pt-$Nb_2O_5$** | 0.10 |
| 0.01% Pt- $Nb_2O_5$ | **4Pt-$Nb_2O_5$** | |
| 1% Pt- $Nb_2O_5$ (Photodeposition) | **6Pt-$Nb_2O_5$** | 0.90 |
| | | |
| 1% Rh-$Nb_2O_5$ | **1Rh-$Nb_2O_5$** | 0.95 |
| 0.5% Rh- $Nb_2O_5$ | **2Rh-$Nb_2O_5$** | 0.49 |
| 0.1% Rh- $Nb_2O_5$ | **3Rh-$Nb_2O_5$** | 0.10 |
| 0.01% Rh- $Nb_2O_5$ | **4Rh-$Nb_2O_5$** | |
| | | |
| 1%Pd-$Nb_2O_5$ | **1Pd-$Nb_2O_5$** | 1.00 |
| 0.5%Pd- $Nb_2O_5$ | **2Pd-$Nb_2O_5$** | 0.51 |
| 0.1%Pd- $Nb_2O_5$ | **3Pd-$Nb_2O_5$** | 0.11 |
| 0.01%Pd- $Nb_2O_5$ | **4Pd-$Nb_2O_5$** | |

**Table 4-1** Summary of the PGM added $Nb_2O_5$ material synthesised, along with a code to identify the sample, with ICP determined PGM content, carried out at the Johnson Matthey Technology Centre.

A summary of the material synthesised, in addition to the ICP determined PGM content of the material synthesized is give in Table 4-1. Each material is assigned a code including the PGM used, which will be used in the discussion of this chapter. The ICP data provided, which was carried out at the Johnson Matthey Technology Centre, confirm that the platinum group metals were successfully impregnated or photodeposited into the $Nb_2O_5$

support, indicating that both methods provide successful routes to synthesising PGM added material.

### 4.2.4 Characterisation of PGM-$Nb_2O_5$ material

A summary of the synthesis of **1Pt-$Nb_2O_5$** is illustrated in Scheme 4-1

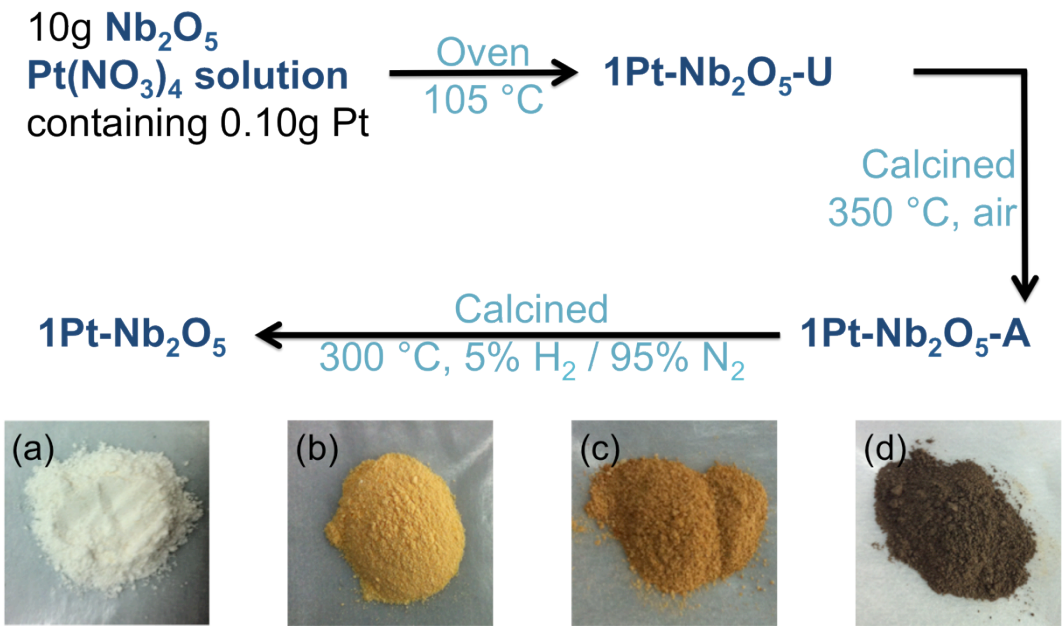


**Scheme 4-1** Schematic illustrating the synthesis of **1Pt-$Nb_2O_5$** from platinum (IV) nitrate solution, and **$Nb_2O_5$-B2:500**, in addition to photographs of the material at different stages of the synthesis: (a) **$Nb_2O_5$-B2:500**; (b) **1Pt-$Nb_2O_5$-U**; (c) **1Pt-$Nb_2O_5$-A**; (d) **1Pt-$Nb_2O_5$**.

Figure 4-1(a) shows the TGA data for material after the platinum (IV) nitrate is impregnated into the niobium oxide (**1Pt-$Nb_2O_5$-U**), indicating the weight loss as the temperature increases, in addition to the heat flow. As the temperature increases, there is a decrease in the weight, caused by the nitrate decomposing. The weight loss stabilizes around 300 °C, indicating the nitrate removal is complete at this temperature. CHN data of material calcined at 350 °C for 3 hours (**1Pt-$Nb_2O_5$-A**) confirms this is the case, with the no nitrogen detected by CHN analysis. With this material then calcined under 5% hydrogen and 95% nitrogen at 300 °C, the yellow / orange platinum oxide species is reduced to the dark grey platinum metal on the surface of niobium oxide (**1Pt-$Nb_2O_5$**). ICP

analysis of **1Pt-$Nb_2O_5$** gives a platinum content of 0.94%, confirming the presence of platinum in this material.

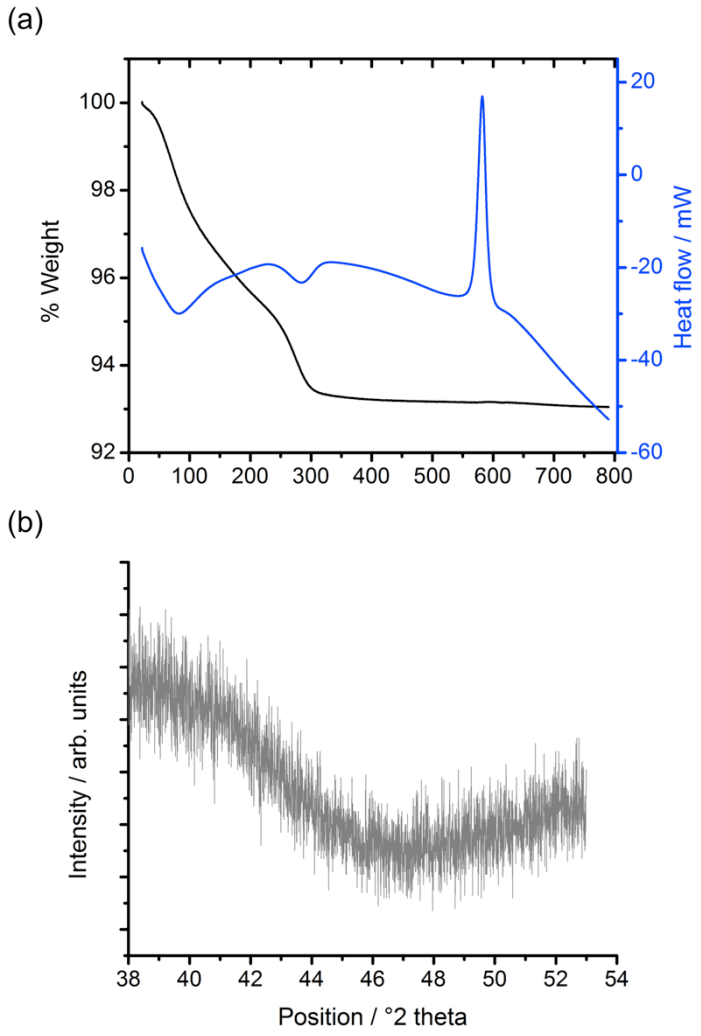


**Figure 4-1** (a) TGA data for **1Pt-$Nb_2O_5$-U**, illustrating the weight loss and the heat flow difference. (b) High resolution XRD spectra of **1Pt-$Nb_2O_5$** between 38 and 53 ° 2 theta, with a platinum diffraction peak expected at 46.5 ° 2 theta.

Figure 4-1(b) shows a high resolution XRD spectrum of **1Pt-$Nb_2O_5$**, between 48 and 53 °2 theta. Swanson and Tatgne determined the XRD spectra of platinum metal, noting a significant peak at 46.5 °2 theta (ICCD file 00-004-0802). The XRD spectra of **1Pt-$Nb_2O_5$** does not show a peak at this angle, indicating the platinum particle on the surface of the

$Nb_2O_5$ does not diffract, plausibly as the size of the particles are below the diffraction limit.

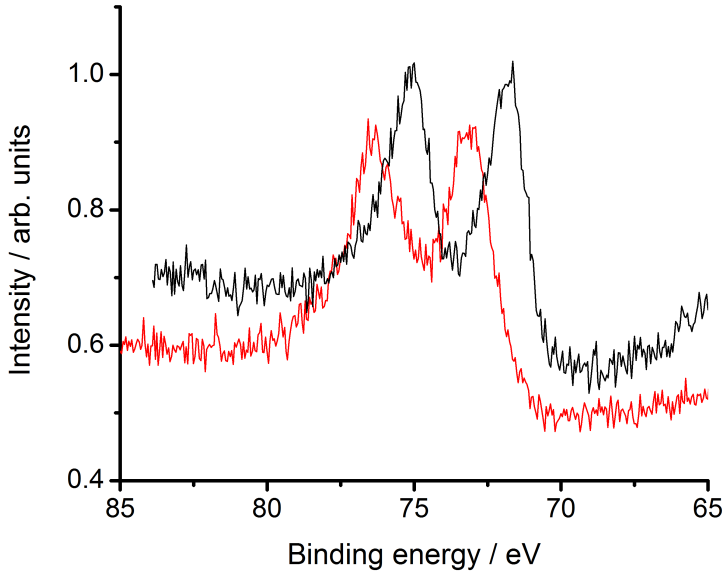


**Figure 4-2** XPS spectra for **1Pt-$Nb_2O_5$-A** (red line) and **1Pt-$Nb_2O_5$** (black line)

XPS analysis of **1Pt-$Nb_2O_5$-A** indicates that there is no platinum metal present in the material. As platinum is in the +4 oxidation state when the $Nb_2O_5$ is initially impregnated, this is not surprising, as the initial calcination is performed in air - essentially mild oxidizing conditions. With platinum (II) oxide (PtO) and platinum (IV) oxide ($PtO_2$) having a 4f binding energy of 72.9 eV and 74.5 eV respectively, the binding energy of platinum 4f in **1Pt-$Nb_2O_5$-A**, at 73.3 eV, lies in between these values, indicating that both platinum (II) oxide and platinum (IV) oxide are present. After the reduction step, the binding energy of platinum 4f shifts to 71.6 eV, close to the literature value of platinum (0) (71.5 eV), indicating that the reduction step has produced platinum (0) as expected. The Nb 3d peaks appear at the same energy in both the pre and post reduction samples, indicating that the reduction step has no effect on the oxidation state of niobium in the sample.

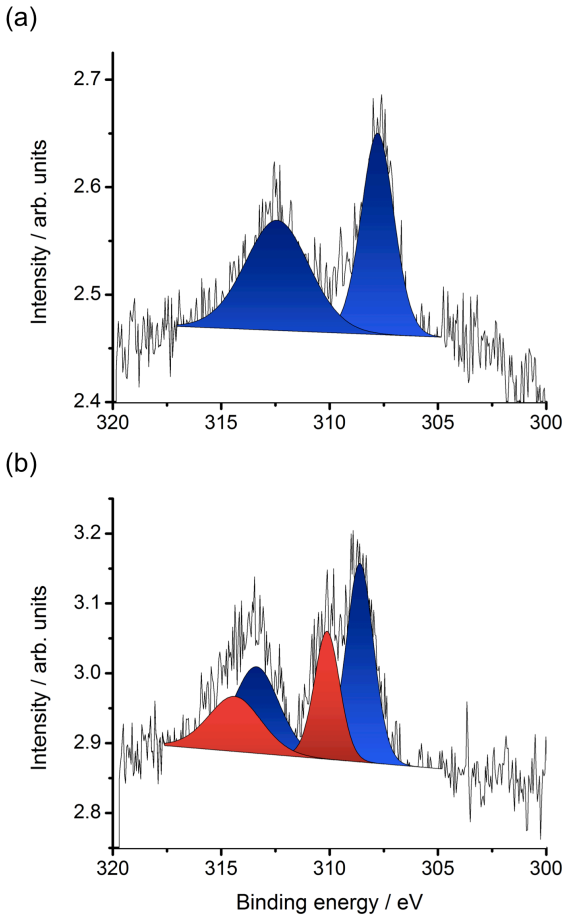


**Figure 4-3** XPS of (a) **1Rh-$Nb_2O_5$** and (b) **1Rh-$Nb_2O_5$-A**, with the multiple oxide states of rhodium fitted.

A comparable analysis can be found considering the XPS data for **1Rh-$Nb_2O_5$-A** and **1Rh-$Nb_2O_5$**. Again, from XPS spectra of **1Rh-$Nb_2O_5$-A**, two components can be identified and fitted, with the binding energy of the rhodium 3d electrons consistent with literature values of rhodium (III) oxide species (309.6 eV) and rhodium (I) oxide species (308.0 eV). **1Rh-$Nb_2O_5$** shows a single component present, with the binding energy close to the literature value of rhodium (0) (306.5 eV). As with the platinum based material, the Nb 3d peaks appear at the same energy in both **1Rh-$Nb_2O_5$-A** and **1Rh-$Nb_2O_5$**.

Qualitative and quantitative information regarding the PGM nanoparticles can be found using TEM and EDX. Figure 4-4 illustrates TEM images of **1Pt-$Nb_2O_5$** at 145,000 x magnification (a) and 450,000 x magnification (b). Qualitatively, there is evidence of

platinum present in the small dark patches one of which is highlighted in Figure 4-4 (b) with an orange circle, indicating platinum nanoparticles of around 1 nm in size. More quantitative evidence for platinum present on the material can be found using EDX of the material at comparable magnification (Figure 4-5). Here, with the contrast reversed to better view the platinum nanoparticles, small light patches, with a size of around 1 nm are evident. EDX shows significant counts of x-ray energy just below 10 KeV, indicative of platinum, at an energy where niobium and copper (other metals present on the material itself, or the TEM grid holder) do not appear. EDX of a line across two small light patches also indicates platinum present, with the platinum count increasing as the line passes through the two light patches evident in the image, again confirming the presence of platinum in the material.

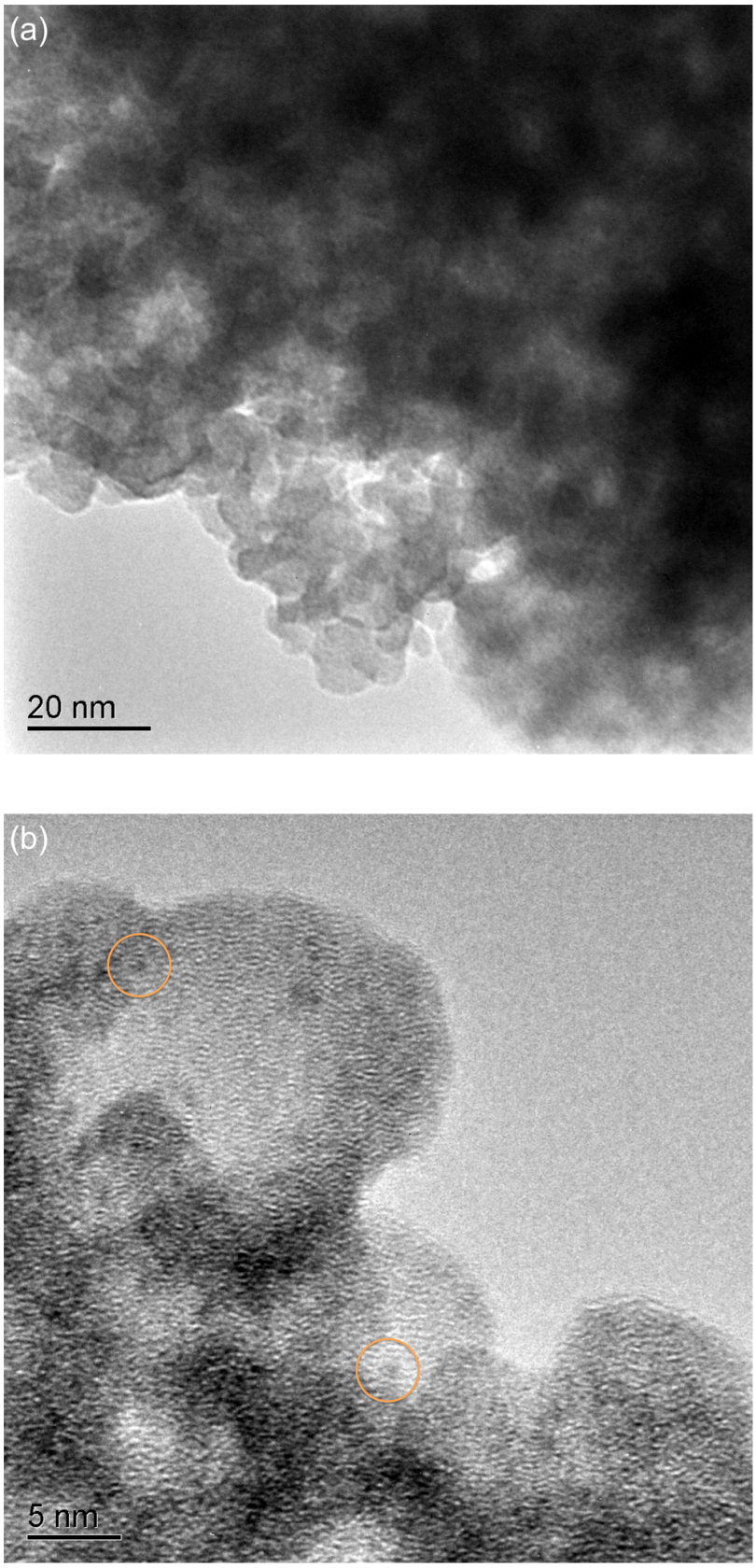


**Figure 4-4** (a) TEM image of **1Pt-$Nb_2O_5$** at 145 000 x magnification; (b) TEM image of **1Pt-$Nb_2O_5$** at 450,000 x magnification, with platinum nanoparticles highlighted (orange circles).

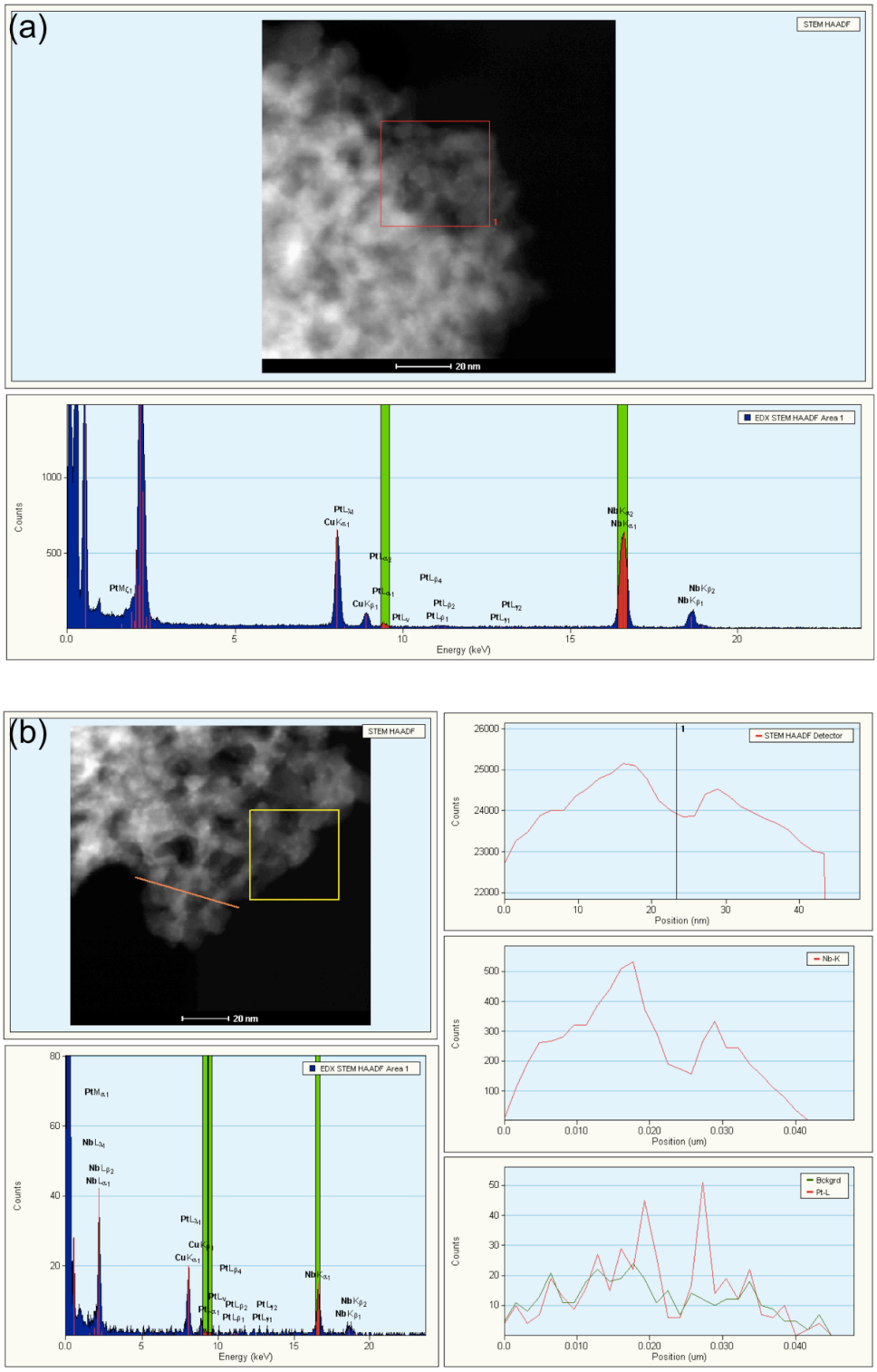


**Figure 4-5** (a) EDX data of an area of **1Pt-$Nb_2O_5$**, including a reverse contrast image, with counts at an energy of around 9 KeV indicative of platinum. (b) EDX data of an area of **1Pt-$Nb_2O_5$**, with data for a line crossing two areas identified as platinum nanoparticles, highlighting an increase in counts at around 9 KeV indicative of platinum when the line passes over the platinum areas.

Although platinum is not detected by XRD, both ICP and XPS shows platinum present, so the identification of platinum by EDX is no surprise. However the difficulty in identifying platinum particles from the images even at 1% by weight is indicative of the small size of the platinum nanoparticles on the surface of the $Nb_2O_5$; platinum particles shown to be platinum by EDX show a size of around 1 nm, confirming that the impregnation method produces nanoparticles of platinum at around 1 nm in size on the surface of the support.

1% by weight platinum on $Nb_2O_5$ was also synthesised by the photodeposition method (**6Pt-$Nb_2O_5$**), a comparatively simpler procedure of reducing a methanol / chloroplatinic acid / water solution under UV light with the semiconductor support. TEM images of **6Pt-$Nb_2O_5$** indicate that this photodeposition method produces significantly different platinum particles on the surface compared with the impregnation method used to produce **1Pt-$Nb_2O_5$**.

Figure 4-6 shows two dark particles over 100 nm wide, with EDX showing significant platinum content, indicating that this dark material is platinum metal. From this relatively low magnification, smaller dark particles are also evident, with EDX again showing platinum present, indicating that the photodeposition method produces significantly larger platinum nanoparticles compared with the impregnation method (Figure 4-7) Although TEM images identify only small areas of the particles under investigation, it is significant that the images processed for the impregnation method samples (**1Pt-$Nb_2O_5$**) show uniform 1 nm size particles, whereas the photodeposition method shows two size distributions of platinum particles. ICP analysis of **6Pt-$Nb_2O_5$** shows 0.90 % by weight platinum, comparable with the ICP analysis of **1Pt-$Nb_2O_5$** (0.94 % by weight platinum).

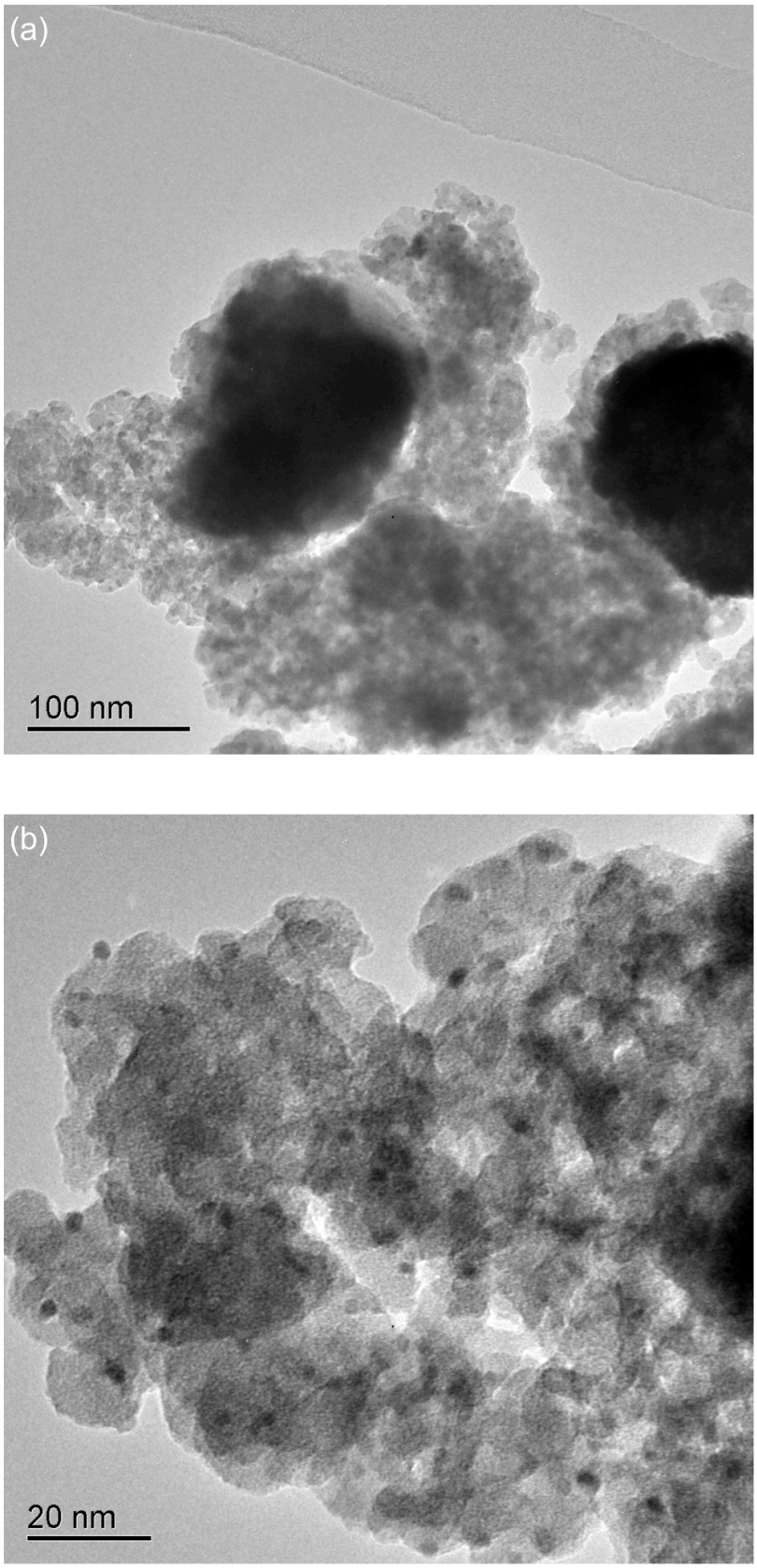


**Figure 4-6** (a) TEM image of **6Pt-$Nb_2O_5$** at 145,000 x magnification; (b) TEM image of **6Pt-$Nb_2O_5$** at 450,000 x magnification

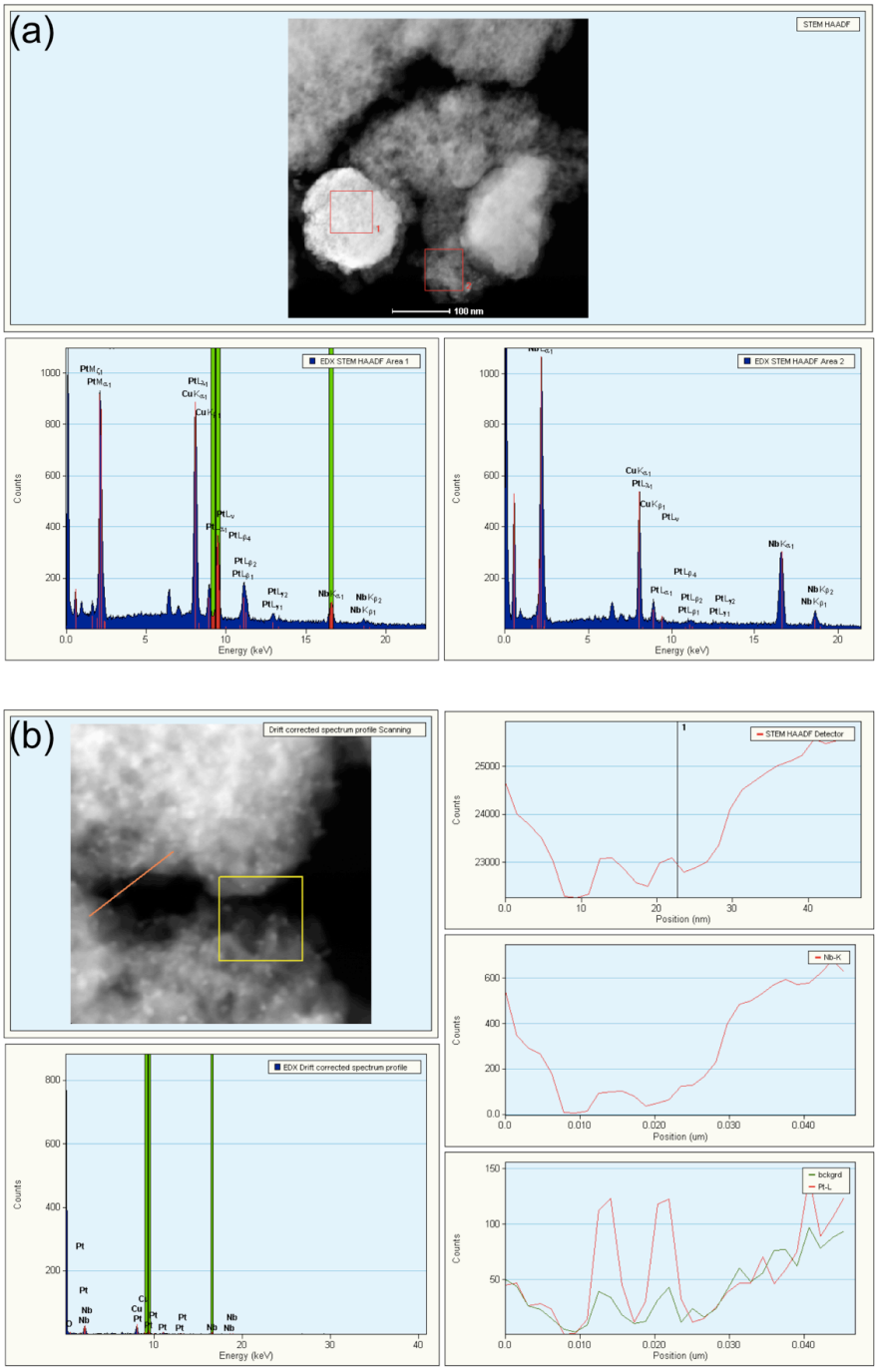


**Figure 4-7 EDX of Material** (a) EDX data of an area of **6Pt-$Nb_2O_5$**, including a reverse contrast image, with counts at an energy of around 9 KeV indicative of platinum emanating from the large bright particle identified as platinum. (b) EDX data of an area of **6Pt-$Nb_2O_5$**, with data for a line crossing two areas identified as platinum nanoparticles, highlighting an increase in counts at around 9 KeV indicative of platinum when the line passes over the platinum areas.

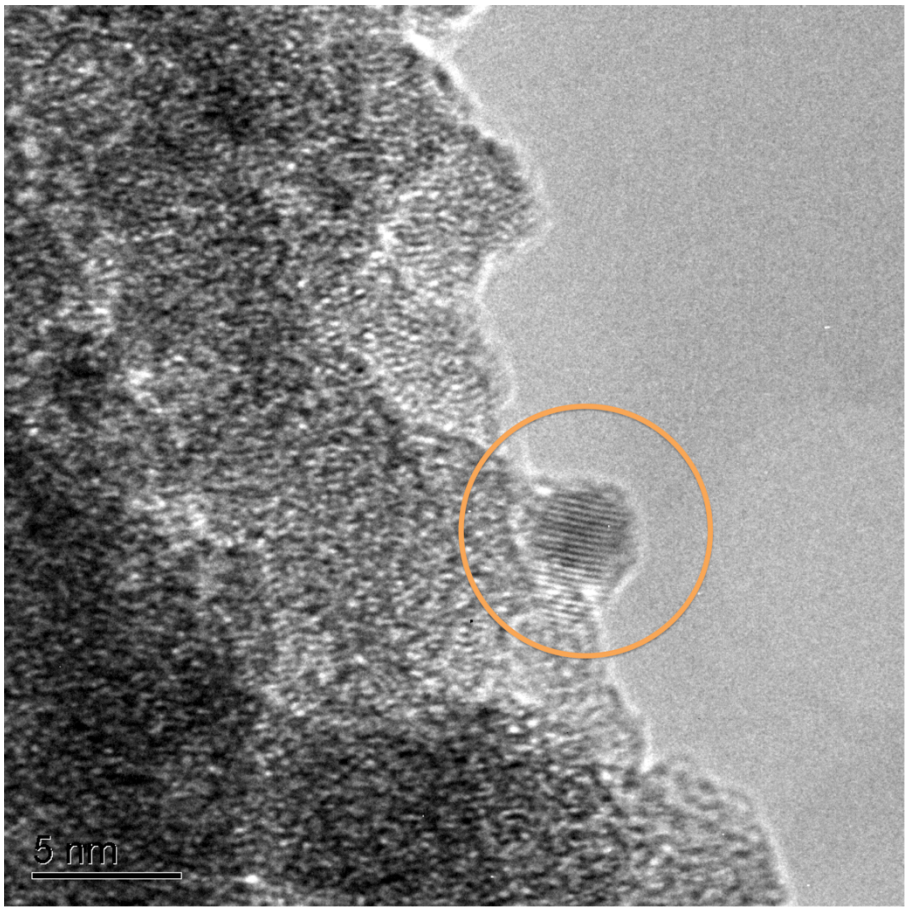


**Figure 4-8** TEM image of **6Pt-$Nb_2O_5$** at 590 000 x magnification, with the platinum particle highlighted

A higher magnification image shows the smaller of the two size platinum particles more clearly (Figure 4-8). From this image, the platinum nanoparticles can be seen to be between 3-5 nm in size. Also evident in is the crystalline nature of these platinum particles, with a layered pattern evident in the platinum particle highlighted, indicative of crystalline material, contrasting with the semi-amorphous niobium oxide support.

0.1% by weight palladium (**3Pd-$Nb_2O_5$**) was also investigated under the TEM. ICP analysis of this material indicated 0.11 % by weight palladium content. However images of the material at 145,000 and 590,000 x magnification failed to identify areas that could be considered palladium nanoparticles (Figure 4-10), despite ICP confirming the presence of palladium in the sample. EDX was similarly inconclusive (Figure 4-9), with no

palladium detected in the areas analyzed. This highlights a limitation in using TEM as a qualitative way of viewing such small palladium nanoparticles on a support such as niobium oxide.

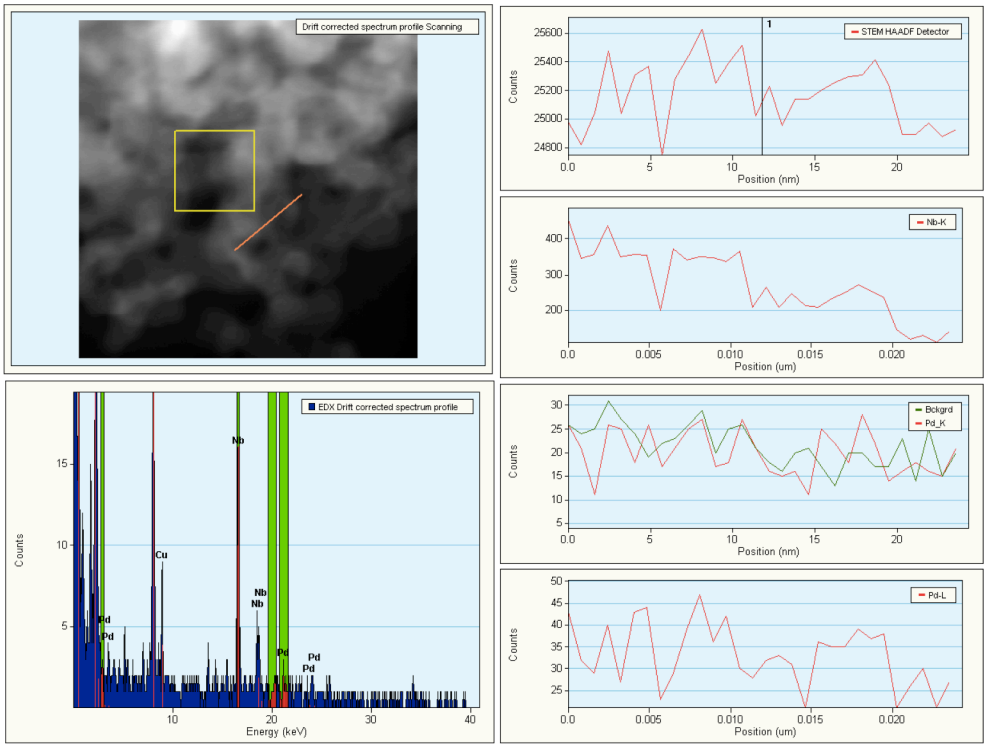


**Figure 4-9** EDX of **3Pd-$Nb_2O_5$**, showing no detectable Pd in the area selected.

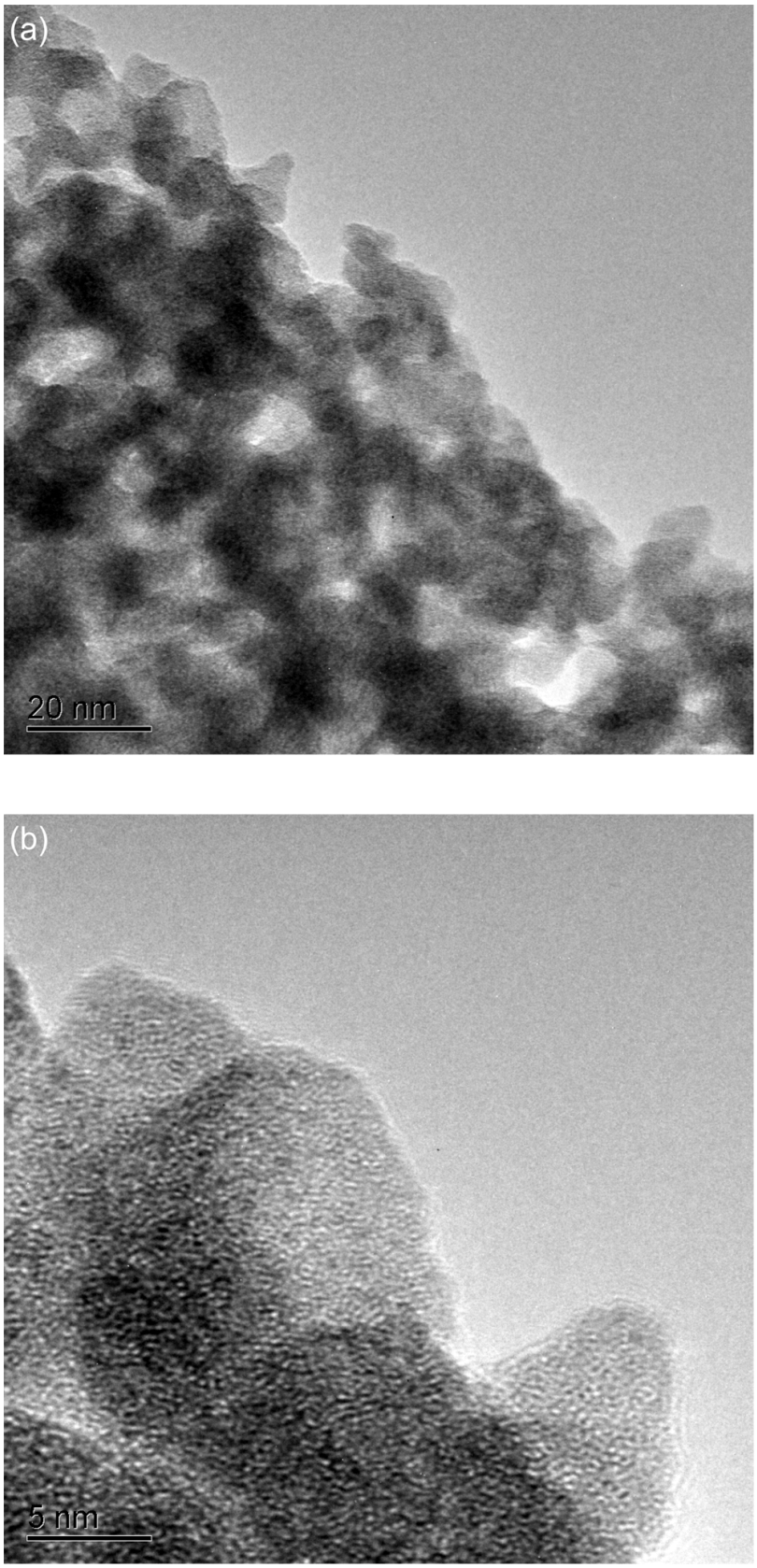


**Figure 4-10** TEM images of **3Pd-$Nb_2O_5$** at (a) 145,000 x magnification and (b) 590,000 x magnification.

Another quantitative way of analyzing the PGM content on the $Nb_2O_5$ is dispersion measurements. As described in Chapter 2, this technique uses carbon monoxide a way of determining the percentage of PGM that is able to be involved in catalysis taking place. Carbon monoxide (CO) is passed through the PGM added semiconductor, with the CO being adsorbed onto the surface of the PGM and the amount of CO adsorbed on the surface can be determined. By assuming that the CO adsorbs exclusively on the PGM in a 1:1 ratio of moles of CO to moles of PGM, the amount of moles of PGM on the surface accessible to the CO can be determined, i.e. the amount of PGM accessible in catalysis reactions. A percentage can be calculated of the amount of PGM able to adsorb the CO, over the amount of PGM in the sample, determined by ICP measurement. This dispersion – the fraction of the metal exposed – gives a quantitative way of determining how much of the PGM is available to be used in catalysis. Before being measured for dispersion, the sample is placed under reducing conditions, to ensure the PGM is in its reduced state i.e. the metal. Accurate dispersion measurements were measured for 1% and 0.5% PGM samples, and are listed in Table 4-2. Additionally, the dispersion measurement procedure was repeated without the reduction step, so the dispersion of the PGM supported material was measured as is.

The platinum impregnated samples, and the palladium impregnated samples show that the dispersion increases as the weight of PGM decreases. Interestingly, the dispersion of the impregnated platinum sample is almost double that of the photodeposited platinum sample at the same weight percentage. As seen in the TEM images of the two materials, the smaller size of the platinum nanoparticles on **1Pt-$Nb_2O_5$** gives better dispersion than the larger and less uniform platinum particles on the surface of **6Pt-$Nb_2O_5$**.

| Material | Code | CO adsorbed / μmol $g^{-1}$ | Dispersion / % |
|---|---|---|---|
| 1%Pt-$Nb_2O_5$ | 1Pt-$Nb_2O_5$ | 13 | 25 |
| 1%Pt-$Nb_2O_5$ (no reduction step) | 1Pt-$Nb_2O_5$ | | 17.7 |
| 0.5%Pt-$Nb_2O_5$ | 2Pt-$Nb_2O_5$ | 9.8 | 38 |
| | | | |
| 1%Rh-$Nb_2O_5$ | 1Rh-$Nb_2O_5$ | 18.3 | 20 |
| 1%Rh-$Nb_2O_5$ (no reduction step) | 1Rh-$Nb_2O_5$ | | 0.7 |
| 0.5%Rh-$Nb_2O_5$ | 2Rh-$Nb_2O_5$ | 7.9 | 18 |
| | | | |
| 1%Pd-$Nb_2O_5$ | 1Pd-$Nb_2O_5$ | 12.5 | 13 |
| 1%Pd-$Nb_2O_5$ (no reduction step) | 1Pd-$Nb_2O_5$ | | 4 |
| 0.5%Pd- $Nb_2O_5$ | 2Pd-$Nb_2O_5$ | 11.8 | 25 |

**Table 4-2** Summary of the dispersion measurements carried out on 1% and 0.5% PGM added $Nb_2O_5$ samples, including experiment carried out without the pre-measurement reduction step.

Significantly, in all three metals, the dispersion is higher when the material undergoes a reduction step in the dispersion measurement procedure. This indicates there could be some oxide present, although the amount of this is too small to measure by XPS, which indicates 100% metal content of rhodium and platinum. For **1Rh-$Nb_2O_5$**, almost no CO is adsorbed onto the rhodium present in the sample, possibly due to the reactive metal being coated with an oxide layer, whilst not being detectable by XPS, able to stop the CO absorbing onto the surface. An alternative explanation could be chemisorbed species attached to the reactive rhodium metal preventing the CO from adsorbing.

By using XPS, TEM, ICP and dispersion measurements, the higher weight percentage PGM samples have been well characterised. However the difficulty of characterising low weight PGM samples presents a challenge. ICP is not sensitive enough to accurately determine the low weight percentage 0.01% samples; as described in Chapter 2, adapting

TPR equipment to accurately measure low weight percentage PGMs is challenging, whilst it is difficult to see the PGM on low weight percentage PGM supported semiconductors, with EDX similarly unable to detect such low weight percentage PGMs. However, all material was tested for hydrogen generation with sacrificial reagents.

## 4.3 Hydrogen Measurements

In order to compare the 3 PGM added materials, with different weight percentages with respect to photocatalytic hydrogen generation, each material was reacted under the protocol described in Chapter 2: a 20% methanol solution under UV light for 4 hours.

### 4.3.1 $Nb_2O_5$ Hydrogen Generation

As discussed in Chapter 3, $Nb_2O_5$ has been studied as a photocatalyst with respect to hydrogen generation. Compared to $TiO_2$, $Nb_2O_5$ has a larger band gap, which also implies that the conduction band reduction potential of $Nb_2O_5$ is more negative than $TiO_2$, signifying greater reductive power. Ohtani suggested that because of this, $Nb_2O_5$ made by his hydrothermal method would be able to generate hydrogen from a methanol solution without the need of PGMs; his paper proved this to be the case, with around 18 μmol $h^{-1}$ of hydrogen being generated, whereas $TiO_2$ produced negligible hydrogen.[13]

For the material synthesised in Chapter 3, a comparable experiment was performed, using the hydrogen generation protocol described in Chapter 2. 0.1 g of **$Nb_2O_5$-B2:500** was added to 100 ml of a 20% methanol solution, and reacted under UV light for 4 hours. $TiO_2$ (P25) was similarly reacted under UV light. The data shows that **$Nb_2O_5$-B2:500** produces around 4 μmol $h^{-1}$ of hydrogen, compared to the less than 1 μmol $h^{-1}$ hydrogen generated by P25, the most active form of $TiO_2$. Although the surface area of **$Nb_2O_5$-B2:500** is higher than P25, normalizing to unit surface area shows that the **$Nb_2O_5$-B2:500** is superior in photocatalytic activity for generating hydrogen compared to P25 (0.20 μmol $h^{-1}$ $m^{-2}$ vs

0.36 μmol $h^{-1}$ $m^{-2}$ for P25 and **$Nb_2O_5$-B2:500** respectively). As noted, the more negative conduction band, with greater reducing power is key to this superior activity.

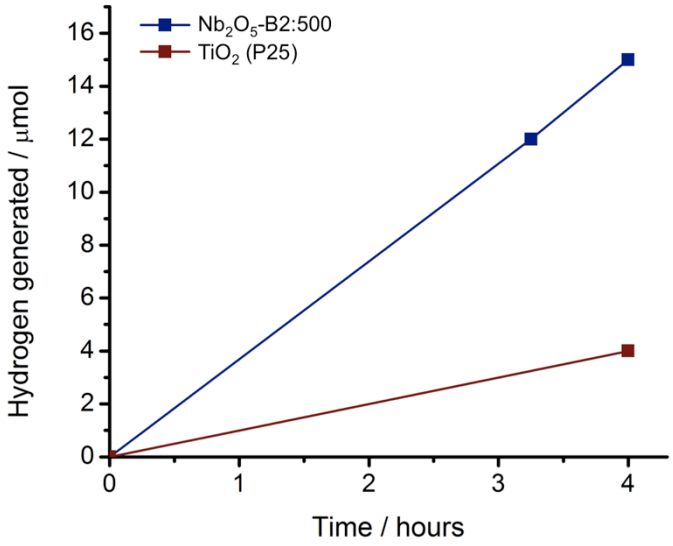


**Figure 4-11** Reaction of **$Nb_2O_5$-B2:500**, and P25 with a 20% methanol solution under UV Light, illustrating hydrogen evolved during the course of the reaction.

## 4.3.2 Platinum Added $Nb_2O_5$ Hydrogen Generation

A summary of the results of the platinum based $Nb_2O_5$ material reacting with methanol solution under UV light is given in Figure 4-12. The reaction with **3Pt-$Nb_2O_5$** was also repeated (Figure 4-13): after 4 hours, the reactor was exposed to air, then sealed, again, before being purged with nitrogen, and reacted again under the same UV light conditions; the results show that the two runs give comparable rates of hydrogen generation.

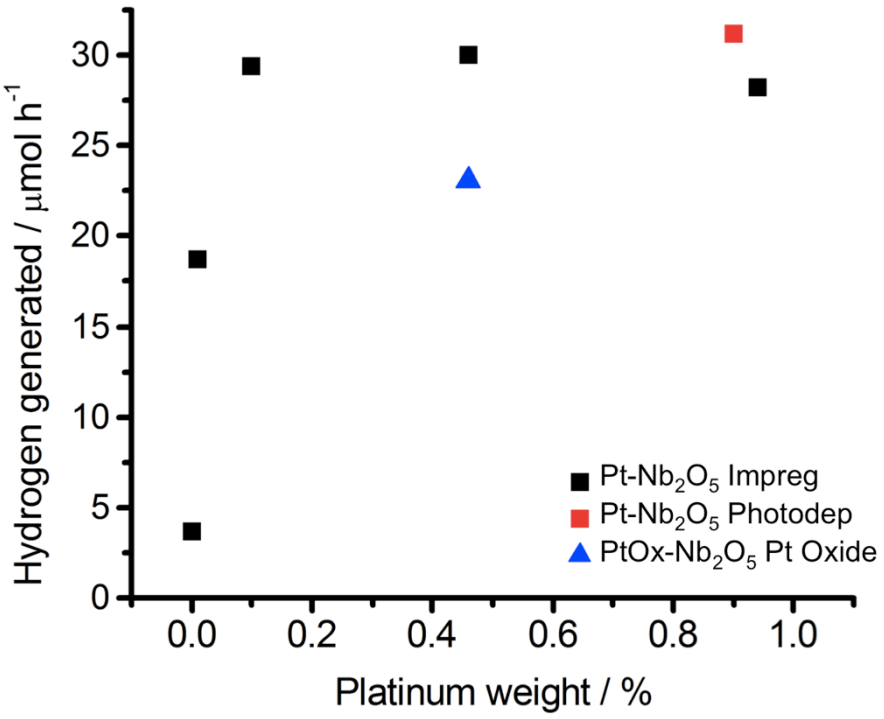


**Figure 4-12** A summary of the hydrogen generation experiments for platinum added $Nb_2O_5$ material.

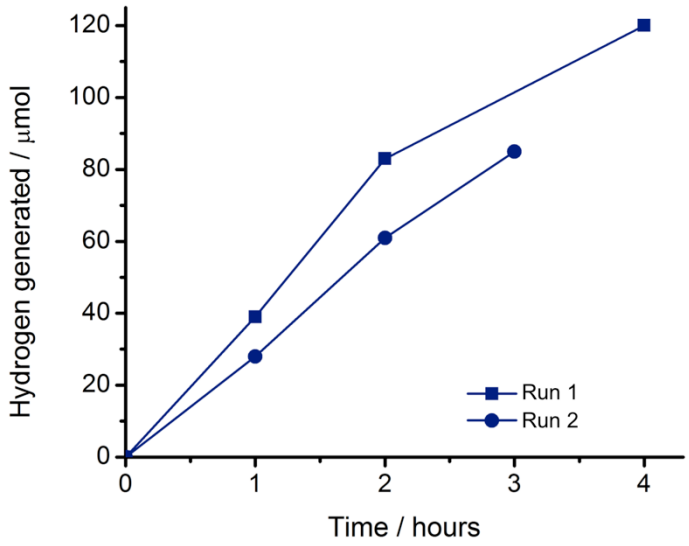


**Figure 4-13** Reaction of **3Pt-$Nb_2O_5$** with 20% methanol solution under UV light, illustrating the hydrogen evolved during the course of two reactions with the same material.

A comparison between **1Pt-$Nb_2O_5$**, **2Pt-$Nb_2O_5$**, **3Pt-$Nb_2O_5$** (1 – 0.1% impregnated platinum samples) and **6Pt-$Nb_2O_5$** (photodeposited sample) shows that there is little difference in hydrogen generation rate, with the hydrogen generation rate centering on 30 μmol $h^{-1}$ (Figure 4-12). Despite the significant difference in the platinum nanoparticles of **1Pt-$Nb_2O_5$**, with 1% by weight platinum deposited by impregnation and **6Pt-$Nb_2O_5$**, with 1% by weight platinum deposited by photodeposition, evident in the dispersion and TEM images of these compounds, the rate is comparable. This is slightly surprising; one would assume more disperse discrete platinum would provide more active sites for hydrogen generation. Similarly surprising is the comparable hydrogen generation of **3Pt-$Nb_2O_5$**, **2Pt-$Nb_2O_5$** and **1Pt-$Nb_2O_5$**, with 0.1% 0.5% and 1% platinum added by impregnation respectively. However the higher dispersion of **2Pt-$Nb_2O_5$** indicates that a higher percentage of the lower weight platinum can be accessed, and so is able to provide active sites for hydrogen generation. By assuming the lower platinum weight **3Pt-$Nb_2O_5$** has comparable higher dispersion, the result of this low weight still generating significant amounts of hydrogen is consistent with Ohtani's observation of a single particle of platinum required per particle of semiconductor.[6]

Also plotted in Figure 4-12 are the hydrogen generation results for **2Pt-$Nb_2O_5$-A**, material that did not undergo the reduction step when undergoing platinum addition. XPS showed this material to be a mixture of platinum oxides, with no metallic platinum present. The data confirms that this material can generate hydrogen, significantly more than the unpromoted **$Nb_2O_5$-B2:500**. An explanation for this could be that the platinum oxide present on the surface of the $Nb_2O_5$ is being reduced by the electrons produced by $Nb_2O_5$ on activation with UV light, comparable to the photodeposition reaction. Visibly, this is confirmed by the darkening of the material after the reaction is complete. The lack of an induction time of this **2Pt-$Nb_2O_5$-A** reaction possibly indicates that the platinum oxide is reduced to the metal as soon as the light is turned on.

### 4.3.3 Rhodium Added $Nb_2O_5$ Hydrogen Generation

A summary of the results is given in Figure 4-14. Unlike the platinum added material, rhodium added material shows significant differences between the different weight percentages. Significantly, the material that gives the most hydrogen is **3Rh-$Nb_2O_5$**, with 0.1% rhodium added by impregnation, with this material generating a rate of hydrogen over twice that of **1Rh-$Nb_2O_5$**, despite having 10 times less rhodium present, confirmed by ICP measurements. This indicates that the interaction between the $Nb_2O_5$/rhodium and the water being reduced to form hydrogen is different from the $Nb_2O_5$/platinum system.

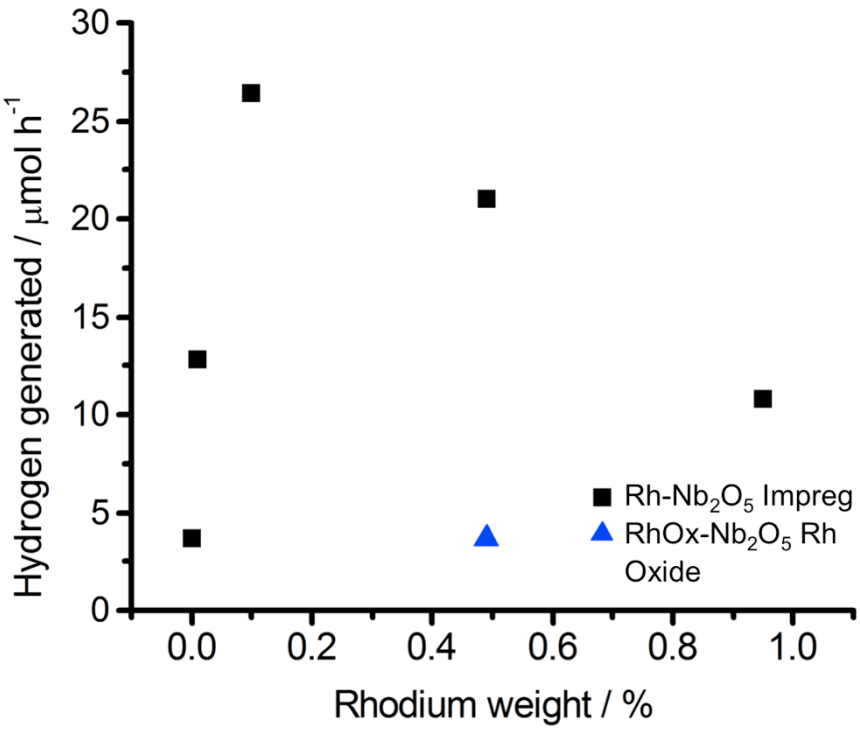


**Figure 4-14** A summary of the hydrogen generation experiments for rhodium added $Nb_2O_5$ material.

Unlike the platinum added equivalent material (**1Pt-$Nb_2O_5$**), **1Rh-$Nb_2O_5$** has an induction period, where the rate of hydrogen generation is less compared to later on in the reaction, where the reaction rate is significantly higher (Figure 4-15). A repeated reaction shows a

comparable result. Dispersion measurements signified that the rhodium on $Nb_2O_5$ had to undergo a reduction step before being available to adsorb CO as part of the dispersion measurement process; this induction period provides further proof that rhodium on the as made material is not immediately available for hydrogen generation sites, however the rhodium sites do become available as the reaction proceeds.

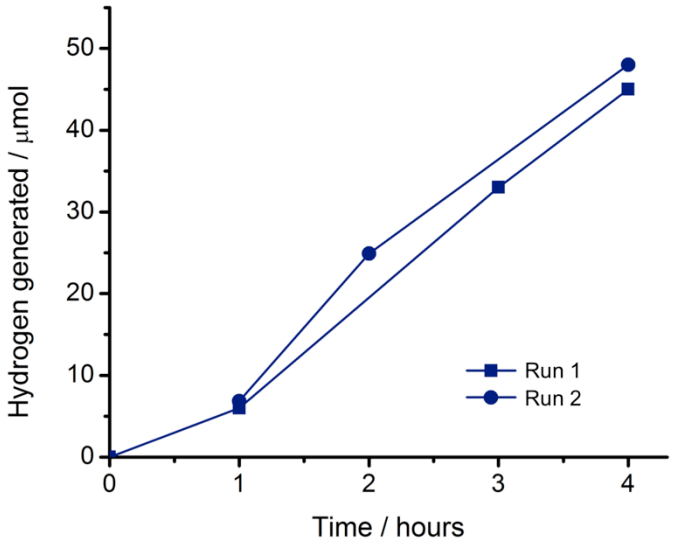


**Figure 4-15** Reaction of **1Rh-$Nb_2O_5$** with 20% methanol solution under UV light, illustrating the hydrogen evolved during the course of two reactions carried out under the same conditions independently.

Another interesting result from the data is the lack of improvement in hydrogen generation from **$Nb_2O_5$-B2:500** to **2Rh-$Nb_2O_5$-A**, the pre reduction 0.5% by weight rhodium sample: the hydrogen generation rates are identical. XPS confirms the rhodium present in this material to be mixed oxide rhodium species, with no metal present. Unlike the comparable platinum added $Nb_2O_5$ (**2Pt-$Nb_2O_5$-A**) the rhodium oxide species are not reduced to metal via a light induced reaction with $Nb_2O_5$. This result also implies the initial induction period noted from the **1Rh-$Nb_2O_5$** reaction, and confirmed by the dispersion measurements of **1Rh-$Nb_2O_5$** without a pre-treatment reduction step, could be due chemisorbed species which desorb when the reaction starts, or under flow from hydrogen in dispersion

measurements, rather than a more permanent oxide species, which reduces when under UV light or hydrogen flow.

### 4.3.4 Palladium Added $Nb_2O_5$ Hydrogen Generation

A summary of results is given in Figure 4-16. As with rhodium added material, the rate of hydrogen generated increases from 1% by weight palladium through to 0.1%, with 0.1% by weight palladium (**3Pd-$Nb_2O_5$**) having the highest rate of hydrogen generation, although the difference in rate between the different weight percentage material is not as pronounced as in rhodium added material.

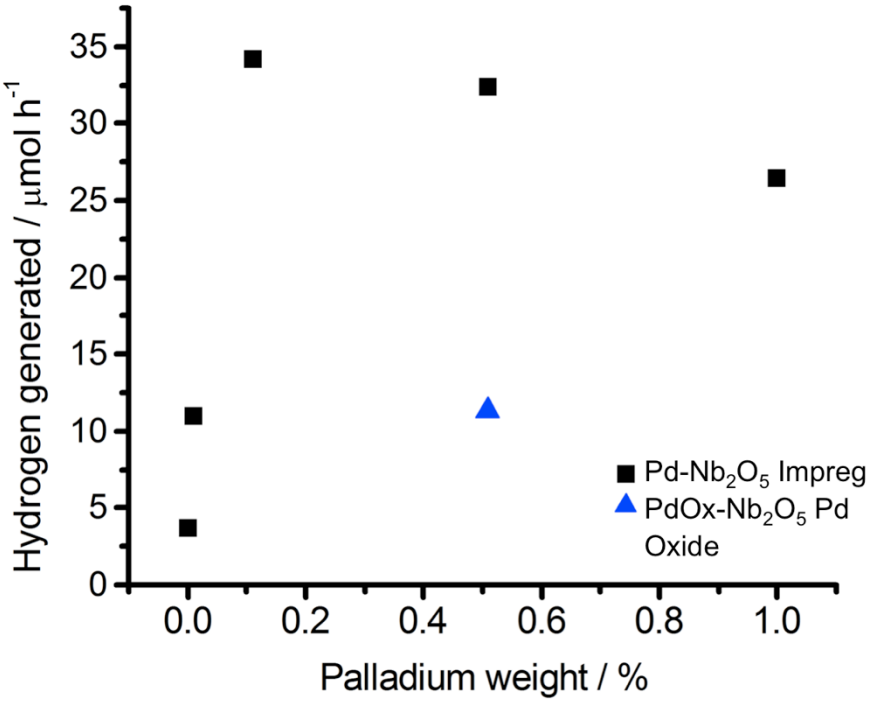


**Figure 4-16 (previous page)** A summary of the hydrogen generation experiments for palladium added $Nb_2O_5$ material.

A longer-term hydrogen generation reaction was also carried out with **3Pd-$Nb_2O_5$** (Figure 4-17). The material was reacted under UV light for over 20 hours, generating 521 µmol of hydrogen. Based on the amount of $Nb_2O_5$ present, at this stage in the reaction there is a

turnover number of 1.16, indicating that the reaction is catalytic. There is also no evidence of the reaction rate slowing down. XRD of material before and after the long-term reaction, (Figure 4-18), in addition to SEM of the material before and after the long-term reaction (Figure 4-19), show comparable properties, again supporting the view that this is a catalytic reaction.

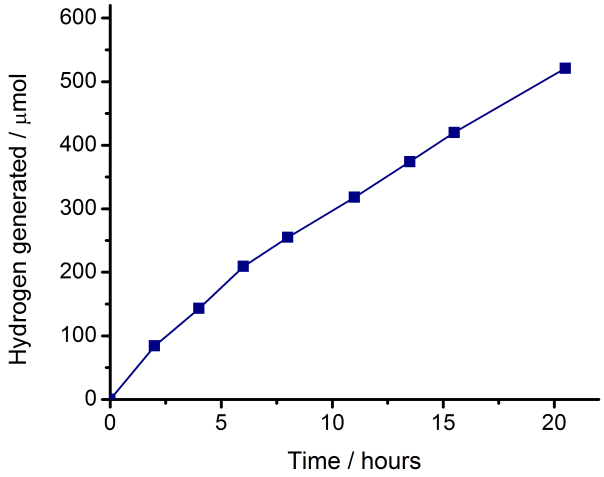


**Figure 4-17** Reaction of **3Pd-$Nb_2O_5$** with 20% methanol solution under UV light, illustrating the hydrogen evolved during the course of the reaction over 22 hours.

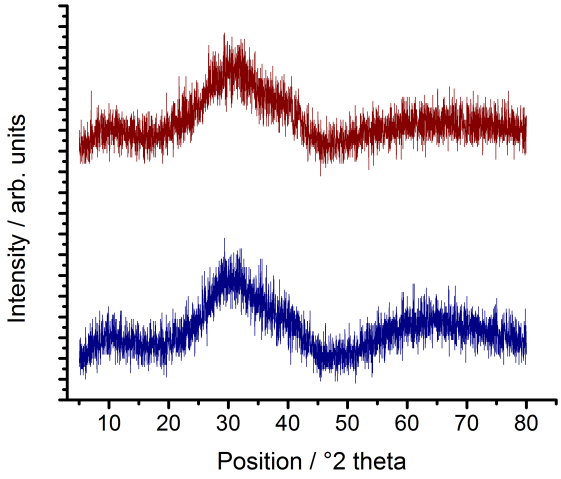


**Figure 4-18** XRD spectrum of **3Pd-$Nb_2O_5$** before (blue) and after (red) the long term hydrogen generation reaction under UV light

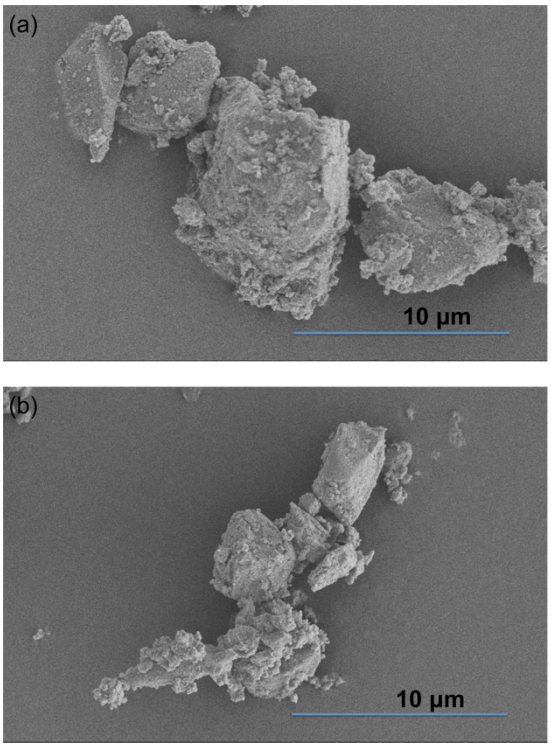


**Figure 4-19** SEM images at 5000 x magnification of **3Pd-$Nb_2O_5$** before (a) and after (b) the long term hydrogen generation reaction under UV light

## 4.3.5 Addition of two co-catalysts ($RuO_2$ and Pt)

Whilst this chapter predominantly deals with hydrogen generation co-catalysts, the alternative oxygen generation co-catalyst, $RuO_2$ was briefly investigated. The aim of synthesising material was to see whether Pt-$Nb_2O_5$-$RuO_2$ material would be able to split pure water. A major problem with this type of reaction is the separation of hydrogen and oxygen, limiting the backward reaction to form water. It is noted that platinum or the semiconductor can actually act as promoters for this back reaction.[4]

The **Pt-$Nb_2O_5$-$RuO_2$** was synthesised by a method comparable to Gratzel's work described in the introduction to this chapter, where the group synthesized Pt-$TiO_2$-$RuO_2$ by firstly adding the $RuO_2$, then photodepositing platinum onto the $TiO_2$-$RuO_2$.[14-15] Here, $RuO_2$ was loaded onto **$Nb_2O_5$-B2:500** by an impregnation method, with 1% by weight ruthenium chloride ($RuCl_3$). The material was calcined in air for 2 hours at 500 °C. This

material **$Nb_2O_5$-$RuO_2$**, was then photodeposited with platinum by the photodeposition method previously described, with 1% by weight platinum added to the material: **Pt-$Nb_2O_5$-$RuO_2$**.

Both **$Nb_2O_5$-$RuO_2$** and **Pt-$Nb_2O_5$-$RuO_2$** were tested with 20 % methanol solution under UV light, comparable to the reaction carried out with the PGM added material described earlier in this chapter. This was compared to **6Pt-$Nb_2O_5$**, material photodeposited with 1% by weight platinum, and with the unpromoted **$Nb_2O_5$-B2:500**. The results surprisingly show that the most effective catalyst in terms of rate is **6Pt-$Nb_2O_5$**, rather than the material with the hydrogen and oxidation co-catalysts. The results also show that adding an oxidation co-catalyst improves the reaction rate of the hydrogen generation reaction (a reduction reaction), as seen by the increase in hydrogen generated with **$Nb_2O_5$-$RuO_2$** compared with unpromoted **$Nb_2O_5$-B2:500**.

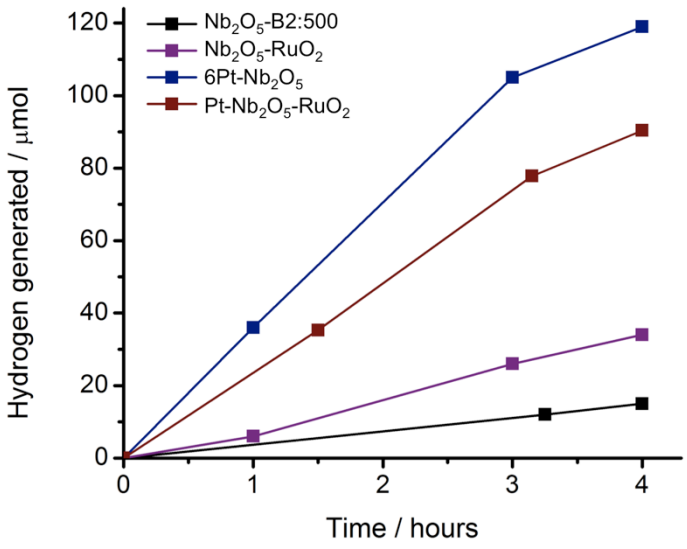


**Figure 4-20** Reaction of **$Nb_2O_5$-B2:500**, **$Nb_2O_5$-$RuO_2$**, **6Pt-$Nb_2O_5$** and **Pt-$Nb_2O_5$-$RuO_2$** with 20% methanol solution under UV light, illustrating the hydrogen evolved during the course of the reaction.

It is clear from the results in this chapter that varying the method of deposition and weight percentage of PGM has a large bearing on the photocatalytic activity of the material synthesised, and so further optimization of the two co-catalysts in terms of weight percentage and element for the reduction co-catalyst (platinum, rhodium or palladium) and weight percentage of the oxidation co-catalyst is required.

With **Pt-$Nb_2O_5$-$RuO_2$** performing relatively poorly as a photocatalyst compared to some of the other material synthesized, it is perhaps not surprising that the material was unable to split water under UV light after 8 hours, with no hydrogen detected. Further optimization of the co-catalysts on $Nb_2O_5$ will give more photocatalytic activity for the material, and so give a better chance of producing detectable amounts of hydrogen and oxygen from the water splitting reaction.

## 4.4 Conclusion and Future Work

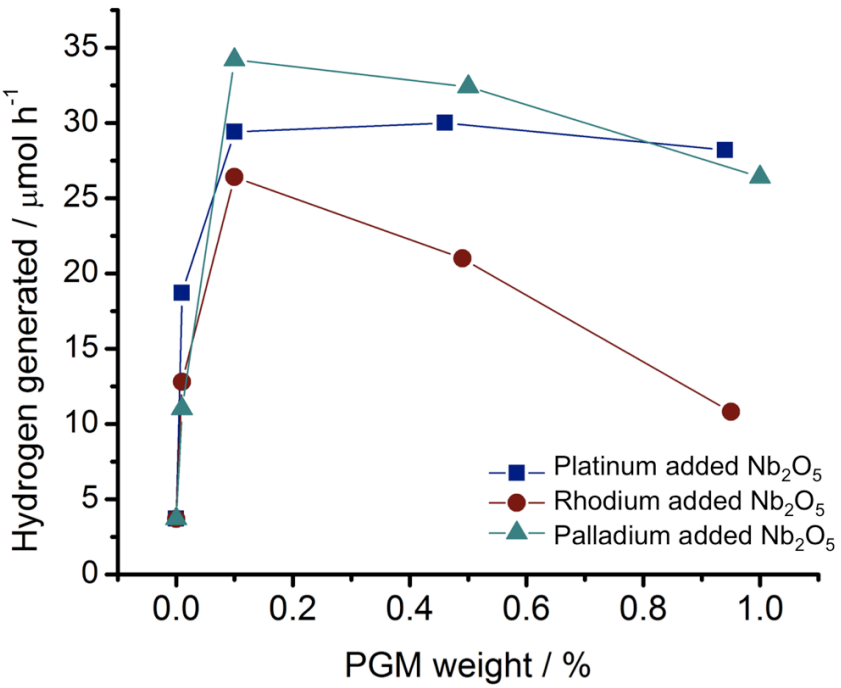


**Figure 4-21** A summary of the hydrogen generation results for the impregnation samples synthesised by addition of platinum, rhodium and palladium to $Nb_2O_5$.

A summary of the impregnation results is illustrated in Figure 4-21. The data shows that the best material synthesised in terms of hydrogen generation is the 0.1% by weight palladium $Nb_2O_5$ sample, although the three PGM based materials follow a general trend that lower weight PGMs up to 0.1% give better photocatalytic performance. Unfortunately, two key instruments of characterisation: TEM and dispersion analysis are limited when characterising such low weight percentage PGM added material. TEM, even at high resolution is unable to pick out the individual nanoparticles of palladium at such low weight percentages even at high resolution, although one could conclude that the fact the palladium nanoparticles cannot be imaged is indicative of high dispersion. Equipment for measuring dispersion is limited in producing such a low pulse of CO required to interpret such a small amount of CO adsorbed onto the palladium.

Despite this lack of characterisation on the low weight PGM added samples, the results from this chapter have contributed a great deal of knowledge of PGM addition, with characterisation techniques such as dispersion rarely seen in literature. The results, and the direction of similarly investigating oxidation based PGM material give scope for synthesising an effective catalyst for water splitting.

## 4.5 References

[1] A. Fujishima, K. Honda, *Nature* **1972**, *238*, 37-38.

[2] L. S. Al-Mazroai, M. Bowker, P. Davies, A. Dickinson, J. Greaves, D. James, L. Millard, *Catal. Today* **2007**, *122*, 46-50.

[3] S. Sato, J. M. White, *Chem. Phys. Lett.* **1980**, *72*, 83-86.

[4] K. Yamaguti, S. Sato, *J. Chem. Soc., Faraday Trans. 1 F* **1985**, *81*, 1237-1246.

[5] F. E. Osterloh, *Chem. Mater.* **2008**, *20*, 35-54.

[6] B. Ohtani, K. Iwai, S.-i. Nishimoto, S. Sato, *J. Phys. Chem. B* **1997**, *101*, 3349-3359.

[7] A. Dickinson, D. James, N. Perkins, T. Cassidy, M. Bowker, *J. Mol. Catal. A: Chem.* **1999**, *146*, 211-221.

[8] L. Millard, M. Bowker, *J. Photochem. Photobiol., A* **2002**, *148*, 91-95.

[9] A. Mills, S. LeHunte, *J. Photochem. Photobiol., A* **1997**, *108*, 1-35.

[10] Y. Matsumoto, *J. Solid State Chem.* **1996**, *126*, 227-234.

[11] B. Kraeutler, A. J. Bard, *JACS* **1978**, *100*, 4317-4318.

[12] Y.-C. Xie, Y.-Q. Tang, *Advances in Catalysis* **1990**, *37*, 1-43.

[13] H. Kominami, K. Oki, M. Kohno, S. Onoue, Y. Kera, B. Ohtani, *J. Mater. Chem.* **2001**, *11*, 604-609.

[14] D. Duonghong, E. Borgarello, M. Gratzel, *JACS* **1981**, *103*, 4685-4690.

[15] E. Borgarello, J. Kiwi, E. Pelizzetti, M. Visca, M. Gratzel, *JACS* **1981**, *103*, 6324-6329.

# 5 Chromium – Niobium Based Composites

## 5.1 Introduction

The idea of using metal-to-metal charge transfer chromophores for visible light photocatalysis was introduced initially by Heinz Frei and his group, via a series of papers published from 2005.[1-7] Unlike ligand to metal charge transfer on microporous silica based sieves, for example Ulagappan and Frei's oxygen to titanium charge transfer,[8] where the transition is in the ultraviolet region, oxo-bridged metal-to-metal charge transfer (MMCT) moieties can absorb visible light. Based on work by George Blasse,[9] Frei and his group postulated that two metal centres could be engaged on a single particle; these would be able to absorb visible light, allowing an electron to be transferred from one metal centre to the other, thus producing charge carriers capable of oxidizing or reducing material.

Lin and Frei[1] synthesised binuclear metal-to-metal charge transfer moieties by grafting titanium (IV) onto the surface of a MCM-41 silicate sieve, and grafting either copper (I) or tin (II). This produced in the case of titanium (IV) and copper (I) a visible light absorbing Ti(IV)-O-Cu(I) chromophore. A key characterisation of this material was the difference between the diffuse reflectance of the MCM-41-Cu(I) material synthesised, showing UV absorption producing a $3d^{10} \rightarrow 3d^{9}4s^{1}$ transition, and the diffuse reflectance of the MCM-41-Ti(IV)-O-Cu(I) material, which showed visible light absorption not present in the MCM-41-Cu(I) material, with the group attributing this to the $Ti^{IV}/Cu^{I} \rightarrow Ti^{III}/Cu^{II}$ MMCT transition (Figure 5-1(a)). The MCM-41-Ti(IV)-O-Sn(II) material was characterised similarly, with the visible absorbance from the diffuse reflectance attributed to $Ti^{IV}/Sn^{II} \rightarrow Ti^{III}/Sn^{III}$ MMCT. Although no photocatalysis reactions were carried out with the material synthesised in this paper, the group published around the same time a paper where they synthesised comparable material utilizing a Zr(IV)-O-Cu(I) chromophore.[2] Using this

material under visible light, the group successfully photoreduced carbon dioxide to carbon monoxide and oxygen, an important reaction for the generation of renewable fuels using light as an energy source. The Frei group noted that they were unable to photoreduce carbon dioxide with the Ti/Cu based material, with the group attributing this to the poor reductive power of $Ti^{III}$ compared with $Zr^{III}$.

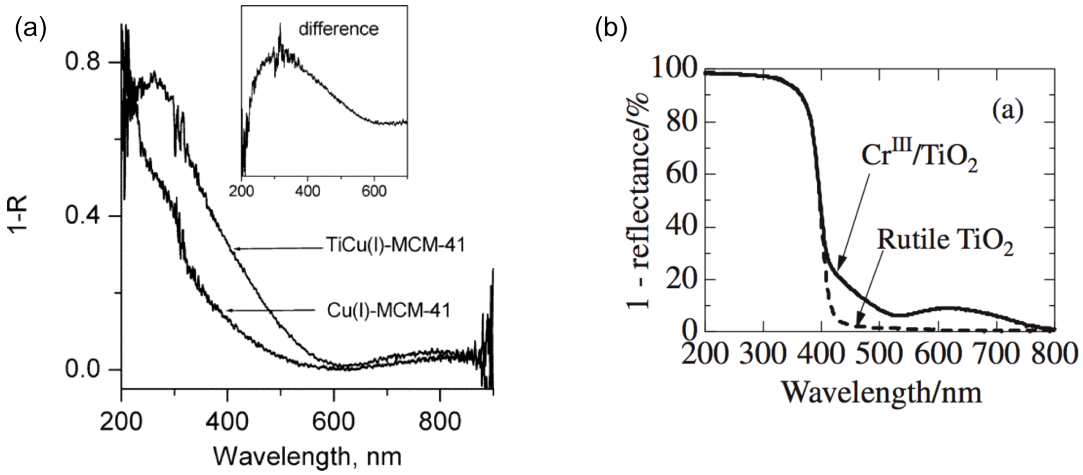


**Figure 5-1** (a) The diffuse reflectance of the MCM-41-Cu(I) material and MCM-41-Ti(IV)-O-Cu(I) material synthesised by Lin and Frei,[1] the insert shows the difference between the two spectra. (b) The diffuse reflectance of rutile and $Cr^{III}/TiO_2$ material synthesised by Irie et al.[10] Figures acquired from the manuscripts.

Another group led by Kazuhito Hashimoto in 2008 produced material by an analogous method.[10] Here, Irie et al. grafted chromium (III) ions onto the surface of rutile titanium dioxide by an impregnation method, dispersing rutile titanium dioxide in chromium (III) chloride solution, heating at 90 °C for one hour, then filtering and drying the powder at 110 °C for 24 hours. By comparison the group also grafted chromium (III) ions onto zirconium oxide. The authors state that the chromium (III) is not chemically bonded to titanium dioxide, and describe the MMCT as proceeding via space charge transfer. As with the Frei papers, the group compared the diffuse reflectance of the material pre and post grafting, noting the visible absorbance in the grafted material not present in the original rutile titanium dioxide, which in this case was attributed to both MMCT and chromium

(III) *d* – *d* transitions (Figure 5-1(b)). The group chose the particular ions chromium (III) and titanium (IV) due to the $Cr^{IV}/Cr^{III}$ redox couple ($E^0$ = 2.1 V), and the conduction band of rutile (–0.4 V at pH 7); they concluded that visible light (with energy less than 3.0 eV) should have enough energy to induce the transition from chromium to titanium, being greater than the difference between the redox couple of $Cr^{IV}/Cr^{III}$ and the conduction band of rutile. With the zirconium oxide conduction band being higher in energy than titanium oxide (at –1.4 V at pH 7), the energy of light needed to produce a chromium to zirconium transition was higher than the corresponding chromium to titanium transition, but still less than the zirconium oxide band gap, this further confirmed the MMCT taking place. The chromium – titanium based material was successfully used to decompose 2-propanol into acetone and carbon dioxide under visible light.

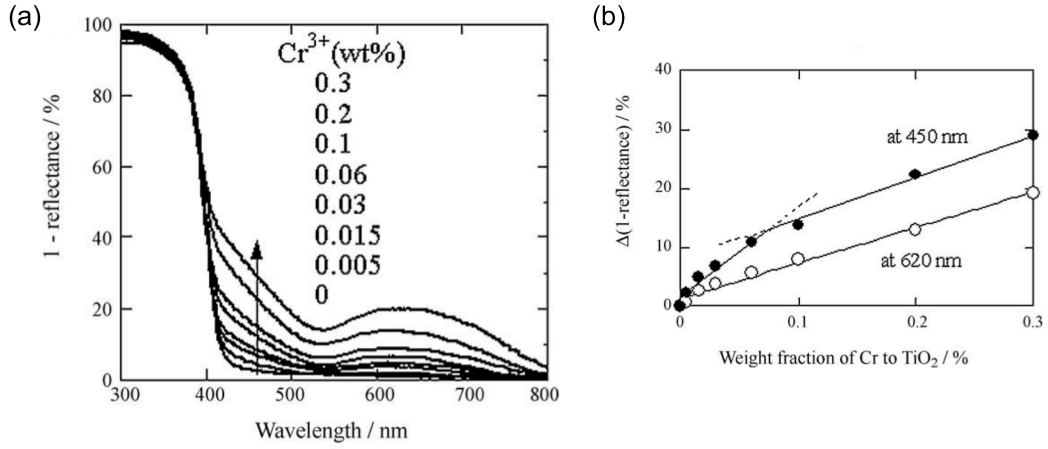


**Figure 5-2** (a) Material synthesised by Hashimoto et al.,[10-11] highlighting the increase in charge transfer absorbance at (450 nm) and chromium *d* – *d* transitions (at 650 nm) with increasing amount of chromium impregnated. (b) The change in reflectance versus the amount of chromium impregnated at 450 nm and 620 nm. Figures acquired from the manuscript.[11]

The group continued characterisation of the material by grafting different weight percentages of chromium.[11] The group found the absorbance at 620 nm, which the group attributed to chromium (III) *d* – *d* transitions, increased linearly with the amount of chromium grafted (Figure 5-2(a)). The absorbance at 450 nm, increased sharply when the

amount of chromium (III) was less than 0.06% by weight, then linearly, comparable to the 620 nm *d* – *d* transition at higher weight percentages. The group attributed this peak to both the chromium – titanium MMCT and chromium (III) *d* – *d* transitions, with the higher weight percentage chromium based material absorption being dominated by the chromium (III) *d* – *d* transitions, and the lower weight percentage material chromium being well dispersed, producing a more dominant chromium – titanium charge transfer transition (Figure 5-2(b)). The group concludes that not all the chromium (III) is involved in the MMCT, and so there is an optimal level of chromium (III) that can be used to induce MMCT, which one could conclude would be complete coverage of a monolayer of chromium (III) oxide on the surface of the titanium dioxide.

In this chapter, material was designed to replicate the MMCT process described by the Frei and Hashimoto groups, to induce visible light photocatalysis. Unlike the grafted ions used by the both the Frei and Hashimoto groups, material synthesised in this chapter used an incipient wetness technique to load a metal oxide onto a metal oxide.[12] Niobium oxide ($Nb_2O_5$), the synthesis and characterisation of which is described in Chapter 3 of this thesis (**$Nb_2O_5$-B1:500**), was used as one of the metal oxides. Characterisation of **$Nb_2O_5$-B1:500** showed this material to be a UV active photocatalyst, able to degrade the model dye Methyl Orange under UV light without any further modification. To **$Nb_2O_5$-B1:500**, chromium oxide ($Cr_2O_3$) was loaded onto the surface by the incipient wetness method, comparable to that used to load PGM material onto $Nb_2O_5$ described in Chapter 4 of this thesis. This material was characterised by XPS, which confirmed the presence of only chromium (III) on the niobium (V) oxide surface. The diffuse reflectance of the chromium oxide – niobium oxide composite ($Cr_2O_3$-$Nb_2O_5$) was determined, and explored in a level of detail not seen in the charge transfer papers referenced previously. Analysis of the optical properties of the material confirmed that $Cr_2O_3$-$Nb_2O_5$ was able to induce MMCT $Nb^{V}/Cr^{III} \rightarrow Nb^{IV}/Cr^{IV}$ using visible light. Finally the photocatalytic properties of the

materials synthesised were characterised by degrading Methyl Orange under visible light. By completing an action spectrum of this degradation, it was confirmed that it was $Cr_2O_3$-$Nb_2O_5$, and so the chromium (III) – niobium (V) MMCT, that was responsible for the Methyl Orange degradation.

## 5.2 Synthesis and Characterisation of $Cr_2O_3$-$Nb_2O_5$

### 5.2.1 Synthesis of $Cr_2O_3$-$Nb_2O_5$

The material was synthesised by impregnating chromium (III) nitrate into $Nb_2O_5$, using the incipient wetness method previously described in Chapter 4, where platinum group metal (PGM) salts were used to impregnate $Nb_2O_5$ with the PGM. As described in Chapter 4, the technique involves mixing the solid niobium oxide material with a liquid chromium precursor up to the point of incipient wetness, and calcining to remove the nitrate precursor. The materials in this chapter were synthesized using the large batch of $Nb_2O_5$, calcined at 500 °C previously characterised in Chapter 3 (**$Nb_2O_5$-B1:500**).

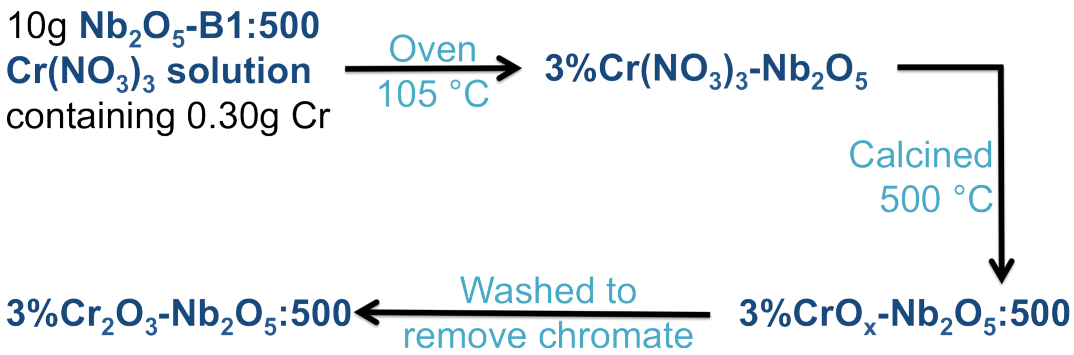


**Scheme 5-1** Schematic showing the synthesis of **3%$Cr_2O_3$-$Nb_2O_5$:500** from **$Nb_2O_5$:500** and a chromium (III) nitrate precursor.

The reaction scheme for synthesising 3% by weight $Cr_2O_3$ on **$Nb_2O_5$-B1:500**, referred to as **3%$Cr_2O_3$-$Nb_2O_5$:500** is illustrated in Scheme 5-1. After the initial impregnation, the material is dried, and then calcined at 500 °C, producing a $Cr_2O_3$ – $Nb_2O_5$ composite with the chromium portion, a mixture of chromium (III) and chromium (VI) oxide (**3%$CrO_x$-**

**$Nb_2O_5$:500**). Washing the material removes the chromium (VI), with the final $Cr_2O_3$ – $Nb_2O_5$ composite (**3%$Cr_2O_3$-$Nb_2O_5$:500**) retained for photocatalysis testing.

A 2.5 M stock solution of chromium (III) nitrate in water was formed, by dissolving 15 g of $Cr(NO_3)_3.9H_2O$ in 25 ml of water, with the solution therefore having a chromium concentration of 0.078 g $ml^{-1}$. The point of incipient wetness of **$Nb_2O_5$-B1:500**, as described in Chapter 4, was found to be 0.4 ml $g^{-1}$. In the **3%$Cr_2O_3$-$Nb_2O_5$:500** synthesis illustrated, 10 g of **$Nb_2O_5$-B1:500** was impregnated with 3.85 ml of the 2.5 M chromium (III) nitrate solution, and 0.15 ml of water to bring the solution up to the incipient wetness point of the **$Nb_2O_5$-B1:500**. This allows a 0.30 g loading of chromium (3% by weight of $Nb_2O_5$). This material was then dried in an oven overnight at 105 °C. The resulting material (**3%$Cr(NO_3)_3$-$Nb_2O_5$**) was then calcined in air at 500 °C for 2 hours, heating at 5 °C $min^{-1}$, and cooling at 10 °C $min^{-1}$. 0.8 g of the as made material (**3%$CrO_x$-$Nb_2O_5$:500**) was then placed in 400 ml distilled water under constant stirring for 2 hours, allowing chromium (VI) to leech out into the water. The solid material was collected by centrifuge at 2500 rpm, and the UV/Vis absorbance of the washing was measured from 240 nm to 600 nm, to determine the chromate content. The collected material was placed in 200 ml of distilled water, and stirred for 30 minutes. Again the material was collected by centrifuge at 2500 rpm, and the chromate content of the washing determined by UV/Vis; this washing procedure continued until no evidence of chromate was detected by UV/Vis absorbance. This final washed **3%$Cr_2O_3$-$Nb_2O_5$:500**, collected by centrifuge, was dried overnight in an oven at 105 °C. 1% by weight chromium (**1%$Cr_2O_3$-$Nb_2O_5$:500**) and 5% by weight chromium (**5%$Cr_2O_3$-$Nb_2O_5$:500**) composites were similarly synthesised by varying the amount of chromium nitrate dissolved in water in the initial stage of the synthesis. For comparison, 1.5 g of the initial impregnated sample was calcined at lower temperature (350 °C) in air (**3%$Cr_2O_3$-$Nb_2O_5$:350)**; 1.5 g of the material was calcined in a nitrogen atmosphere at a temperature of 350 °C (**3%$Cr_2O_3$-$Nb_2O_5$:350N**).

## 5.2.2 Characterisation of 3%$Cr_2O_3$-$Nb_2O_5$:500

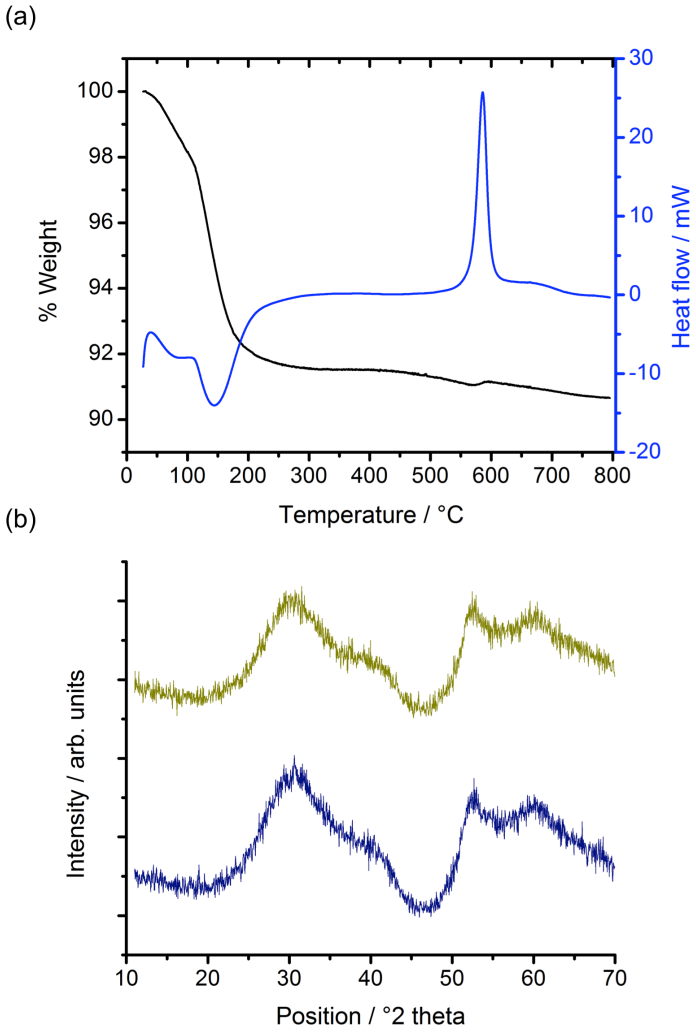


**Figure 5-3** (a) TGA data for material pre calcination (**3%$Cr(NO_3)_3$-$Nb_2O_5$**), showing the weight loss and the heat flow difference. (b) X-ray diffraction patterns of post calcination **3%$CrO_x$-$Nb_2O_5$:500** (dark yellow) and **$Nb_2O_5$-B1:500** (navy).

Figure 5-3(a) illustrates the TGA data for the material after $Nb_2O_5$ is impregnated with the chromium (III) nitrate solution and dried (**3%$Cr(NO_3)_3$-$Nb_2O_5$**) indicating the weight loss and the heat flow difference. CHN for this material shows nitrogen present, which emanates from chromium nitrate on the surface of the niobium oxide. As the temperature increases, there is a dramatic weight loss corresponding to the nitrate decomposing. Sietsma et al[13] discussed the deposition of nickel oxide onto SBA-15 silica using a

comparable impregnation technique with nickel nitrate as the precursor. The group reported nickel nitrate deposits as solid $Ni_3(NO_3)_2(OH)_4$ on drying at 120 °C, with water and nitric acid given off as a gas. As the calcination proceeds, this solid nickel species decomposes to the nickel oxide, with nitrogen dioxide, water and oxygen given off as gas. A comparable decomposition process can be assumed to take place here. CHN data of the post – calcined material (**3%$CrO_x$-$Nb_2O_5$:500**) confirms that the calcination process has removed the nitrate that was present in the original material, **3%$Cr(NO_3)_3$-$Nb_2O_5$**, with nitrogen content being undetectable by CHN microanalysis.

The X-ray diffraction pattern of **3%$CrO_x$-$Nb_2O_5$:500** is illustrated in Figure 5-3(b), in addition to XRD data of **$Nb_2O_5$-B1:500** used in the synthesis. From the data it is clear there is no evidence from XRD of a chromium oxide species on the composite, when compared to the XRD of **$Nb_2O_5$-B1:500**; the two x-ray diffraction patterns are comparable. The BET surface area of the composite was calculated to be 110 $m^2$ $g^{-1}$, comparable to the surface area of **$Nb_2O_5$-B1:500** (118 $m^2$ $g^{-1}$). Xie and Tang[12] discussed the spontaneous monolayer dispersion of oxides and salts onto supports. They noted that at low loadings of oxides onto supports, there is no evidence of the oxide in XRD patterns; as the weight of loading increases, evidence of the oxide appears in the form of crystalline peaks in the x-ray of the material. The point at which this change occurs corresponds to the addition oxide forming a complete monolayer on the surface of the support.

By taking the surface area of **$Nb_2O_5$-B1:500**, the amount of chromium oxide deposited onto the surface can be calculated using the technique Xie and Tang use. It is assumed that the oxide forms a layer, with the $O^{2-}$ ions forming a close packed layer on the surface of the support, in this case, **$Nb_2O_5$-B1:500**. Using the radius of oxygen atoms as 1.4 angstroms, the amount by weight of chromium required to form a monolayer on the surface of **$Nb_2O_5$-B1:500** (with a surface area of 118 $m^2$ $g^{-1}$) can be calculated. This equates to 0.11 g of chromium $g^{-1}$ **$Nb_2O_5$-B1:500** required to form a monolayer; 11% by

weight chromium would produce a monolayer of chromium oxide on the surface of **$Nb_2O_5$-B1:500**.

Therefore, there is 45% surface coverage for the **5%$CrO_x$-$Nb_2O_5$,:500**, 27% surface coverage for **3%$CrO_x$-$Nb_2O_5$:500** and 9% surface coverage for **1%$CrO_x$-$Nb_2O_5$:500**. As these values are significantly below monolayer coverage, one would expect there to be no x-ray peaks for chromium oxide if the oxide is in the crystalline form, which is consistent with previous work, assuming the model is physically correct.

XPS was used to determine the oxidation state of the chromium throughout the synthesis procedure. When the niobium oxide was initially impregnated with chromium (III) nitrate, with chromium in the +3 oxidation state, XPS confirms the presence, with the only chromium species detected being chromium (III) (Figure 5-4(a)). When the **3%$Cr(NO_3)_3$-$Nb_2O_5$** is calcined at 500 °C, some of the chromium present is oxidized to chromium (VI). This can be quantified by XPS to indicate a ratio of 9 : 4 : 87 of $Cr^{III}$, $Cr^{VI}$ and $Nb^{V}$ respectively (Figure 5-4(b)). Calcination of **3%$Cr(NO_3)_3$-$Nb_2O_5$** in a nitrogen atmosphere, as opposed to air, also yields a change in oxidation state of some of the chromium, indicating that the source of the oxidizer must be from the products of the decomposition of the nitrate to the oxide (Table 5-1).

| Calcination conditions | $Cr^{III}$ / % | $Cr^{VI}$ / % |
|---|---|---|
| 500°C, air | 72 | 28 |
| 350°C, air | 43 | 57 |
| 350°C, $N_2$ | 68 | 32 |

**Table 5-1** Ratio of the oxidation state of **3%$CrO_x$-$Nb_2O_5$** material after calcination under various conditions.

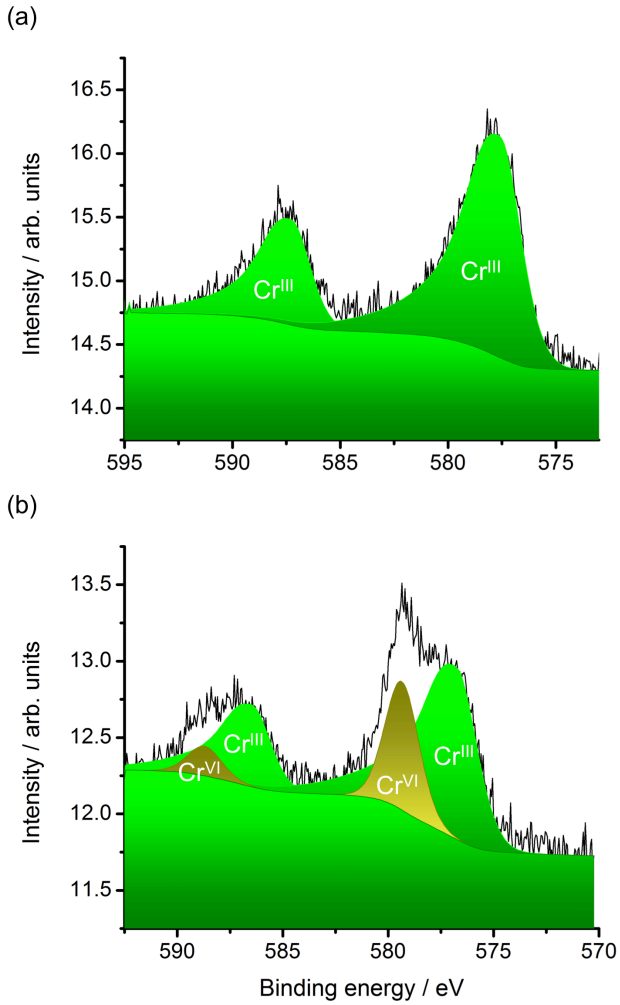


**Figure 5-4** (a) XPS data of material pre calcination, **3%Cr(NO$_3$)$_3$-Nb$_2$O$_5$** with fitted chromium (III) XPS peaks. (b) XPS data of the post 500 °C calcination material, **3%CrO$_x$-Nb$_2$O$_5$,:500** with fitted chromium (III) and chromium (VI) peaks.

Further evidence for the detection of chromate can be found by measuring the UV/Vis spectrum of the deionized water, after stirring the **3%CrO$_x$-Nb$_2$O$_5$:500** composite in the solvent for around 2 hours. The spectrum measured (Figure 5-5(a)) with significant peaks at centered at 256 nm and 350 nm is characteristic of chromium (VI) indicating that chromium (VI) is leeching out of the composite.[14] As the material is continually washed (as described in Section 5.2.2), a significant decrease in intensity of the chromium (VI) peak can be observed, indicating chromium (VI) is being removed from the **3%CrOx-Nb$_2$O$_5$:500**. By continually washing in this way, the amount of chromate leaching out of

the catalyst into the deionized water becomes undetectable by UV/Vis spectroscopy with the absorbance at the most intense chromium (VI) peak (at 256 nm) being less than 0.01 A. (Figure 5-5(a)). This signifies that the chromium (VI) present in **3%CrOx-$Nb_2O_5$:500** has leached out. XPS confirms this is the case; after the washing procedure, the XPS spectrum of **3%$Cr_2O_3$-$Nb_2O_5$:500** can be fitted to chromium (III); there is no evidence in the XPS spectrum of chromium (VI) (Figure 5-5(b)).

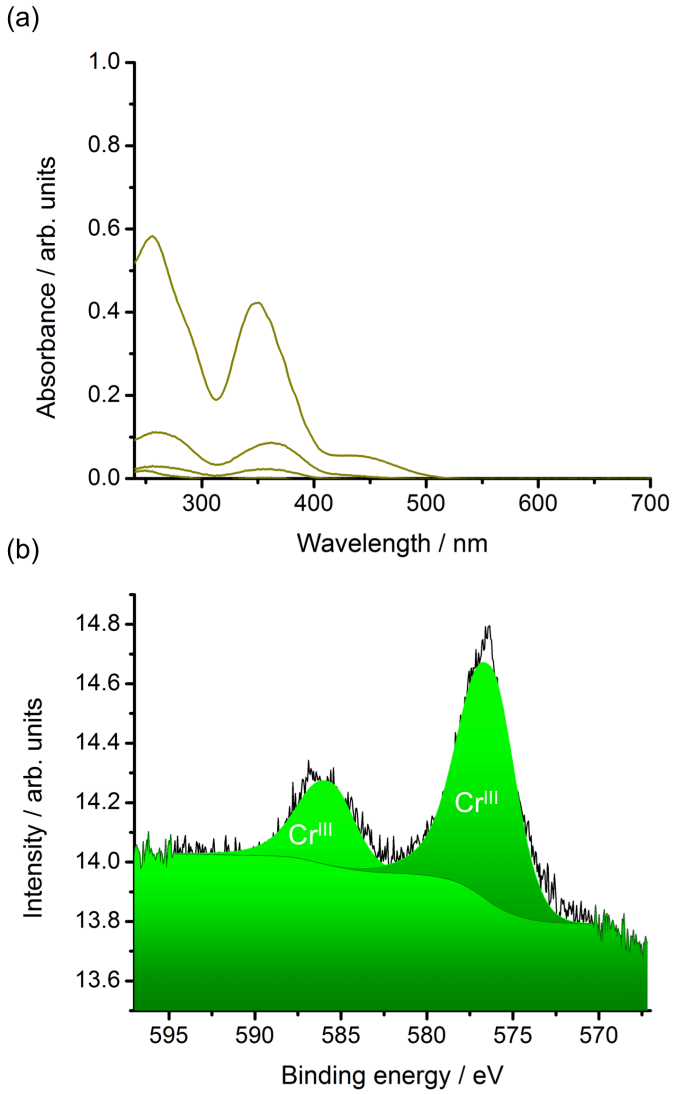


**Figure 5-5** (a) UV Vis absorbance spectra of **3%$CrO_x$-$Nb_2O_5$:500** being washed, with the intensity of the chromium (VI) absorbance peaks decreasing until undetectable by UV/Vis spectroscopy. (b) XPS data of the calcined composite **3%$Cr_2O_3$-$Nb_2O_5$:500** after washing to remove the chromate, with fitted chromium (III) XPS peaks.

## 5.3 Composite Optical Properties

### 5.3.1 Optical Properties During Synthesis

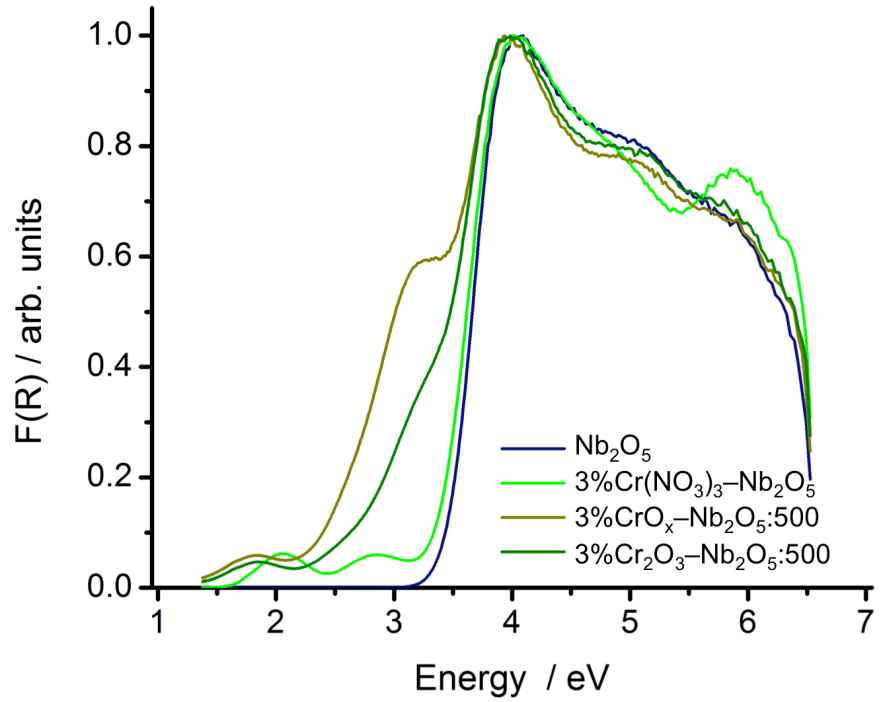


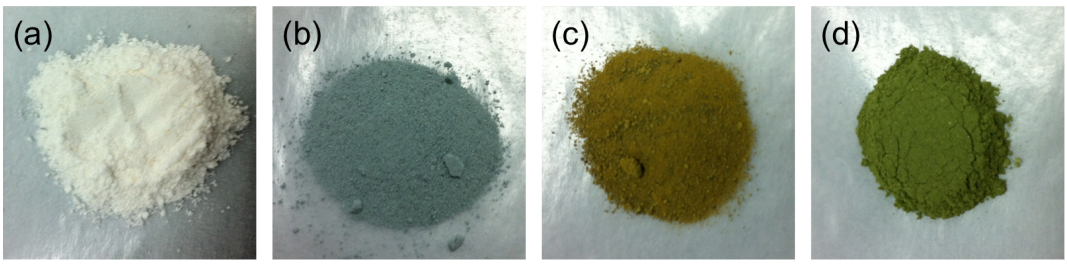


**Figure 5-6** The diffuse reflectance spectra, and photographs of the composite at different stages of the synthesis: a) niobium oxide (**$Nb_2O_5$-B1:500**), b) the chromium impregnated material (**3%$Cr(NO_3)_3$-$Nb_2O_5$**), c) impregnated material after calcination at 500°C (**3%$CrO_x$-$Nb_2O_5$:500**), d) material after removal of chromate (**3%$Cr_2O_3$-$Nb_2O_5$:500**).

As the composite material is synthesised from **$Nb_2O_5$-B1:500**, the material changes colour from the white of **$Nb_2O_5$-B1:500**, through to the green of the final washed composite,

**3%$Cr_2O_3$-$Nb_2O_5$:500**. As the composite changes colour, there is a corresponding change in the material's diffuse reflectance (Figure 5-6).

$Nb_2O_5$ is white (Figure 5-6), and when the green chromium (III) nitrate solution is impregnated onto the $Nb_2O_5$, the green 'stains' the white $Nb_2O_5$, producing a green compound, **3%$Cr(NO_3)_3$-$Nb_2O_5$** (Figure 5-6(b)) which has been impregnated with chromium (III) nitrate. The diffuse reflectance of this green material is dominated by the $Nb_2O_5$ band gap, the feature occurring at 3.6 eV. The visible absorbance seen between 1.3 and 3 eV can be accounted for by the *d – d* transitions from the chromium (III) nitrate present in the compound; the absorbance being comparable to the visible region of the diffuse reflectance of both the solid chromium (III) nitrate used in the synthesis, and chromium (III) oxide, both of which have chromium in the +3 oxidation state. At this stage in the synthesis, the diffuse reflectance does not show any clear interaction between chromium (III) and niobium (V) in the composite. This lack of interaction between the chromium and niobium ions is noticeably different from the chromium (III) – titanium (IV) oxide material synthesised by the Hashimoto group[10-11], who identify $Cr^{III}/Ti^{IV}$ interaction on material that has not been calcined.

When **3%$Cr(NO_3)_3$-$Nb_2O_5$** is calcined at 500 °C in air, the optical properties change significantly. The colour changes from green, to dark yellow in colour, (Figure 5-6(b)) and the diffuse reflectance of **3%$CrO_x$-$Nb_2O_5$:500** now shows significant visible absorption, although the $Nb_2O_5$ band gap is still evident (Figure 5-6). It is noticeable that there is a shift in around 0.1 eV of this band gap feature in **3%$CrO_x$-$Nb_2O_5$:500** compared to **$Nb_2O_5$-B1:500**. XPS of this material shows chromium present as both chromium (III) and chromium (VI) (Figure 5-4(b)) and the diffuse reflectance reflects this. Solutions of chromium (VI) compounds have a characteristic spectrum, with absorbance in the UV region centered around 275 nm (4.5 eV) and 375 nm (3.3 eV).[14] The diffuse reflectance of **3%$CrO_x$-$Nb_2O_5$:500** shows a hump and shoulder between 2.1 eV and 3.5 eV. This

absorbance, which is absent pre-calcination, is due to the chromium (III), chromium (VI) transitions and any interaction between these and the $Nb_2O_5$. The hump around 3.1 eV could be indicative of chromium (VI) absorbance. As chromium (VI) has no *d* electrons present, this absorbance will induce oxygen to chromium charge transfer on the chromium species. Shen and Guo,[15] who synthesised chromium and titanium co-incorporated onto MCM-41 similarly observed chromium (VI) transitions in the UV/Vis spectrum of their material. As the synthesis continues, chromium (VI) is washed out of the material. One would therefore expect the chromate features of the diffuse reflectance to minimize as the chromate is washed out. By examining the diffuse reflectance of **3%$Cr_2O_3$-$Nb_2O_5$:500**, it can be seen that this is the case.

As discussed previously, as the material is washed, the chromium (VI) content of **3%$CrO_x$-$Nb_2O_5$:500** decreases until the amount is too low to be detected by both UV/Vis spectroscopy and XPS. The diffuse reflectance of **3%$Cr_2O_3$-$Nb_2O_5$:500** reflects this, with the feature around 3.3 eV, heavily influenced by chromium (VI) transitions, decreasing. The diffuse reflectance of this final washed product **3%$Cr_2O_3$-$Nb_2O_5$:500** therefore contains absorbance coming from the $Nb_2O_5$, $Cr_2O_3$ on the surface of the $Nb_2O_5$, in addition to any interaction between the chromium (III) and niobium (V) ions i.e. MMCT between the two ions. The next few sections will examine this final washed composite's optical properties by identifying and analysing the individual components of the spectrum.

## 5.3.2 Optical Properties of Niobium Oxide

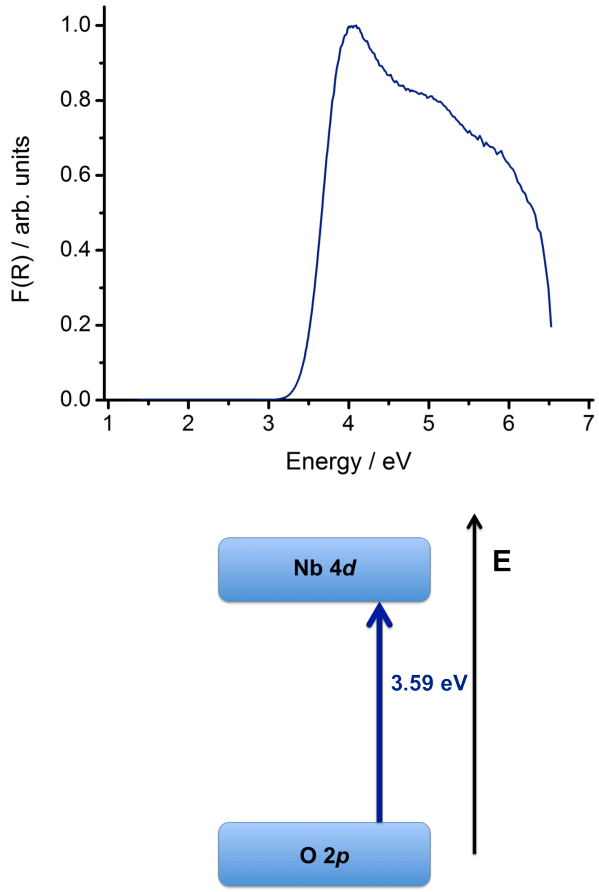


**Figure 5-7** The diffuse reflectance of **$Nb_2O_5$-B1:500** used in the synthesis of **3%$Cr_2O_3$-$Nb_2O_5$:500**, and a diagram representing the electronic structure of $Nb_2O_5$.

The diffuse reflectance of **3%$Cr_2O_3$-$Nb_2O_5$** contains a feature at 3.5 eV which is indicative of the $Nb_2O_5$ band gap, the transitions of electrons from the 2*p* orbitals of the oxygen in the structure to the empty 4*d* orbitals of niobium (V). This transition at 3.6 eV is the only transition possible due to the absence of 4*d* electrons in the niobium (V) oxidation state, as discussed in Chapter 3. As a result, there is no visible absorbance as seen in the $Nb_2O_5$ diffuse reflectance (Figure 5-7), and the electronic structure can be plotted in a diagram, showing the relatively straightforward oxygen 2*p* to niobium 4*d* transition.

## 5.3.3 Optical Properties of Chromium Oxide

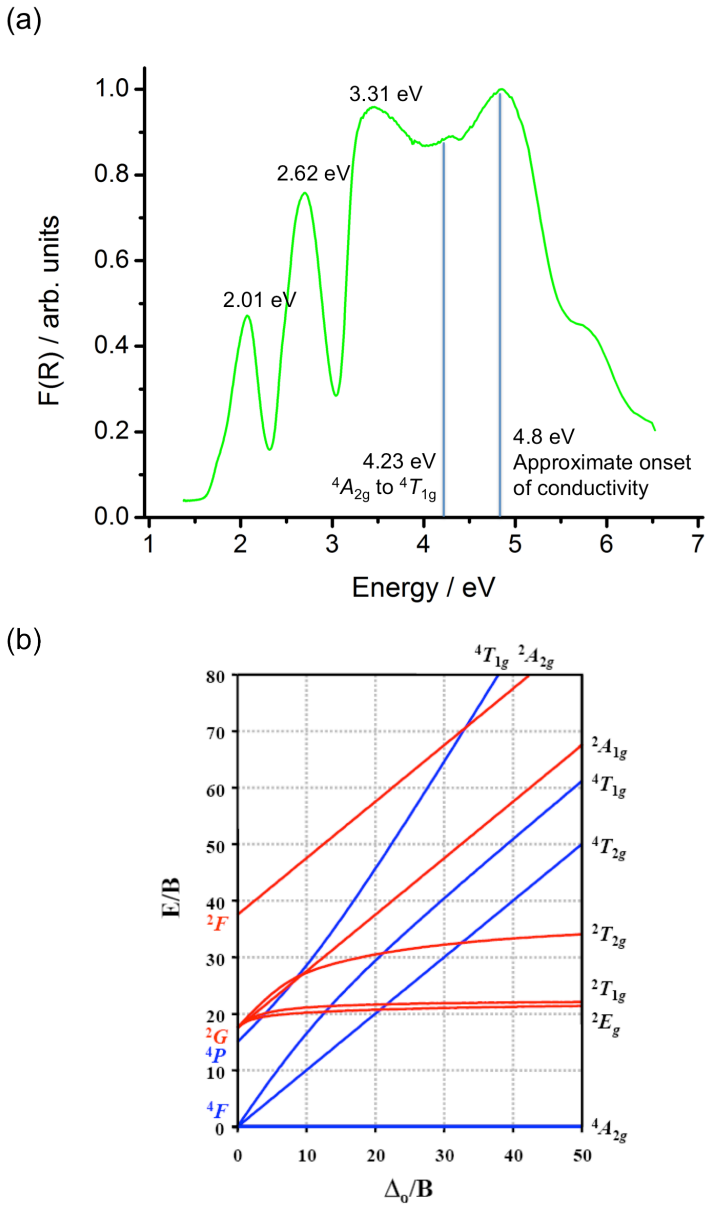


**Figure 5-8** (a) The measured diffuse reflectance of bulk chromium (III) oxide, purchased from Sigma – Aldrich (b) The Tanabe-Sugano diagram for a $d^3$ metal, as in chromium (III) oxide, indicating the electronic transitions that can take place involving the three *d* electrons.

As discussed, $Nb_2O_5$ is a $d^0$ oxide due to the metal niobium being in the +5 oxidation state, and so having no *d* electrons. Chromium (III) oxide on the other hand, has chromium in the +3 oxidation state, and so the chromium has the outer shell electronic shell structure $3s^2 3p^6 3d^3$. Unlike the $Nb_2O_5$ diffuse reflectance, the chromium (III) oxide, with three *d*

electrons, shows visible absorbance in the diffuse reflectance spectra, noticeably features at 2.01 eV, 2.62 eV and another feature at in the UV region at 3.31 eV (Figure 5-8(a)). The visible absorbance is responsible for the green colour of the chromium (III) oxide.

For a $d^3$ metal complex, electronic diagrams such as the Tanabe-Sugano diagram can be used to determine electronic transitions (Figure 5-8(b)). In a free gaseous metal, the *d* orbitals are degenerate, and so there will be no spectra from $d - d$ transitions. However complexes that have ligands split the *d* orbitals into two groups, due to the electrostatic field effect from the ligand. The strength of the ligand field determines the energy difference between the different energy states. Different energy states can be assigned a term symbol with the chromium (III) ground state being assigned $^4F$, consisting of three parallel spinning electrons in three 3*d* orbitals. Excited states are possible; however Laporte selection rules state electronic transitions cannot change spin. As a result, transitions from the ground state to spin different states are forbidden and will produce weak spectra that are not seen. Laporte allowed electronic transitions are from the $^4F$ to $^4P$ electronic states, both of which have three parallel spinning electrons. In an octahedral complex with ligands, $^4P$ is not split, but transforms to a $^4T_{1g}(P)$ state. The $^4F$ state splits into $^4A_{2g} + {}^4T_{1g}(F) + 4T_{2g}$ states, with the $^4A_{2g}$ state being the state lowest in energy i.e. the ground state.

The chromium (III) oxide, with the chromium in the +3 oxidation state surrounded by oxygen atoms can be approximated to that of a chromium (III) octahedral complex in terms of the oxide's electronic structure. Therefore the Tanabe-Sugano diagram predicts three spin allowed $d - d$ electronic transitions possible for the oxide. The two features occurring in the visible region of the chromium (III) oxide diffuse reflectance are $d - d$ transitions, and so correspond to the first and second of these spin allowed transitions. From these two, the energy of the third can be predicted using the Tanabe-Sugano diagram.

$^4A_{2g}$ to $^4T_{2g}$ 2.01 eV

$^4A_{2g}$ to $^4T_{1g}$ (*F*) 2.62 eV

$^4A_{2g}$ to $^4T_{1g}$ (*P*) 4.23 eV

Therefore the energy required allowing the third transition from the ground state, 4.23 eV, is well into the UV region of the spectra, and as seen in the diffuse reflectance of chromium (III) oxide, is hidden by the strong feature at 3.31 eV.

The feature in the UV region at 3.31 eV is consistent with a ligand-to-metal charge transfer (LMCT) transition. In the chromium (III) oxide, an electron from the oxygen is being promoted to the chromium 3*d* orbital. This transition and the three *d* – *d* transitions, are all localised internal electronic transitions, which do not facilitate conduction away from the metal oxide. This can be further demonstrated by the lack of reports of chromium (III) oxide as a visible light photocatalyst despite absorbing visible light, and confirmed by experiments carried out later in this chapter.

Electronic structure studies of chromium (III) oxide by Uozumi et al[16] report the approximate onset of conductivity of chromium (III) oxide to be 4.8 eV. This indicates that the transition that occurs at 4.8 eV allows electrons to occupy states not localised on a single chromium (III) centre, and may be considered its band gap. Here, the electronic transition that is taking place is from the oxygen 2*p* orbital, to the chromium 4*s* orbital, which is essentially the chromium (III) oxide conduction band; as the chromium 4*s* and 2*p* orbitals are more delocalized than the chromium 3*d* orbitals, conduction is allowed.

These transitions can be represented in a diagram (Figure 5-9), which adequately explains the diffuse reflectance data obtained of the bulk chromium (III) oxide, and also explains why, as can be seen later in this chapter, chromium (III) oxide does not degrade methyl orange under visible light, despite the chromium (III) oxide being able to absorb visible light.

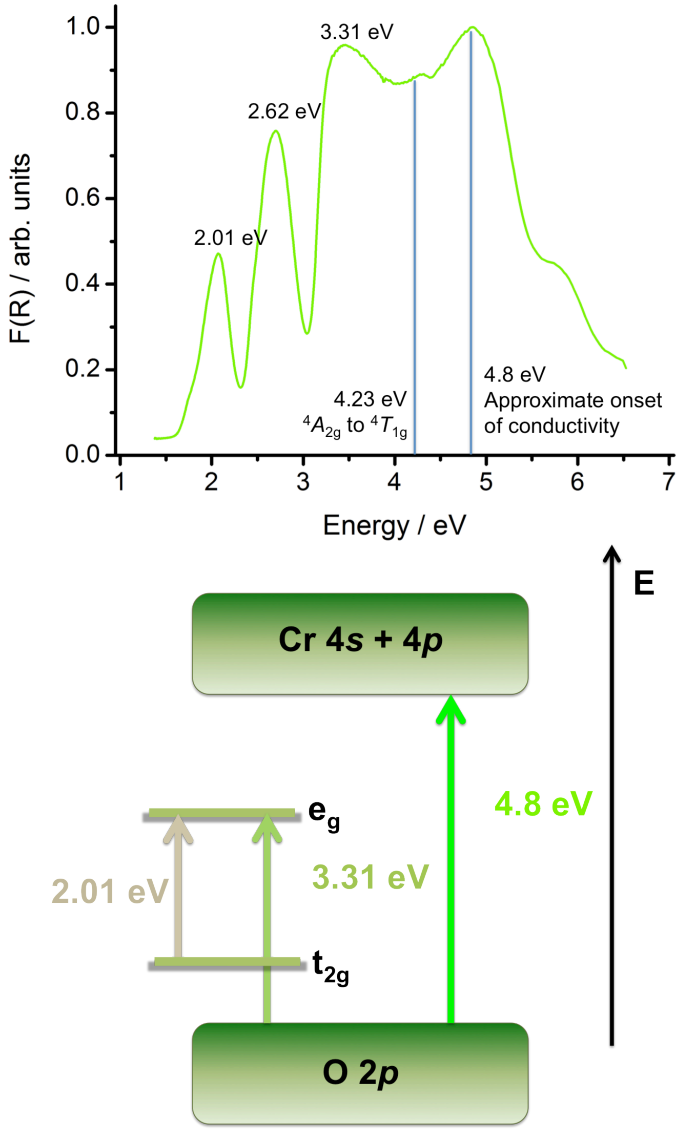


**Figure 5-9** The measured diffuse reflectance of bulk chromium (III) oxide purchased from Sigma – Aldrich, and a diagram representing the electronic structure of the bulk chromium (III) oxide.

## 5.3.4 Optical Properties of 3%$Cr_2O_3$-$Nb_2O_5$:500

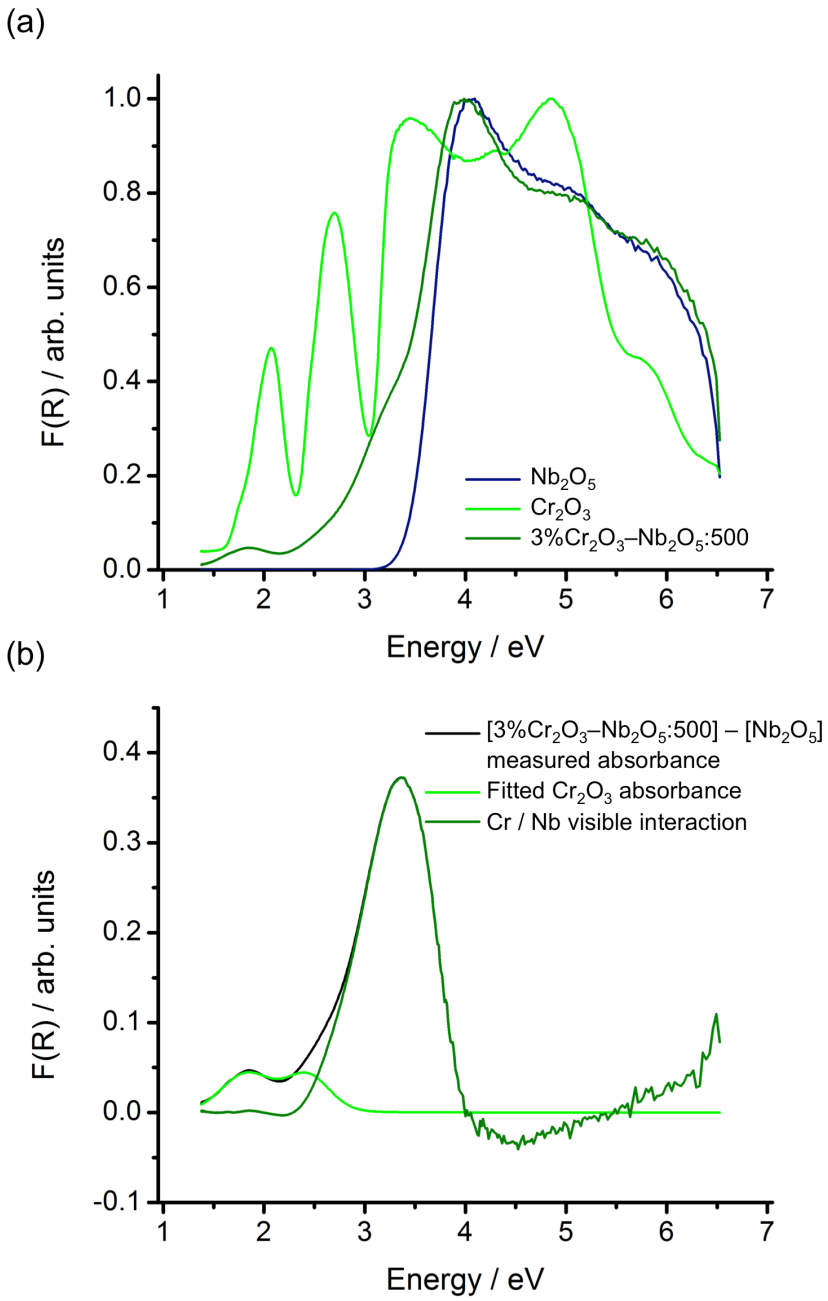


**Figure 5-10** (a) Diffuse reflectance of **$Nb_2O_5$-B1:500**, bulk chromium (III) oxide ($Cr_2O_3$) purchased from Sigma – Aldrich, and **3%$Cr_2O_3$-$Nb_2O_5$.:500** (b) Diffuse reflectance spectra showing the measured difference between the **3%$Cr_2O_3$-$Nb_2O_5$:500** and **$Nb_2O_5$-B1:500**, spectra ([3%$Cr_2O_3$-$Nb_2O_5$ – [$Nb_2O_5$]), the fitted $Cr_2O_3$ absorbance emanating from $Cr_2O_3$ on the **3%$Cr_2O_3$-$Nb_2O_5$:500**, and the chromium – niobium visible interaction of **3%$Cr_2O_3$-$Nb_2O_5$:500** from the measured spectra.

The **3%$Cr_2O_3$-$Nb_2O_5$:500** was synthesised by loading chromium (III) oxide onto the surface of niobium (V) oxide, with XPS confirming the presence of chromium (III) ions and niobium (V) ions. The diffuse reflectance of **3%$Cr_2O_3$-$Nb_2O_5$:500** will therefore be a composite of the chromium (III) oxide and niobium (V) oxide, whose optical properties were discussed in the previous two sections. By normalizing to the maximum absorbance the diffuse reflectance spectrum of **$Nb_2O_5$-B1:500**, chromium (III) oxide and **3%$Cr_2O_3$-$Nb_2O_5$:500**, the spectrum of the three can be compared (Figure 5-10(a)), and the difference in the spectra, noticeably in the visible region can be seen. By subtracting the measured **$Nb_2O_5$-B1:500** diffuse reflectance from the measured diffuse reflectance of **3%$Cr_2O_3$-$Nb_2O_5$:500**, the difference between the two, highlighting the visible absorbance can be seen more clearly (Figure 5-10(b)).

This difference spectrum, in addition to showing chromium – niobium interaction, also shows optical absorbance emanating from the chromium (III) oxide on the surface of **$Nb_2O_5$-B1:500**, with the feature at 1.83 eV comparable with *d* – *d* transitions of chromium (III) oxide discussed in the previous section, specifically the *d* – *d* $^4A_{2g}$ to $^4T_{2g}$ transition. This transition occurs at a lower energy than that of the bulk chromium (III) oxide, indicating a change in ligand field strength, which may be accounted for by noting the thin layer of chromium (III) oxide on the surface of **$Nb_2O_5$-B1:500**, as opposed to bulk chromium (III) oxide. Although the second visible *d* – *d* transition $^4A_{2g}$ to $^4T_{1g}$ is not evidenced in the spectra as clear as the $^4A_{2g}$ to $^4T_{2g}$ transition, the transition will be present in the absorbance. As the energy difference between the $^4A_{2g}$ to $^4T_{2g}$ and $^4A_{2g}$ to $^4T_{1g}$ is equivalent for much of the Tanabe-Sugano diagram (Figure 5-8(b)), it can be assumed that the $^4A_{2g}$ to $^4T_{1g}$ transition will occur at an equivalent higher energy in **3%$Cr_2O_3$-$Nb_2O_5$:500** as in the bulk. This transition will therefore occur at 2.43 eV in **3%$Cr_2O_3$-$Nb_2O_5$:500**. Although this second *d* – *d* transition is hidden in the spectra, the first *d* – *d* transition can be fitted into the spectrum, and the second transition can be comparably fitted, allowing the visible optical absorbance of the chromium oxide on the surface of

niobium oxide to be realized. As with the **$Nb_2O_5$-B1:500** absorbance spectrum, this fitted visible chromium (III) oxide spectrum can also be subtracted from the **3%$Cr_2O_3$-$Nb_2O_5$** diffuse reflectance, leaving just the interaction between the chromium (III) oxide on the surface of **$Nb_2O_5$-B1:500** and **$Nb_2O_5$-B1:500** itself (Figure 5-10b).

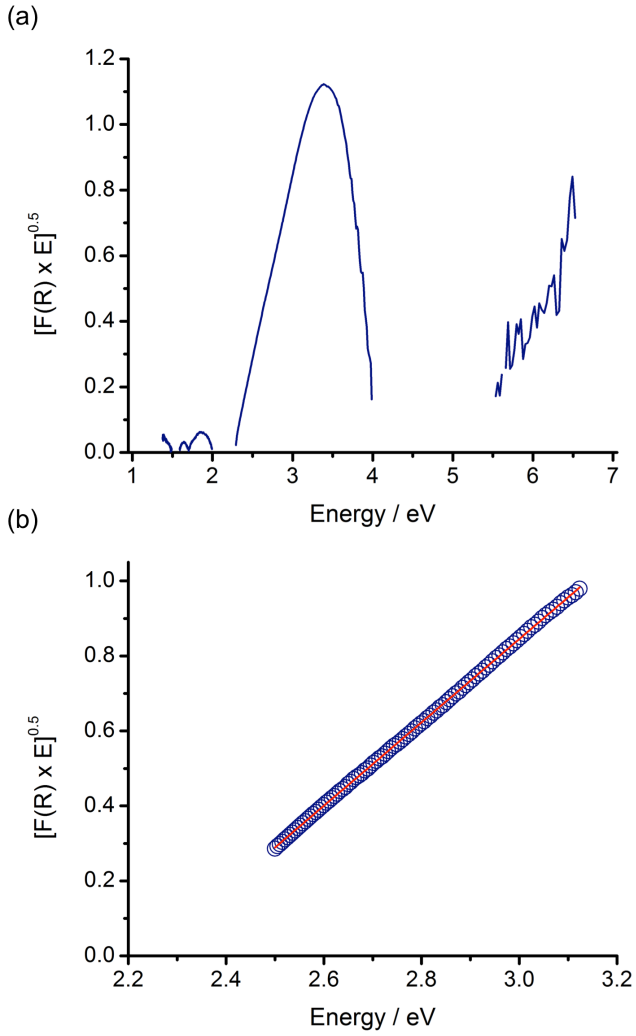


**Figure 5-11** (a) The chromium – niobium interaction of **3%$Cr_2O_3$-$Nb_2O_5$:500**, plotted as an indirect band gap diagram. (b) The extrapolation of the linear section of the spectrum to determine the intercept of the x-axis, hence the indirect band gap, calculated to 2.27 eV, with $R^2$=0.999.

As discussed in Chapter 2, the Kubelka-Munk function (F) plotted as $[F(R)xE]^{0.5}$ vs energy will be linear above the indirect band gap, with the intercept of the linear section with the

x-axis giving the value of the indirect band gap. By plotting $[F(R)xE]^{0.5}$ vs energy for the chromium – niobium interaction determined by removing the chromium (III) oxide and $Nb_2O_5$ influence in the visible region of the diffuse reflectance spectrum (Figure 5-11(a)), a linear section is evident, and a straight line with a $R^2$ value of 0.999 can be plotted (Figure 5-11(b)). By extrapolating this linear section, the indirect band gap can be determined, with the intercept of the x-axis calculated to be 2.27 eV.

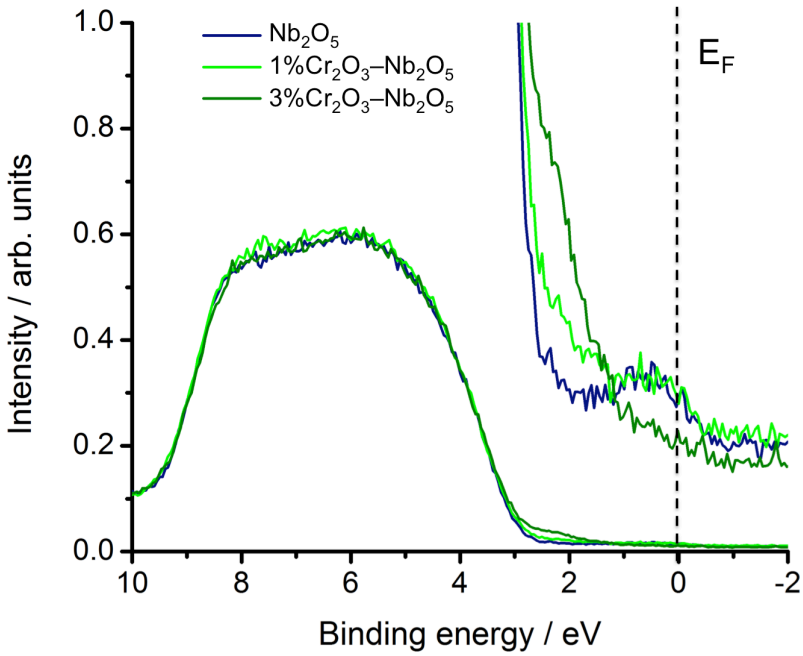


**Figure 5-12** Valence band XPS data for **$Nb_2O_5$-B1:500**, **1%$Cr_2O_3$-$Nb_2O_5$:500** and **3%$Cr_2O_3$-$Nb_2O_5$:500**. Insert shows the binding energy from 2.5 eV to -2 eV at 20x magnification.

This transition calculated could be from chromium (III) *d* states to the $Nb_2O_5$ conduction band, or alternatively a ligand – metal charge transfer from the oxygen 2*p* orbitals to the chromium (II) 3*d* orbitals. To determine which of these is the case, valence band XPS was carried out on both **1%$Cr_2O_3$-$Nb_2O_5$:500** and **3%$Cr_2O_3$-$Nb_2O_5$:500**, in addition to **$Nb_2O_5$-B1:500** (Figure 5-12). This shows the density of filled states at different binding energies. **1%$Cr_2O_3$-$Nb_2O_5$:500** shows filled electronic states above the valence band maximum of niobium oxide. These filled electron states are more evident in **3%$Cr_2O_3$-**

**$Nb_2O_5$:500**, indicating that these are chromium derived states, which must be chromium 3*d* states as these are the only filled valence orbitals in chromium (III) ions. As shown in Figure 5-12, these chromium 3*d* states are centred on 2.3 eV. The binding energy scale of the valence band X-ray photoelectron spectra are set so that zero binding energy corresponds to the Fermi level. In $Nb_2O_5$, which is an n-type semiconductor, the Fermi level will be located at the conduction band minimum, due to the presence of donor states just below the conduction band. Therefore the chromium 3*d* states shown in Figure 5-12 are approximately 2.3 eV below the conduction band. This gives good agreement with the optical transition of 2.27 eV seen in these materials being assigned as transfer from chromium (III) 3*d* states to the $Nb_2O_5$ conduction band, consisting predominantly of niobium 4*d* orbitals.

This XPS data, in addition to the indirect band gap calculated from the diffuse reflectance of **3%$Cr_2O_3$-$Nb_2O_5$:500** is conclusive evidence that there is a metal-metal charge transfer transition from the chromium 3*d* orbital to the niobium 4*d* orbital, requiring energy of 2.27 eV to accomplish this.

The transitions evident on **3%$Cr_2O_3$-$Nb_2O_5$:500** can be illustrated (Figure 5-13), presenting the chromium $d - d$ transitions taking place, the niobium oxide band gap transition and the metal-to-metal charge transfer taking place i.e. $Cr^{III} + Nb^{V} \rightarrow Cr^{IV} + Nb^{IV}$.

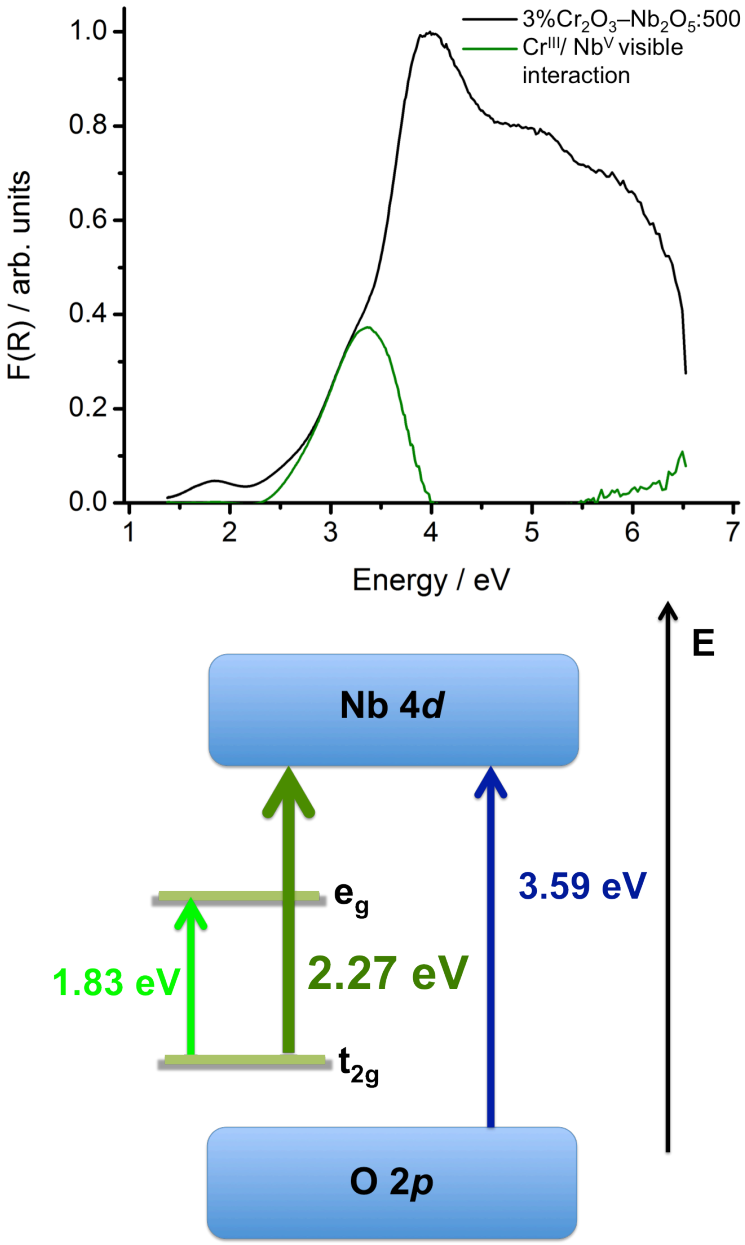


**Figure 5-13** The diffuse reflectance of **3%$Cr_2O_3$-$Nb_2O_5$:500**, including the metal – metal charge transfer (MMCT) interaction between $Cr^{III}$ and $Nb^{V}$, and a diagram representing the electronic structure of **3%$Cr_2O_3$-$Nb_2O_5$:500**.

## 5.4 Photocatalysis Reactions

### 5.4.1 Methyl Orange Visible Light Photocatalysis

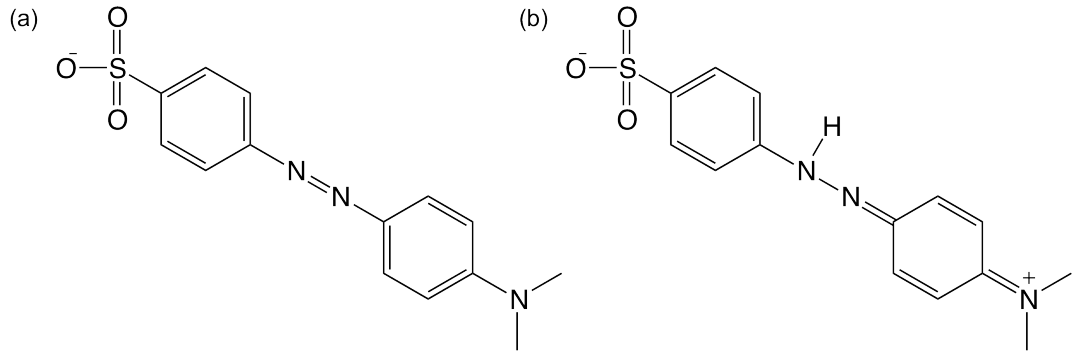


**Figure 5-14** (a) The structure of the yellow / orange form of methyl orange. The extinction coefficient for this compound is 2.68 x $10^4$ $dm^3$ $mol^{-1}$ $cm^{-1}$.[17] (b) The structure of the red protonated form of methyl orange; extinction coefficient is 4.57 x $10^4$ $dm^3$ $mol^{-1}$ $cm^{-1}$.[18]

In order to confirm that the MMCT identified in the composite material could be used for visible light photocatalysis, the degradation of the model dye methyl orange under visible light was tested as a model reaction. As discussed in Chapter 2, methyl orange is a stable dye under visible light due to the molecule undergoing rapid trans – cis photo-isomerization, having a short excited state lifetime, and so eliminating the self-degradation that is common in many visible light dyes.[17]

The zeta potential of **5%$Cr_2O_3$-$Nb_2O_5$:500** was measured in both the deionized water (pH 6.9) used to make up the methyl orange solution, and the acetate buffer used to make up the red form of the methyl orange solution (pH 3.5) used in the degradation reactions. The zeta potential of the composite in water was –40.7 mV; the zeta potential of the composite in acetate pH 3.5 buffer solution was –6.29 mV, indicating the surface charge of the **5%$Cr_2O_3$-$Nb_2O_5$:500** is closer to zero at the lower pH. Due to the negative charge of the Methyl Orange at a neutral pH, and with the surface charge of **5%$Cr_2O_3$-$Nb_2O_5$:500** negative, methyl orange does not absorb as readily onto the surface of **5%$Cr_2O_3$-$Nb_2O_5$:500**. However at lower pH, the protonated red form of methyl orange has a neutral

surface charge, with the surface charge of **5%$Cr_2O_3$-$Nb_2O_5$:500** also close to zero, so the methyl orange absorbs onto the surface of **5%$Cr_2O_3$-$Nb_2O_5$** more readily at lower pH, compared to neutral pH. Therefore, the methyl orange degradation reactions were studied at pH 3.5, using the red form of methyl orange.

## 5.4.2 Methyl Orange Degradation of Niobium Oxide and Chromium Oxide Under Visible Light

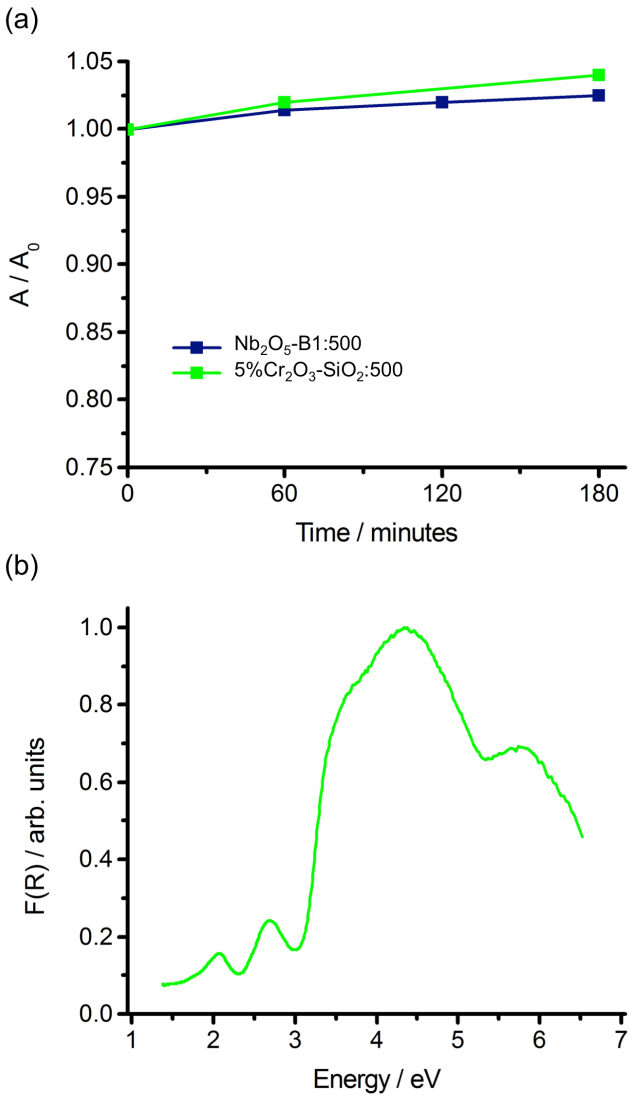


**Figure 5-15** (a) The change in concentration of the red form of methyl orange over the course of a visible light reaction with **$Nb_2O_5$-B1:500** or **5%$Cr_2O_3$-$SiO_2$:500**, (b) The diffuse reflectance of **5%$Cr_2O_3$-$SiO_2$:500**.

As the **5%$Cr_2O_3$-$Nb_2O_5$:500** contains both $Nb_2O_5$ and chromium (III) oxide ($Cr_2O_3$), reactions were first carried out with these two materials to confirm that they do not react with methyl orange under visible light. The band gap of $Nb_2O_5$, at 3.6 eV, is too wide to allow visible light absorbance, whilst the optical properties of $Cr_2O_3$, discussed earlier in this chapter, show the visible absorbance induce localised *d* – *d* transitions. **$Nb_2O_5$-B1:500**, used in the synthesis of **5%$Cr_2O_3$-$Nb_2O_5$:500** was reacted with the red form of methyl orange (0.02 g $L^{-1}$, 6.11 x $10^{-5}$ M methyl orange in 0.01 M acetate buffer solution) under visible light using the standard methyl orange degradation protocol as described in Chapter 2. As the light (greater than 420nm) is not energetic enough to excite the electrons into the conduction band of **$Nb_2O_5$-B1:500** a reaction is not expected. However a dye sensitization reaction could occur, as the methyl orange does absorb visible light and could inject an electron into the $Nb_2O_5$ conduction band. It can be seen however, that the concentration of methyl orange remains constant as the reaction proceeds (Figure 5-15 (a)), and so $Nb_2O_5$ does not degrade the red form of methyl orange under visible light; implying that the light being absorbed by the methyl orange is being used to power the cis – trans photo-isomerization of the molecule.

As with $Nb_2O_5$, $Cr_2O_3$ would not be expected to degrade methyl orange under visible light. As explained in Section 5.3.3, $Cr_2O_3$, although absorbing visible light, does not facilitate electron migration from the visible absorbance of the material, therefore would not be expected to undergo a reaction under visible light. Again, it is possible a dye sensitization reaction could take place, with electrons from the methyl orange entering the 4*s* orbitals, which are known to be conducting. To replicate the $Cr_2O_3$ that is present on the composite, $Cr_2O_3$ was loaded onto the silica particles (**5%$Cr_2O_3$-$SiO_2$:500**) with a surface area of 90 $m^2$ $g^{-1}$, using the protocol discussed in Section 5.2.1, including the calcination and washing steps to remove chromate. As silica has a band gap of 9 eV,[19] a charge transfer of chromium to silicon comparable to the $Cr^{III}$ – $Nb^{V}$ interaction would not be expected, and the diffuse reflectance of **5%$Cr_2O_3$-$SiO_2$:500** confirm this to be the case (Figure 5-15 (b)).

The visible light region of the diffuse reflectance of **5%$Cr_2O_3$-$SiO_2$:500** is comparable to bulk $Cr_2O_3$, with *d* – *d* transitions present in the visible region, and the LMCT present in the UV region; the silica electronic transitions being outside the range of the UV/Vis instrument measurement. Using the standard visible light methyl orange degradation protocol (Chapter 2), it can be seen that as with $Nb_2O_5$, the concentration of methyl orange remains constant over the course of the reaction (Figure 5-15).

### 5.4.3 Methyl Orange Degradation of 5%$Cr_2O_3$-$Nb_2O_5$:500 Under Visible Light

The previous section indicates that the two components of **5%$Cr_2O_3$-$Nb_2O_5$:500** do not degrade methyl orange when reacted under visible light. In order to see if the MMCT chromium (III) – niobium (V) interaction can degrade methyl orange under visible light, **5%$Cr_2O_3$-$Nb_2O_5$:500** was reacted with methyl orange under visible light, using the standard protonated methyl orange protocol (Figure 5-16(a)). It can be seen that as the reaction with **5%$Cr_2O_3$-$Nb_2O_5$:500** proceeds, the concentration of methyl orange decreases, and the reaction can be plotted as a first order kinetics plot (Figure 5-16(b). As the concentration of **5%$Cr_2O_3$-$Nb_2O_5$:500** increases from 1.0 g $L^{-1}$ up to 2.0 g $L^{-1}$ there is a comparable increase in the reaction rate. At 2.5 g $L^{-1}$ however, the reaction rate remains comparable to the rate at 2 g $L^{-1}$, indicating at the concentration of 2 g $L^{-1}$, **5%$Cr_2O_3$-$Nb_2O_5$:500** is absorbing the maximum amount of light.

From the blank experiments carried out, it can be concluded that as $Nb_2O_5$ and $Cr_2O_3$ do not undergo a reaction with methyl orange on their own, **5%$Cr_2O_3$-$Nb_2O_5$:500** and the chromium (III) – niobium (V) interaction could be responsible for the degradation. Although it has been shown that $Cr_2O_3$ and $Nb_2O_5$ are not dye sensitized by the methyl orange, it is possible that **5%$Cr_2O_3$-$Nb_2O_5$:500** could be undergoing a dye sensitized

reaction with the methyl orange. To disprove this, action spectrum experiments were carried out.

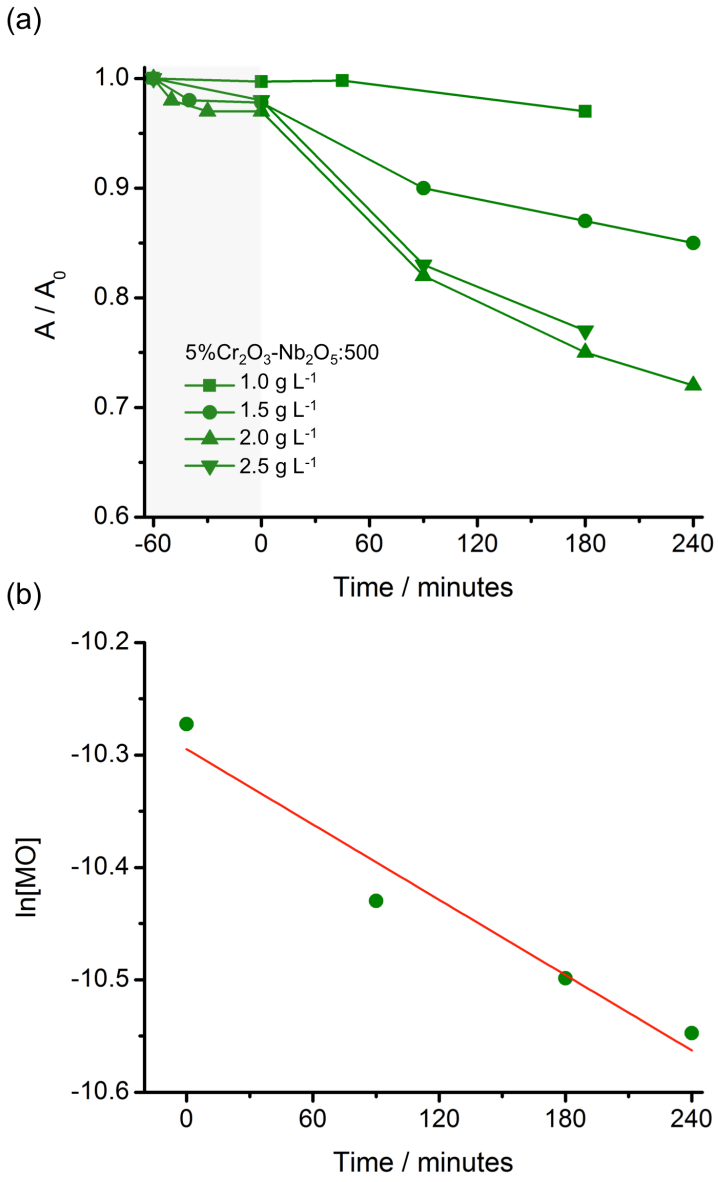


**Figure 5-16** (a) The change in concentration of the red form of methyl orange over the course of a reaction of **5%$Cr_2O_3$-$Nb_2O_5$:500** at concentrations of 1 g $L^{-1}$ to 2.5 g $L^{-1}$ under visible light. (b) The change in concentration of the red form of methyl orange plotted as a first order kinetic plot, over the course of a reaction of **5%$Cr_2O_3$-$Nb_2O_2$:500** with methyl orange under visible light.

## 5.4.4 Action Spectrum of 5%$Cr_2O_3$-$Nb_2O_5$:500

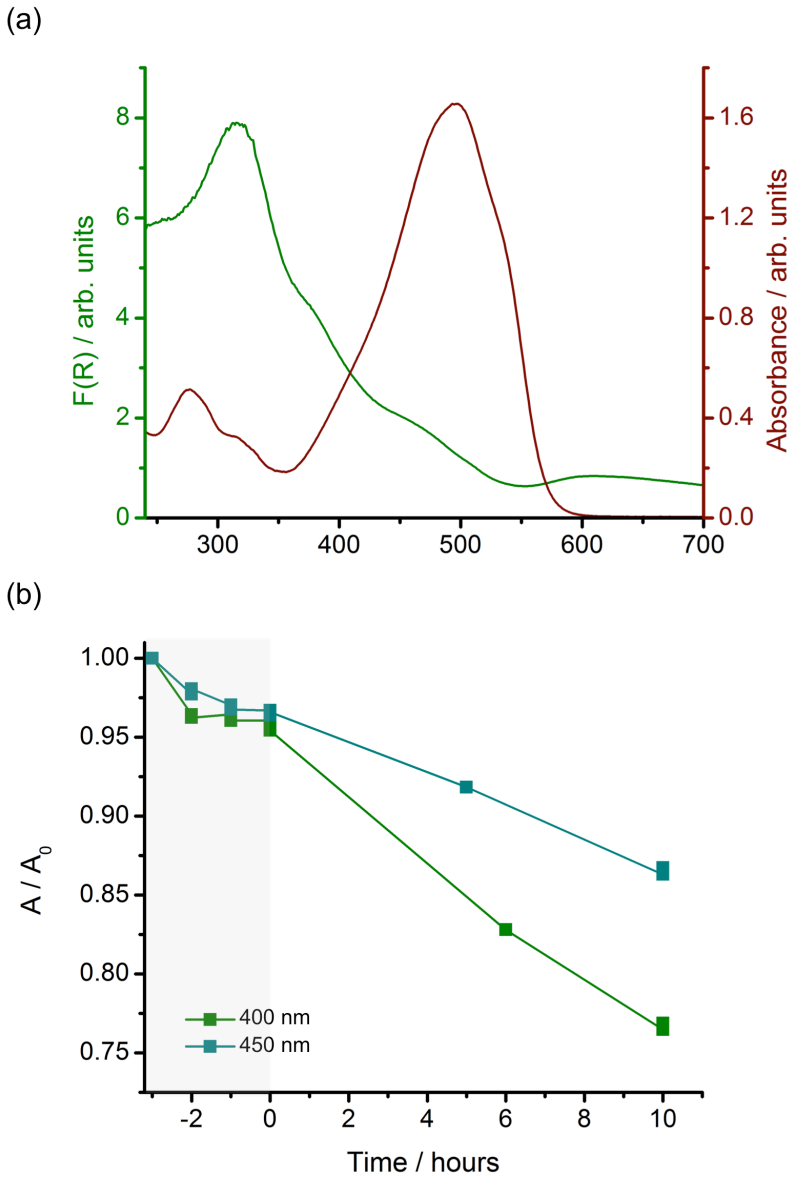


**Figure 5-17** (a) Absorbance spectrum of methyl orange (red), and diffuse reflectance of **5%$Cr_2O_3$–$Nb_2O_5$:500** (green) used in the action spectrum methyl orange degradation reactions, with the frequency of band pass filters (400 nm and 450 nm) highlighted. (b) Change in concentration of methyl orange with the **5%$Cr_2O_3$–$Nb_2O_5$:500** composite reacted under the 400nm band pass filter. c) Change in concentration of methyl orange with the **5%$Cr_2O_3$–$Nb_2O_5$:500** composite reacted under the 450 nm band pass filter.

The absorbance spectrum of the protonated form of methyl orange has its absorbance maximum at 495 nm (2.50 eV), with absorbance intensity decreasing from 450 nm to 400 nm. Conversely, the **5%$Cr_2O_3$-$Nb_2O_5$:500** absorbance increases from 450 nm through to 400 nm, with the MMCT of chromium (III) to niobium (V) predominantly responsible for this absorbance. Potassium ferrioxalate chemical actinometry experiments as described in Chapter 2 of this thesis give the value of the photon flux incident on the reactor as 1.15 x $10^{20}$ photons $h^{-1}$ at 400 nm, and 2.10 x $10^{20}$ photons $h^{-1}$ at 450 nm, when using the 300W Xenon lamp with the respective band pass filters. Quantum efficiencies can therefore be determined by carrying out methyl orange degradation reactions utilizing the 400 nm and 450 nm band pass filters, and determining the moles of methyl orange degraded by using the absorbance coefficient for the red form of methyl orange. Due to the total light intensity being lower through the band pass filters compared to the 420 nm cut off filter, reactions are carried out for a longer time, in order to get a significant reduction in the methyl orange concentration.

These experiments were repeated; in both cases a higher amount of methyl orange was degraded when using light centered at a wavelength of 400nm. These results can be plotted as quantum efficiency with the **5%$Cr_2O_3$–$Nb_2O_5$:500** or methyl orange absorbance on the same graph, and this action spectrum diagram shows that the efficacy of degradation is based on the **5%$Cr_2O_3$–$Nb_2O_5$:500** absorbance rather than the methyl orange absorbance (Figure 5-18). Moreover, the actual degradation efficiency follows more precisely the absorbance of the chromium (III) – niobium (V) charge transfer as opposed to the absorbance emanating from the $Cr_2O_3$ and charge transfer visible absorbance combined. These results show that the chromium (III) – niobium (V) MMCT can be identified from the **5%$Cr_2O_3$–$Nb_2O_5$:500** diffuse reflectance, and this interaction in isolation causes the observed visible light methyl orange degradation.

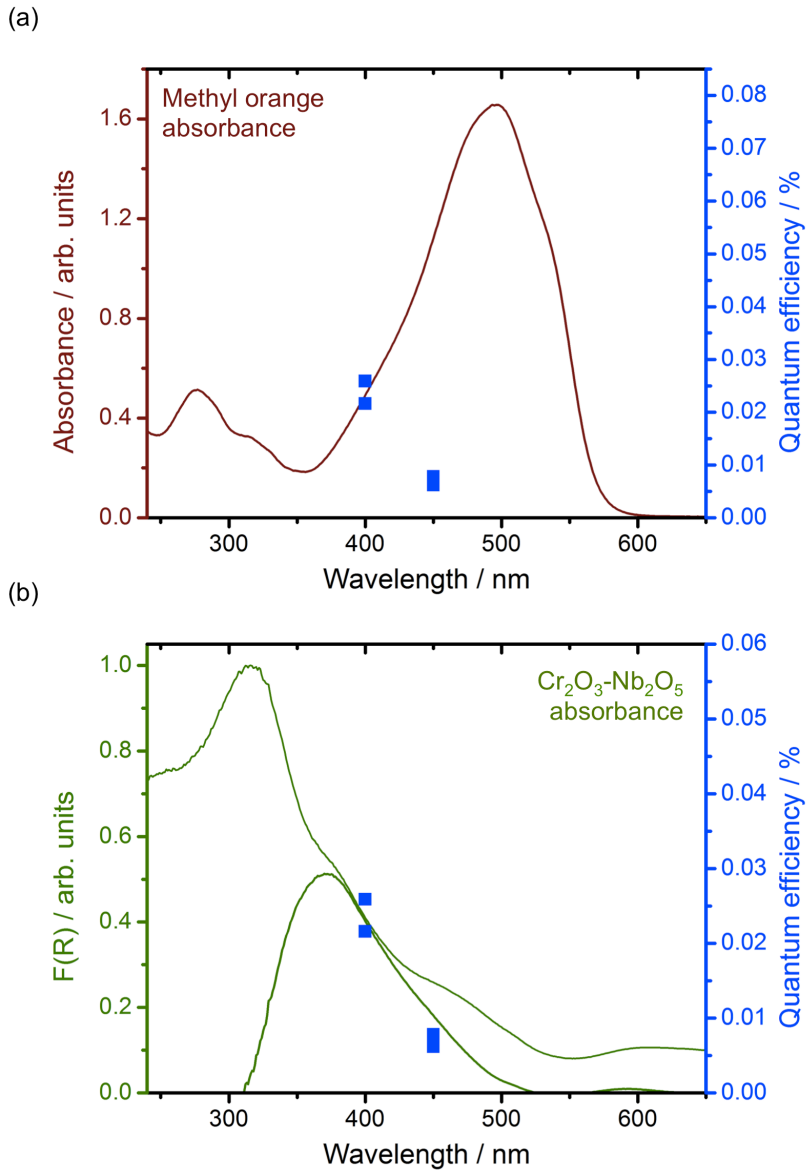


**Figure 5-18** (a) Quantum efficiency of the **5%$Cr_2O_3$–$Nb_2O_5$:500** visible light reaction with methyl orange overlaid with the absorbance spectrum of methyl orange. (b) Quantum efficiency of **5%$Cr_2O_3$–$Nb_2O_5$:500** visible light reaction with methyl orange overlaid with the diffuse reflectance of **5%$Cr_2O_3$–$Nb_2O_5$:500**.

## 5.5 Conclusion and Future Work

The diffuse reflectance of the chromium – niobium material, in addition to the XPS data, quite clearly demonstrate metal to metal charge transfer between chromium (III) on the surface of the $Nb_2O_5$, and the niobium oxide itself. This interaction particularly clear from

the diffuse reflectance of the actual chromium to niobium interaction, obtained by subtracting the absorbance of the niobium oxide and chromium oxide on the surface of the composite, with the energy of this indirect transition calculated to be in the visible region. The action spectrum carried out additionally conclusively shows that this visible interaction is responsible for the degradation of methyl orange, with the actual efficiency of the reaction following the absorbance of the composite material, as opposed to the absorbance of methyl orange. However the efficiencies calculated in the action spectrum experiments are orders of magnitude lower than the most efficient visible light catalysts, such as Domen's GaN/ZnO solid solution,[20] indicating a commercial catalyst based on this may not be viable. However, as demonstrated in this thesis, particular Chapter 4, co-catalysts have a significant effect on photocatalytic reactions in improving the efficiencies, and the efficiency will almost certainly increase on addition of co-catalysts such as platinum to assist with the reduction reaction, and / or ruthenium oxide to assist with the oxidation reaction. The efficiency of the methyl orange degradation reaction could therefore be significantly improved.

The protocol used in this chapter in identifying the actual interaction between two metals in composite material, determining the energy of the transitions involved, and then demonstrating that this interaction is responsible for organic degradation under visible light is ideal for composite material involving two metal oxides, and further combinations of metal oxides can be explored utilizing this protocol.

## 5.6 References

[1] W. Y. Lin, H. Frei, *J. Phys. Chem. B* **2005**, *109*, 4929-4935.

[2] W. Y. Lin, H. Frei, *JACS* **2005**, *127*, 1610-1611.

[3] H. Han, H. Frei, *Microporous Mesoporous Mater.* **2007**, *103*, 265-272.

[4] H. Han, H. Frei, *J. Phys. Chem. C* **2008**, *112*, 8391-8399.

[5] H. Han, H. Frei, *J. Phys. Chem. C* **2008**, *112*, 16156-16159.

[6] X. Wu, W. W. Weare, H. Frei, *Dalton Trans.* **2009**, 10114-10121.

[7] T. Cuk, W. W. Weare, H. Frei, *J. Phys. Chem. C* **2010**, *114*, 9167-9172.

[8] N. Ulagappan, H. Frei, *J. Phys. Chem. A* **2000**, *104*, 7834-7839.

[9] G. Blasse, *Struct. Bond.* **1991**, *76*, 153-187.

[10] H. Irie, S. Miura, R. Nakamura, K. Hashimoto, *Chem. Lett.* **2008**, *37*, 252-253.

[11] H. Irie, T. Shibanuma, K. Kamiya, S. Miura, T. Yokoyama, K. Hashimoto, *Appl. Catal., B* **2010**, *96*, 142-147.

[12] Y.-C. Xie, Y.-Q. Tang, *Advances in Catalysis* **1990**, *37*, 1-43.

[13] J. R. A. Sietsma, J. D. Meeldijk, J. P. den Breejen, M. Versluijs-Helder, A. J. van Dillen, P. E. de Jongh, K. P. de Jong, *Angew. Chem. Int. Ed.* **2007**, *46*, 4547-4549.

[14] M.-C. Fournier-Salauen, P. Salauen, *Cent. Eur. J. Chem.* **2007**, *5*, 1084-1093.

[15] S. Shen, L. Guo, *Catal. Today* **2007**, *129*, 414-420.

[16] T. Uozumi, K. Okada, A. Kotani, R. Zimmermann, P. Steiner, S. Hüfner, Y. Tezuka, S. Shin, *J. Electron. Spectrosc. Relat. Phenom.* **1997**, *83*, 9-20.

[17] G. T. Brown, J. R. Darwent, *J. Chem. Soc., Faraday Trans. 1 F* **1984**, *80*, 1631-1643.

[18] G. T. Brown, J. R. Darwent, *J. Phys. Chem.* **1984**, *88*, 4955-4959.

[19] R. B. Laughlin, *Phys. Rev. B* **1980**, *22*, 3021-3029.

[20] K. Maeda, K. Teramura, D. L. Lu, T. Takata, N. Saito, Y. Inoue, K. Domen, *Nature* **2006**, *440*, 295-295.

# 6 Conclusion

The aim of the project was to synthesise visible light active material by starting with a UV active material, and modifying to induce visible light absorption, and then confirming the ability of this material to undergo photocatalysis reactions by performing photocatalysis reactions under strict protocols, to prove the visible light response of the photocatalyst.

Niobium oxide was chosen as the UV active material, and two forms of $Nb_2O5$ were formed: mesoporous and nanoparticulate. The nanoparticulate material, synthesised through a precipitation method, was successfully scaled up from the 1 g scale through to 25 g scale, then finally 200 g scale, with characterisation of the particles at each stage of the scale up comparable in terms of the physical properties of the material and the photocatalytic properties. The ease of scale up indicates that this material could be scaled up still further to produce kilogram quantities of a UV active photocatalyst capable of degrading model dyes such as methyl orange, and producing detectable quantities of hydrogen from a methanol and water solution without any further modification. The simplicity of this precipitation route also leads the possibility of using this method for synthesising other transition metal oxides such as tantalum oxide ($Ta_2O_5$),[1] a UV photocatalyst in it's own right, and a starting material for visible light active TaON.[2-3]

This niobium oxide material was modified with platinum group metals, in order to investigate further the effect PGMs have on photocatalysts, and a survey concentrating on platinum, rhodium and palladium was carried out, with material synthesised and characterised using notably dispersion and TEM techniques to characterise the PGM on the surface of the niobium oxide. The hydrogen generation results indicate that even a low weight percentage of PGM added to the niobium oxide (0.01%) show increased performance compared to unpromoted niobium oxide, which is consistent with Ohtani's observation of a single particle of platinum required per particle of semiconductor in his study of platinum on titanium dioxide.[4] Whilst preparing a material with both an

oxidation and reduction co-catalyst was only briefly looked at, protocols and characterisation of the PGM added material synthesised can be followed to study both material with oxidation co-catalyst added, and material with both oxidation and reduction co-catalysts added, in order to synthesise material capable of splitting pure water.

Finally, niobium oxide material was modified by depositing chromium (III) oxide by an impregnation method, to induce charge transfer between the chromium (III) on the surface, and the niobium (V) in the parent niobium oxide. The diffuse reflectance of this composite material was studied, and manipulated to display just the interaction between the chromium (III) and niobium (V), and from this the required energy of the interaction could be calculated, and found to be in the visible region of the spectrum. This interaction was found to be able to degrade the model dye methyl orange when illuminated with visible light, with an action spectrum confirming the chromium (III) / niobium (V) interaction was responsible for the degradation of methyl orange, as opposed to a dye degradation reaction. As noted, the efficiencies for this reaction are low, compared to world leader visible light photocatalysts such as Domen's GaN/ZnO,[5] however the protocol of identifying the interaction between two metals in composite material, determining the energy of the transitions involved, and demonstrating that this interaction is responsible for organic degradation under visible light is ideal for composite material involving two metal oxides, leading to further combinations of metal oxides being explored using comparable protocols.

As shown in the introduction, the field of research in solar energy, and particularly photocatalysis is a dynamic area, with energy and environmental concerns driving the need for utilizing renewable energy such as solar energy. For commercial considerations, efficiency is key, with single figure quantum efficiencies for even the most efficient visible light catalysts limiting commercial development of photocatalysts. Identifying such visible light catalysts can also be problematic, with techniques needed to prove the photocatalyst

in the reactions is utilizing the visible light absorbed. This thesis, in particular when characterising the visible light active chromium – niobium composites, aimed to develop protocols that can definitively identify visible light interactions. By utilizing these techniques, proven visible light material such as the chromium – niobium composites can be demonstrated, with the knowledge gained used to produce new photocatalysts with the aim of improving efficiency, and developing a functional highly efficient visible light photocatalyst capable of addressing the energy and environmental issues addressed.

[1] T. Sreethawong, S. Ngamsinlapasathian, Y. Suzuki, S. Yoshikawa, *J. Mol. Catal. A: Chem.* **2005**, *235*, 1-11.

[2] G. Hitoki, T. Takata, J. N. Kondo, M. Hara, H. Kobayashi, K. Domen, *Chem. Commun.* **2002**, 1698-1699.

[3] K. Maeda, M. Higashi, D. Lu, R. Abe, K. Domen, *J. Am. Chem. Soc.* **2010**, *132*, 5858-5868.

[4] B. Ohtani, K. Iwai, S.-i. Nishimoto, S. Sato, *J. Phys. Chem. B* **1997**, *101*, 3349-3359.

[5] K. Maeda, K. Teramura, D. L. Lu, T. Takata, N. Saito, Y. Inoue, K. Domen, *Nature* **2006**, *440*, 295-295.